Very low field magnetic resonance imaging

Quentin Herreros

QUENTIN HERREROS

VERY LOW FIELD MAGNETIC RESONANCE IMAGING

Cette thèse, préparée au laboratoire SPEC (CEA\DSM\IRAMIS) au sein du groupe NanoMagnétisme et Oxydes, a été encadrée par Claude Fermon.

CONTENTS

INTRODUCTION

Nuclear Magnetic Resonance (**NMR**) is a physical phenomenon enabling the observation of quantum mechanical properties of specific atomic nucleus. It has been extensively developed to study physical, chemical and biological properties of matter through NMR spectroscopy. It occurs when the nuclei of specific atoms are immersed in an external magnetic field B_0 perfectly homogeneous. This magnetic field is expressed either in Tesla or in Oersted (1 Oe = 0.1 mT). Usually, it needs to be of high intensity which means tens of thousand times stronger than the natural earth's magnetic field. Typically a clinical MRI works between 1.5 T and 3 T and the earth's magnetic field has been measured between 0.250 Oe and 0.65 Oe [11]. Another use of the nuclear property has been proposed with Magnetic Resonance Imaging (**MRI**). This widely used medical imaging technique offers relevant clinical diagnosis with a precise spatial representation of specific biological properties. However this method presents some serious drawbacks due to the use of this large magnetic field. To generate such homogeneous field at this strength, superconducting coils are used. These constituents are costly to purchase and to maintain which turns MRI into an expensive imaging protocol. The homogeneity requirements impose a confined design which raises important difficulty for claustrophobic patient (5-7% of the population) [2]. The

comfort of the device is also degraded by gradient generating important acoustic noises. Finally, the use of high field excludes de facto any MRI on patient with pacemakers, earth valves, metallic implants on brain, eyes or ears and infusion catheters because of heating, small displacements and artifacts. Despite those issues, High Field MRI has been extensively developed for clinical uses as the NMR signal amplitude is proportional to the magnetic field strength. Thus the performance of MRI experiments scales as the magnetic field intensity. Moreover, Radio-Frequency (**RF**) tuned coils are used to measure signals at those fields and their detectivity scales also as the magnetic field intensity. All put together, the efficiency of the MRI setup increases roughly as the square of the field. This explains the development of very high field MRI up to 11.7 T [55].

Another approach has been proposed in Very Low Field MRI and Ultra Low Field MRI with the conception of new kind of sensors much more efficient than RF coils for low frequencies. Those configurations can rely on inexpensive resistive coils for the permanent field with an open and light design. Free of any acoustic noises, this technique reduces all safety issues induced by high magnetic fields. Superconducting Quantum Interference Devices (**SQUIDs**) and Atomic Magnetometers are well known sensors presenting a good detectivity competitive with RF coils at low and ultra low field. Through the work of J. Clarke et al. [13], the use of SQUIDs for ultra low field MRI has been proven. Imaging was performed at 132 μT with a pre-polarizing field between 40 and 60 mT. The signal was acquired with a SQUID working at 4 Kelvin and combined with an untuned flux transformer. I. Savukov et al. [50] demonstrated the use of Atomic Magnetometer for in vivo imaging at 2 mT with a pre-polarizing field at 200 mT through a tuned flux transformer. Moreover a recent study led by S. Busch et al. [10] has proven that new relaxation mechanisms at low field could lead to new opportunities for clinical diagnosis. Very and Ultra Low Field MRI appear like promising complementary methods to classical clinical MRI.

In 2004, C. Fermon and M. Pannetier-Lecoeur proposed a new kind of sensor called "Mixed Sensors" [45]. Combining a Giant Magnetoresistance (**GMR**) with a superconducting loop, it delivers a flat response in frequency and may compete with SQUIDs in term of detectivity at very low field. Depending on the superconducting loop material used, its working temperature can be at 4 Kelvin (Low T_C Niobium) or 77 Kelvin (High T_C $YBa_2Cu_3O_{7-d}$). The structure of the sensor makes him resistant against external magnetic perturbation which is essential for any use in MRI conditions.

The goal of this study is to integrate High T_C mixed sensors into two Very Low Field MRI setups. Working with a static field from 1 mT to 10 mT, MRI experiments are performed to evaluate the possibility offered by such system in comparison to existing tools.

High T_C mixed sensors are characterized precisely outside and inside an MRI environment, with pulses and gradients, to test their robustness in working conditions. A comparison between their detectivity and other existing sensors (tuned coils, atomic magnetometer and SQUIDs) is performed, at different frequencies. Finally, the use of different kind of flux transformers is discussed analytically and experimentally. They are broadly used with SQUIDs and Atomic Magnetometer and an optimal configuration adapted to this particular sensor is proposed.

To obtain a clean MRI image, strict conditions must be respected leading to complex coil architectures. Two Very Low Field MRI setups are used : one existing system adapted for small sample (working volume of 5*5*5 cm^3) and one new full-head system adapted for in-vivo brain imaging (working volume of 15*15*15 cm^3). Adjusted to generate a field between 1mT and 10 mT, both are using no pre-polarization field at all. The absence of any pre-polarizing step offers more freedom in sequence optimization and also less perturbations induced by eddy currents. For practical use and comfort of utilization, open design is favored and no dedicated shielded room is used. Permanent field, gradients and RF pulses are precisely characterized and optimized to fit specific requirements at such field. A special attention is paid to homogeneity, amplitude and slew rates as those parameters are critical to build an operative MRI.

A homemade spectrometer and an MRI software are engineered to control both setups with maximum flexibility. Classic spin echo and gradient echo sequences are tested for first imaging tests. Three dimensional images are acquired at different field strength with specific phantoms used to test the robustness of the system and identify problematic artifacts. Indeed the NMR signal is a very precise tool to estimate characteristics of an external magnetic field. Then contrasts are enhanced by using adapted sequence (Echo time, Repetition time,...). The determination of accurate values has required a relaxometry study of tissues and liquids of interests.

Finally, over the past fifty years, high field MRI has seen its acquisition time decreased by a factor thousand. This gigantic reduction of the time needed to image human tissues has been possible with the use of specific sequences called “fast sequences”. Many different methods have been developed but all of them try to reduce the ac-

quisition time to the minimum required to measure a signal. The use of those techniques are discussed for very low field MRI through the use of two well known sequences : Fast Low Angle SHot sequence (FLASH) and Echo Planar Imaging (EPI). Their relevancy at very low field is analyzed through analytical and experimental measurements.

1

MAGNETIC RESONANCE IMAGING : PRINCIPLE

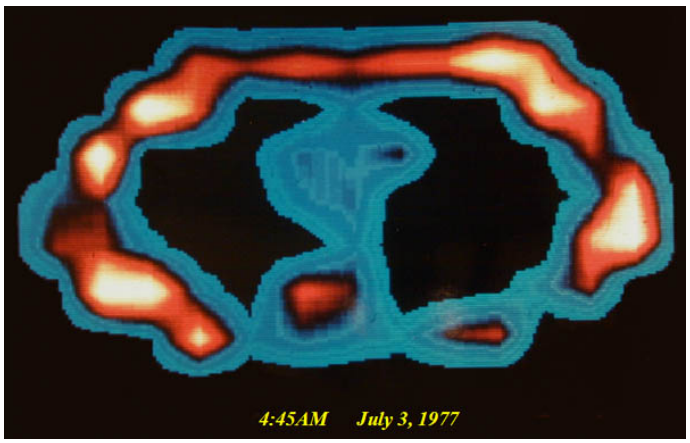

First MRI scan of a live human being chest performed in 1977 [17]

Based on the discovery of Nuclear Magnetic Resonance spectroscopy by Bloch and Purcell in 1945, Magnetic Resonance Imaging has become a major medical imaging technique. In this chapter, I will introduce some general notions about nuclear resonance. Origins and manipulations of the nuclear magnetic moment will be developed. I will also present several specific aspects of very low field NMR. Then an introduction to MRI will present basics of imaging techniques. Through the study of MRI properties, strong and weak points of very low field MRI will be enlightened.

1.1 NUCLEAR MAGNETIC RESONANCE

Nuclear Magnetic Resonance has been extensively developed for medical application through Magnetic Resonance Imaging. Usually, those devices are working with high permanent field. The use of very low permanent field induce new properties. In this section, the polarization and the resonance of the nuclear magnetic moment are introduced. Its frequency and its amplitude for very low field MRI is predicted analytically. The combination of pulses to measure the NMR signal is explained through the presentation of basic sequences. The signal-to-noise ratio problematic in MRI experiments is presented as well as different methods to enhance the nuclear polarization of samples. Finally, the magnetic noise generated by the body is briefly discussed from very low field perspective.

1.1.1 *Polarization and Nuclear Spin*

As points it out the name, Nuclear Magnetic Resonance is a physical phenomenon related to atoms nuclei. Those nuclei are composed of neutrons and protons which both have the intrinsic quantum property of spin. In classical physics, a spin can be seen as the rotation of the charge around its own axe. This spin, or angular momentum, $\vec{I}$ is quantified and induces a magnetic moment $\vec{\mu}$ such as :

$$\vec{\mu} = \hbar\gamma\vec{I}$$

where $\hbar$ is the reduced Planck constant and γ the gyromagnetic ratio of the particle. The overall magnetic moment of a nucleus is then related to a magnetic moment $\vec{M_0} = \sum \vec{\mu}$. This magnetic moment is a critical parameter for NMR measurement. However an even mass nucleus with an even number of neutrons present a zero overall spin ($\sum \vec{I} = 0$) which is not interesting from the NMR point of view. For others nuclei ($\sum \vec{I} \geq \frac{1}{2}$) in absence of external interactions, all spin states are degenerated which lead to $\vec{M_0} = 0$. The application of an external magnetic field B_0 will break degeneracy and spin states will no longer have the same energy.

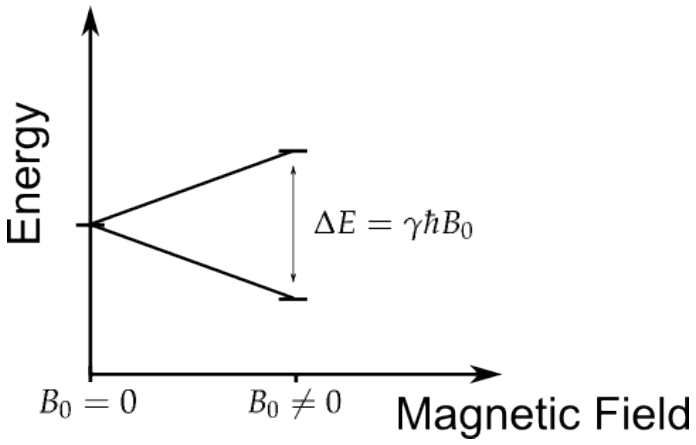

Figure 1.1: Spin states and magnetic field

For most MRI applications, the nucleus ^1H is used as it is present in H_2O, a dominant component in the human body . Figure 1.1 presents this behavior for nucleus with a spin of one-half (like ^1H). This difference in energy results in a small population bias toward the lower energy state and the apparition of an overall magnetic moment $\vec{M}_0$. For ^1H, we have :

$$M_0 = \frac{N\gamma^2\hbar^2 B_0}{4k_b T} \tag{1.1}$$

where N is the spin density, k_b is the Boltzmann constant and T the temperature. This magnetic moment has the same direction as B_0. The use of a magnetic field to generate a magnetization inside a sample is called the polarization.

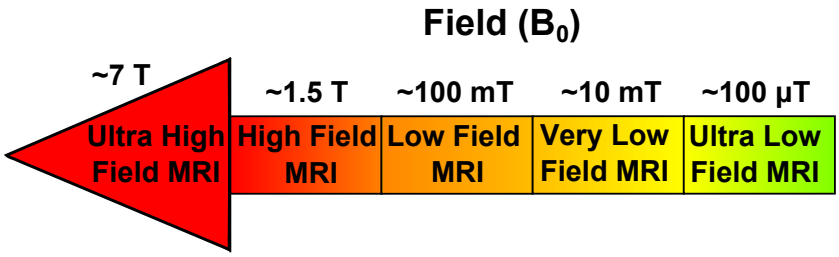

Figure 1.2: Field (B_0) and frequency range of MRI

In this thesis, we are typically working between 1 mT and 10 mT, in the very low field MRI range.

1.1.2 *Excitation and Nuclear Resonance*

The measurement of this magnetic moment is impossible as it is merged into the external magnetic field which is much larger. However, a tip down of the magnetic moment can be achieved with the use

of a radio-frequency pulse. An electromagnetic excitation is applied on the sample at the Larmor Frequency

$$v_0 = \frac{\gamma}{2\pi} B_0$$

This will result in a magnetic resonance absorption and an increase of the high energy state population. At the end of the pulse, the magnetic moment will relax to its original equilibrium state with an angular speed $\omega_0 = 2\pi v_0$.

Nucleus	Gyromagnetic factor $\gamma/2\pi$ (MHz/T)	v_0 at 3T (Mhz)	v_0 at 10 mT (kHz)
^{1}H	42.58	127	426
^{13}C	10.69	32.1	107
^{15}N	4.31	12.9	43.1
^{31}P	17.21	51.6	172

Table 1.1: Commonly observed nuclei ($\sum \vec{I} = 1/2$) and their resonance frequency at 3 T and 10 mT

This relaxation is well described by Bloch equations. For transverse components, we have

$$\frac{dM_{x,y}(t)}{dt} = \gamma(\vec{M}(t) \times \vec{B}(t))_{x,y} - \frac{M_{x,y}(t)}{T_2}$$

where T_2 is the spin-spin relaxation time. It is inversely proportional to the intrinsic inhomogeneity of the sample. For the longitudinal component, we have

$$\frac{dM_z(t)}{dt} = \gamma(\vec{M}(t) \times \vec{B}(t))_z - \frac{M_z(t) - M_0}{T_1}$$

where T_1 is the spin-lattice relaxation time.

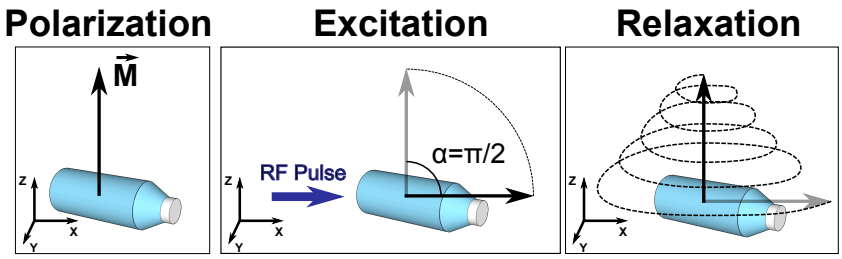

Figure 1.3: Nuclear Magnetic Resonance of a water bottle for a $\frac{\pi}{2}$ pulse. The magnetic moment $\vec{M}$ is described at different stage.

The detection always needs to be orthogonal to the polarization field B_0 to measure the transverse components of the magnetic moment. Thus, in perfect homogeneity conditions, T_2 can be measured

straightly with the Free Induction Decay (**FID**). According to setup requirements and sensors robustness, the detection can be either in the same direction of the pulse or perpendicular to it (for quadrature-phase acquisition). The use of a Fourier Transform allows to convert this temporal signal into its frequency distributed equivalent. It is useful for measuring its amplitude and its bandwidth but especially for imaging purpose as we will see in the next section. It has to be noticed that the Fourier Transform is applied using a specific algorithm called "Fast Fourier Transform". This method reduces dramatically the number of operations needed but requires a cartesian distribution of acquisition points.

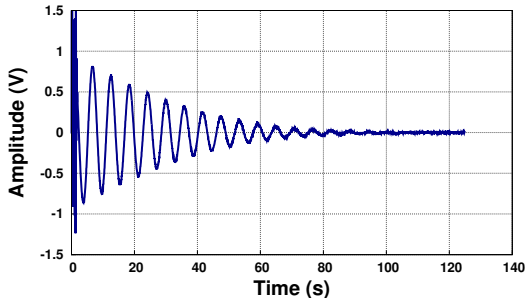

(a)

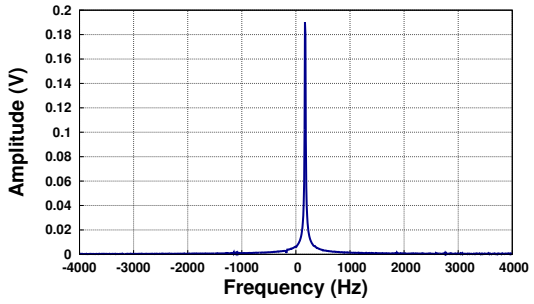

(b)

Figure 1.4: a) Free Induction Decay of a Nuclear Magnetic Resonance signal and b) its Fast Fourier Transform

The NMR signal is oscillating at the Larmor Frequency, which implies that it depends on the applied field B_0 and on the gyromagnetic factor γ of the nucleus (see Table 1.1). An inhomogeneous permanent field $B_0 + \delta B$ will result in a bandwidth widening of the NMR signal ($v_0 + \delta v$) and a faster decoherence between spin phases. Thus it leads to a weakening of signal amplitude and a shorter measured T_2 (called T_2*). Coils that generate B_0 need a specific design to maximize homogeneity to reach the intrinsic spin-spin relaxation of the sample. The higher the field is, the harder it becomes to have a good homogeneity. We will see in this Chapter 2.1 that Very Low Field MRI is not disadvantaged by this particular constrain.

1.1.3 *Basic Sequences*

A sequence can be define as a specific pattern of pulses and gradients (see Chapter 1.2) to measure Nuclear Magnetic Resonance. Complex sequences will be studied in Chapter 6. We will present here just basic sequences, that will be used for a better understanding of future developments.

Free Induction Decay sequence is the use of a single RF pulse to tip the magnetic moment of an angle α. Usually $\alpha = \frac{\pi}{2}$ to maximize the amplitude of detected signals.

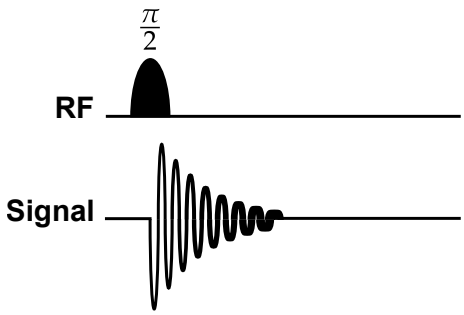

Figure 1.5: Free Induction Decay Sequence

Spin Echo sequence is the use of one excitation pulse α followed by a refocusing pulse π . This sequence is used to get rid of phase decoherence due to external inhomogeneity. Let's take two spins a and b at $t = 0$ in phase ($\Delta\varphi = \varphi_{a,0} - \varphi_{b,0} = 0$) . Inhomogeneous field $B_p(x,t)$ and intrinsic inhomogeneity of the sample $B_i(x,t)$ introduce a decoherence over time such as

$$\begin{cases} \varphi_{a,t} &= \varphi_{a,0} + \varphi_{B_p(a,t)} + \varphi_{B_i(a,t)} \\ \varphi_{b,t} &= \varphi_{b,0} + \varphi_{B_p(b,t)} + \varphi_{B_i(b,t)} \end{cases}$$

and then

$$\Delta\varphi = \varphi_{B_p(a,t)} + \varphi_{B_i(a,t)} - \varphi_{B_p(b,t)} - \varphi_{B_i(b,t)}$$

A π pulse inverse the phase and we obtain $\varphi_{x,t} = -\varphi_{x,t}$. After a time t', we will obtain

$$\begin{cases} \varphi_{a,t+t'} &= -\varphi_{a,0} - \varphi_{B_p(a,t)} - \varphi_{B_i(a,t)} + \varphi_{B_p(a,t')} + \varphi_{B_i(a,t')} \\ \varphi_{b,t+t'} &= -\varphi_{b,0} - \varphi_{B_p(b,t)} - \varphi_{B_i(b,t)} + \varphi_{B_p(b,t')} + \varphi_{B_i(b,t')} \end{cases}$$

and then

$$\begin{aligned} \Delta\varphi = \quad & -\varphi_{B_p(a,t)} + \varphi_{B_p(a,t')} - \varphi_{B_i(a,t)} + \varphi_{B_i(a,t')} + \dots \\ & \dots \varphi_{B_p(b,t)} - \varphi_{B_p(b,t')} + \varphi_{B_i(b,t)} - \varphi_{B_i(b,t')} \end{aligned}$$

The intrinsic inhomogeneity is random and then it is not symmetrical with the refocusing pulse. However an external perturbation $B_p(x,t)$

can be symmetrical (if it is constant for exemple). That way, the dephasing becomes

$$\Delta\varphi = -\varphi_{B_i(a,t)} + \varphi_{B_i(a,t')} + \varphi_{B_i(b,t)} - \varphi_{B_i(b,t')}$$

Only the decoherence of the intrinsic inhomogeneity remains. Thus Spin Echo can be used to access the "real" T_2 in inhomogeneous environment. It is also relevant for three dimensional imaging and the use of frequency coding (see Chapter 1.2).

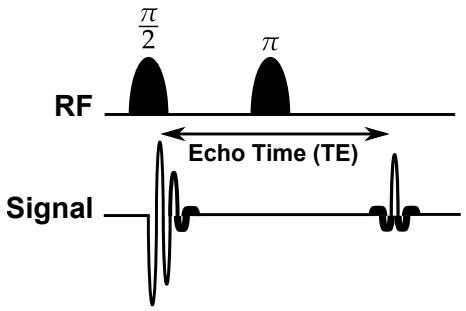

Figure 1.6: Spin Echo Sequence

Regardless the method, the separation time between two sequences is an important parameter (see Chapter 1.2) which is called the repetition time (TR). In a Spin Echo, the separation time between the excitation pulse and the refocusing pulse is called the Echo Time (TE).

1.1.4 *Magnitude of low field NMR signal*

It is of prime importance to have an idea of the signal strength of a sample. It defines the minimum required detectivity of a sensor to measure the signal without any averaging. We define a sample as a cube of water of 1 cm^3. We consider this sample just after a theoretical pulse of $\frac{\pi}{2}$. Thus this cube can be decomposed in magnetic dipoles of 1 mm^3 with a magnetic moment $\vec{m}$.

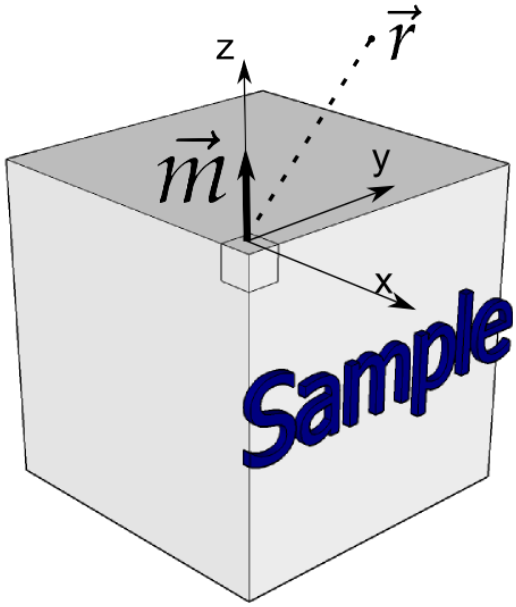

Figure 1.7: Description of the sample

In this configuration, the dipole equation is

$$\vec{B} = \frac{\mu_0}{4\pi r^3}(3\frac{\vec{m}.\vec{r}}{r^2}.\vec{r} - \vec{m})$$

where μ_0 is the vacuum permeability and $\vec{B}$ is the magnetic field generated by the moment $\vec{m}$ at the position $\vec{r}(x, y, z)$. Magnetic sensors are just measuring one component of the field which correspond to B_z such as

$$B_z = \frac{m\mu_0}{4\pi r^3}(3\frac{z^2}{r^2} - 1)$$

The magnetic moment m of 1 elementary dipole can be estimated using 3.1. The number of proton H inside 1 mm^3 is :

$$N = 2N_A\frac{M_{1mm^3}}{M_{H_2O}} = 6.7 * 10^{19}$$

Then, at 300K, under a permanent field of 10 mT, we have

$$m = 3.3 * 10^{-14}\ A.m^2$$

The contribution of all magnetic dipole are added up to obtain the generated magnetic field profile (Figure 1.8).

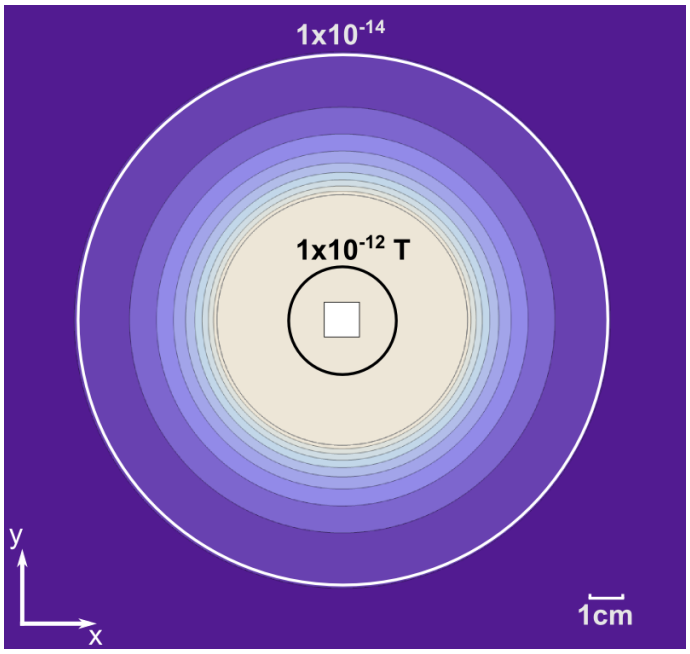

Figure 1.8: Field magnitude generated by a water sample (in white)

At a distance of 1 cm, the field amplitude along z is around 1 pT. In a low noise environment, it gives an order of magnitude of the minimum required detectivity to see the signal with one acquisition at 10 mT. It has to be compared with the same sample in a classical high field MRI at 3 Tesla. At 1 cm, the field magnitude along z is 300 times stronger (300 pT). Using a high magnetic field provide a better signal and then a better quality image. New MRI devices have been built to perform clinical study at 7T [37].Very Low Field MRI presents a clear disadvantage in terms of signal.

1.1.5 *Polarization Enhancement*

This limitation in polarization is intimately linked to very low field study. However, some solutions exist to overcome this restriction.

Magnetization pre-polarization is a field cycling method. A high magnetic field is applied during a time T_1 on the sample to get a large polarization. Then the spin precession is measured in the low permanent field. In this way the signal is strongly enhanced. The pre-polarization field doesn't need to be homogeneous as it is applied before acquisition time. This allow the use of simple and cheap coil designs. However it presents some drawbacks. First, the pre-polarization phase is time consuming and needs to be repeated after each pulse which is a strong constrains on the used sequences. Secondly, this method still excludes all metallic implants. Finally, low field MRI usually needs shielded environment which are subject to strong Eddy currents induced by strong field variations. Those undesired currents perturb the overall homogeneity. This method has

been used with SQUIDs for in vivo Ultra Low Field MRI [41] and for microfluidic applications [56].

Hyperpolarization of noble gases is frequently used to image porous media such as lungs [42]. Atoms like ^{129}Xe and ^{3}He (nuclear spin of 1/2) can see their magnetic moment enhanced by interaction with a pumped atomic alkali vapor like rubidium (Rb). Electrons of an alkali metal vapor are polarized with a laser beam and then this polarized electronic state is transferred to the noble gas through a spin-exchange interaction.

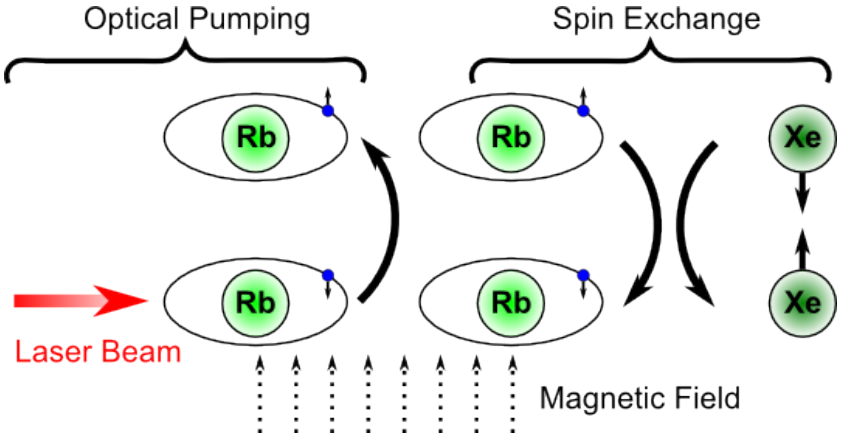

Figure 1.9: Hyperpolarization steps for ^{129}Xe

The nuclear polarization of the noble gas can be up to 10%. In comparison, the ^{1}H polarization at 10 mT is around 0.02 ppm.

Dynamic Nuclear Polarization, based on Overhauser effect [44], enhances the nuclear magnetization by transferring spin polarization from electrons to nuclei. Free radicals (unpaired electron spins) are usually added to the studied sample. A Radio-Frequency irradiation of the two-spin system at the frequency of the electron spin resonance (ESR) is applied.When the saturation is reached, a transfer of polarization from electron to nuclear spin starts. The non-equilibrium polarization created is much larger than the corresponding thermal equilibrium polarization. One promising use of DNP for in vivo imaging is called DNP hyperpolarization or DNP dissolution [6]. The idea is to perform DNP on a solid state sample under 3 T at a temperature around 1K. The polarization is increased by a factor 10000 and is preserved when the solid is dissolved in a liquid phase. This hyperpolarized liquid is then separated from free radicals and injected in vivo. However this method is limited to nuclear spins with a long longitudinal relaxation time T_1 (like ^{13}C and ^{15}N).

Those methods are not used here in this thesis but could be implemented to the existing setup for future research.

1.1.6 *Signal-to-noise ratio*

Those efforts to increase the polarization fit into the overall project of increasing signal-to-noise ratio (**SNR**). Magnetic Resonance Imaging depends strongly on this parameter as it is directly involved in the quality of the image. It can be defined as the power ratio between the meaningful information P_{signal} and the background noise P_{noise}.

$$SNR = \frac{P_{signal}}{P_{noise}}$$

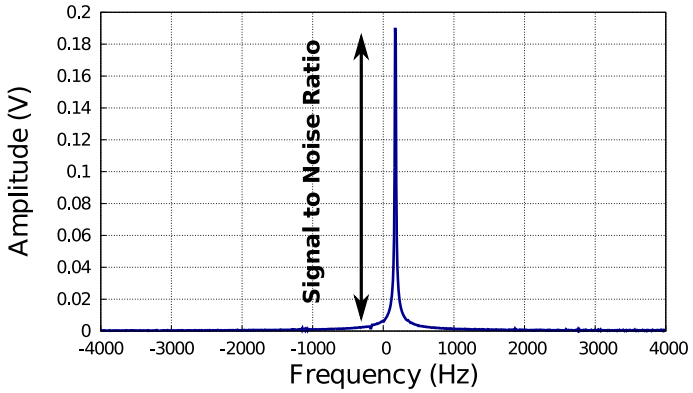

Figure 1.10: Signal-to-noise ratio for a nuclear magnetic resonance signal

Some other solutions than doping polarization are briefly presented here to maximize it :

- One option concerns the detection chain. An efficient sensor presents a low intrinsic noise and a high sensitivity. For high field MRI, sensors are fully optimized and the limiting noise is coming from the sample itself. Concerning Very Low Field MRI, sensors are still an important limitation for signal-to-noise ratio. As we will see more precisely in Chapter 3 and Chapter 4, it is then of prime importance to look for efficient detection method.

- The nuclear magnetic resonance signal can also be averaged. A train of pulses will result in the creation of identical resonances with same phases. However, most of external noises are random in phase. For N acquisitions, a decrease of the noise amplitude of $\sqrt{N}$ will be observed. In the mean time, the nuclear magnetic resonance signal will remain the same as identical pulses involve identical relaxations. This method is time consuming which can be an important issue for clinical applications. As we will see more precisely in Chapter 6, complex sequences have been developed to optimize this aspect.

1.1.7 *Sample Noise*

As we have briefly said before, a conducting sample, like a body, is generating some noise. The capacitive coupled noise component is neglected as it is insignificant at low frequency and can be prevented with specific coil engineering at high frequency. The magnetically coupled noise component can be modeled as a resistance added to the detection.

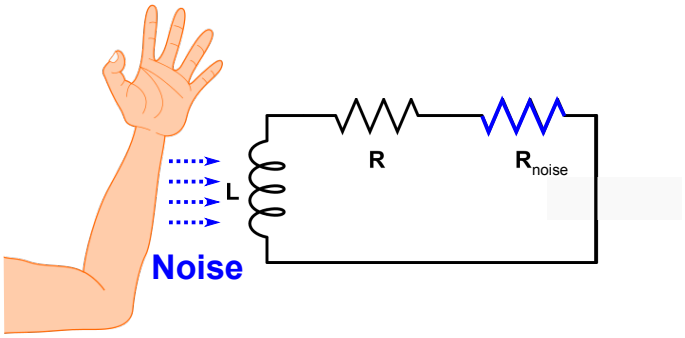

Figure 1.11: Body noise influence on an untuned coil circuit

This series resistance can be described by [43]

$$R_{body} = \sigma \mu_0^2 \omega^2 V_{loss}$$

where σ is the sample conductivity, μ_0 the vacuum permeability, ω the working frequency and V_{loss} a volume parameter containing all geometrical factors. In [43], biological tissues conductivity $\sigma(f)$ has been interpolated between 1 kHz and 10 Mhz using the measured values of [22] such as

$$\sigma = 0.03 f^{0.17}$$

This dependence in frequency explains the need of a new evaluation of body impact at very low field. To approximate the noise generated by an arm and a full head, we model them respectively as an homogeneous cylinder with a radius of 5 cm and an height of 5 cm and a perfect sphere with a radius of 10 cm. We consider an untuned coil (Ø = 6 cm) at 2.5 cm from the sample. The voltage noise emitted inside the coil will be

$$S_V^{1/2} = \sqrt{4 k_b T R_{body}}$$

where T is the body temperature. This can be also written as a magnetic field noise such as

$$S_B^{1/2} = \frac{\sqrt{4 k_b T R_{body}}}{\omega A_p}$$

where A_p is the measuring coil area. This lead to an approximation of the generated noise (Figure 1.12).

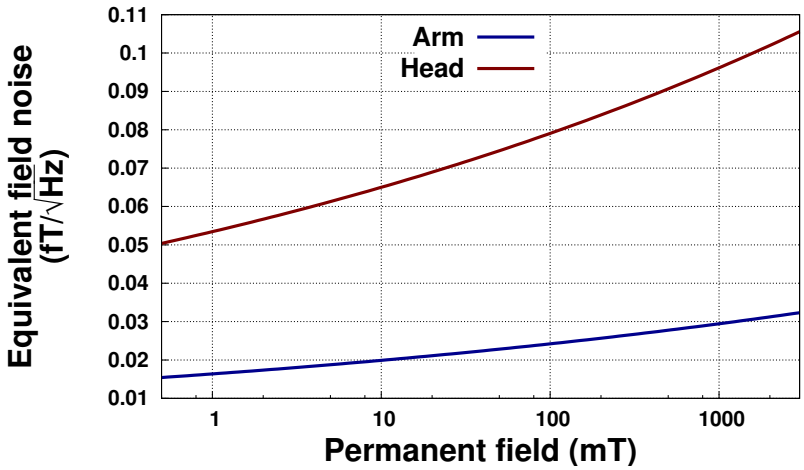

Figure 1.12: Magnetic field noise generated by an arm in a copper coil with different applied fields

We can see that around 10 mT, we expect a noise around 0.02 $fT/\sqrt{Hz}$ for an arm or for a full head. The equivalent field noise dependency in volume, proportional to $\sqrt{V_{loss}}$, appears clearly here. This defines the lower theoretical limit we can achieve in term of noise with such MRI system.

1.2 SPATIAL ENCODING AND IMAGING FEATURES AT VERY LOW FIELD

To obtain an image from the NMR signal, the use of gradients is required. In this section, three dimensional imaging is introduced through the presentation of frequency and phase encoding gradients as well as slice selection gradient. Typical sequences are presented and parameters like resolution, field of view and signal-to-noise ratio are precisely defined. Finally, contrast-to-noise ratio specificity at very low field MRI is discussed through a spin relaxation mechanisms study.

1.2.1 *Frequency encoding and K-space definition*

In the previous section simple methods to acquire a single NMR signal have been shown. However this signal only gives us two informations about the sample :

- The number of protons which is linked to its amplitude.
- Its mean relaxation properties linked to T_1 and T_2.

We get no spatial information straightly from the NMR signal. The use of magnetic field gradients will allow a decomposition of the signal depending on its spatial location. When we apply one linear gradient $\frac{\partial B_x}{\partial x} = G_x$ along $\vec{x}$ during the acquisition, the phase shift at a position x after a time t is

$$\Delta\varphi(t) = \gamma B_0 t + \gamma G_x x t$$

Since the signal emitted at a pixel x is proportional to the number of spins and has the phase given above, the signal detected by the coil can be written as

$$S(t) = \iint_{Sample} \rho(x) e^{i(\omega_0 t + \gamma G_x x t)} dx$$

As we will see in Chapter 2.3, the modulation factor $e^{i\omega_0 t}$ is thrown away by the detection hardware and we define $k_x = \gamma G_x t$ such as

$$S(k_x) = \iint_{Sample} \rho(x) e^{ik_x x} dx$$

The result obtained after an Inverse Fast Fourier Transform is a projection of our sample over x.

$$\rho(x) = FFT^{-1}(S(k_x))$$

Here k_x is a coordinate in the spatial frequency space also called "K-space" in opposition to the "real" spatial space (see Figure 1.13). It

determines the spatial periodicity, also called resolution, and the field-of-view (**FOV**) of the acquisition. In MRI, it is more convenient to see the sampling as a function of k.

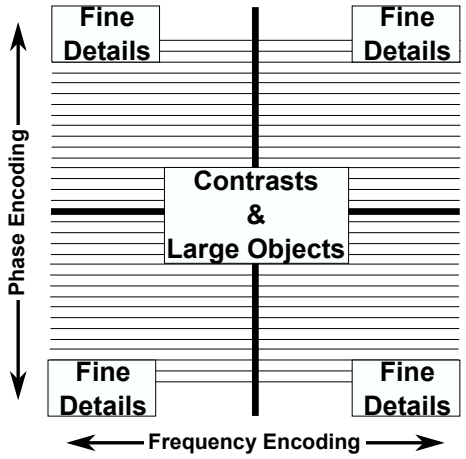

Figure 1.13: K-space representation

The Fast Fourier Transform supposes a cartesian distribution of the K-space. A non-linear gradient will result in a non-cartesian distribution and then a wrong image reconstruction with artifacts and distortions.

One dimensional imaging can be performed using frequency encoding method. It can be used through a Spin Echo sequence or a Gradient Echo sequence.

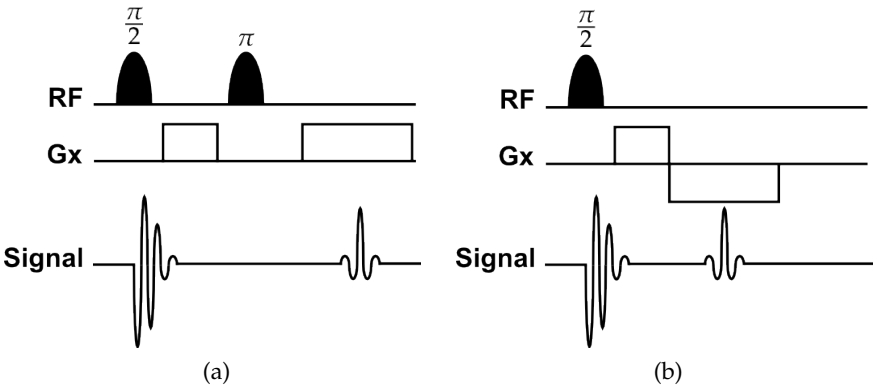

Figure 1.14: (a) Spin Echo and (b) Gradient Echo sequences with frequency encoding gradients along x

Gradient Echo requires an homogeneous environment as it does not use any refocusing pulse. A reverse gradient is used to refocus spins. This method is usually faster than Spin Echo as one excitation pulse is used.

1.2.2 *Phase Encoding*

The "phase encoding" dephases spins along one direction using a gradient G_y during a time τ before the acquisition. The phase shifts at a position (x, y) is

$$\Delta\varphi(t) = \gamma B_0 t + \gamma G_x x t + \gamma G_y y \tau$$

Here $k_y = \gamma G_y \tau$ then

$$S(t) = \iint_{Sample} \rho(x,y) e^{ik_x x + ik_y y} dx dy$$

As for k_x , we need to scan the K-space along y. Given that the parameter τ is defined, this can be done by changing G_y for each k_y. Thus each pixel along the second direction will require one acquisition.

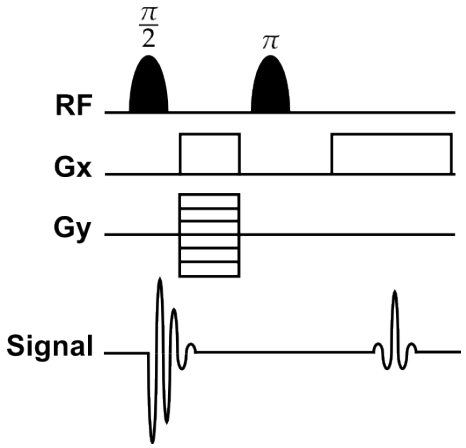

Figure 1.15: Two dimensional imaging with a spin echo sequence

A phase encoding can be performed on one or two directions simultaneously. Then we can access to three dimensional imaging with a double phase encoding.

1.2.3 *Slice Selection*

Three dimensional imaging can also be performed slice by slice. The main idea is to excite a selective part of the sample and then to perform a 2D imaging of this selected part. Then a three dimensional image can be reconstructed. A slice selection requires a pulse designed to excite a narrow frequency bandwidth Δf. Usually a pulse with a cardinal sinus shape is used during a time $T = 1/\Delta f$. This specific shape reduces the sidebands of the selection. Then if a gradient is applied during this selective pulse, just a part of the entire sample will be excited.

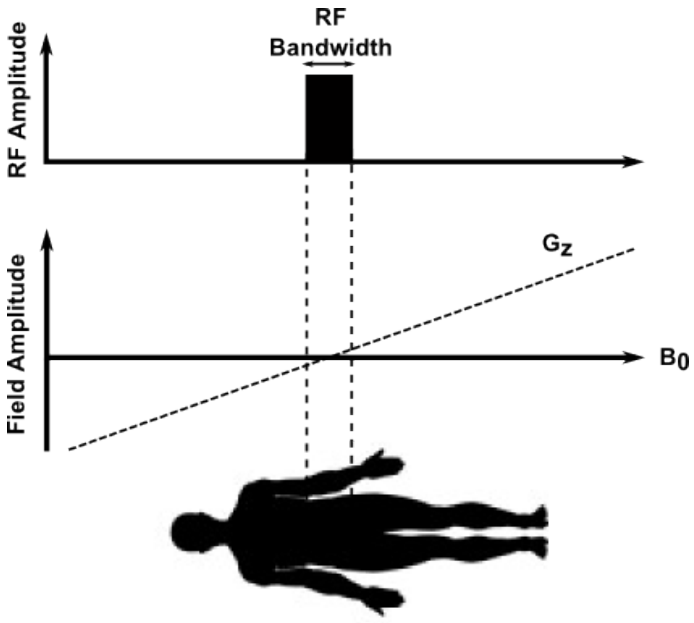

Figure 1.16: Slice selection scheme

After the selection, a classic two dimensional imaging sequence is applied.

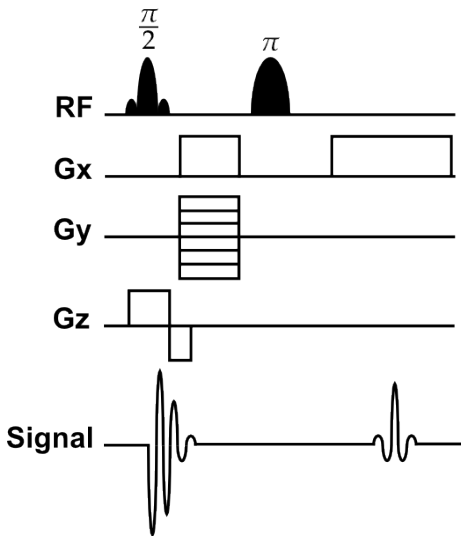

Figure 1.17: Three dimensional imaging with a slice selection and spin echo sequence

Working slice by slice has its advantage, even if the used pulses are longer. Further explanation will be given in Chapter 5.

1.2.4 *Resolution*

The resolution of an MRI image is defined by voxels size. It is linked to the K-space by

$$(k_x, k_y, k_z) = 1/\delta(x, y, z)$$

where (k_x, k_y, k_z) stands for a k-space line along one chosen direction and $\delta(x, y, z)$ for the resolution along the corresponding spatial direction. For the frequency coding direction, we have

$$k_x = \frac{\gamma G_x T_x}{2\pi}$$

where T_x is the total time of the readout gradient G_x application. Then, for a given T_x , we can achieve a resolution δx with a gradient respecting

$$G_x = \frac{2\pi}{\delta x \gamma T_x}$$

According to this equation, we could always compensate a decrease of T_x, which corresponds to an artificial broadening of the linewidth, by an increase of G_x . However, this will lead to a larger frequency spread which leads to a decrease in signal-to-noise ratio. Moreover T_x has a maximum value which is defined by T_2 or T_2^* according to external inhomogeneities. For a given δx , it is necessary to use a minimum gradient strength (see Chapter 2.2).

For the phase encoding direction, we have

$$k_y = \frac{\gamma N_y \delta G_y \tau}{2\pi}$$

where N_y is the number of points along y direction and δG_y one step of the phase encoding gradient. Then

$$\delta G_y = \frac{2\pi}{\delta y \gamma N_y \tau}$$

Just like frequency coding, τ has a maximum value which is defined by T_2 or T_2^*.

Finally, for the slice selection direction, the resolution is defined by the pulse length and the gradient strength. A pulse with a cardinal sinus shape excites a bandwidth

$$\Delta f = \frac{1}{t_0}$$

where t_0 corresponds to one-half the width of the first lobe. For a desired resolution δz, we need a gradient such as

$$G_z = \frac{2\pi}{t_0 \gamma \delta z}$$

Gradients are mainly defined by the desired resolution.

1.2.5 *Field Of View*

The field of view is defined by the size of the spacial encoding area of the MRI image. We have

$$(x, y, z) = 1/\delta(k_x, k_y, k_z)$$

where (x, y, z) stands for the field of view along one spatial direction and $\delta(k_x, k_y, k_z)$ for the resolution along the corresponding k-space direction. For a frequency sampling $f_s = \frac{1}{\delta t}$ along the frequency coding direction, we have

$$x = \frac{2\pi}{\gamma G_x \delta t}$$

The frequency sampling needs to be chosen wisely to avoid any signal outside this "window". A too small field-of-view will result in wrap-around artifacts also called aliasing. Signals out of the bandwidth will be mismapped to the opposite side of the image leading to indecipherable images. For the phase encoding gradient, we have

$$y = \frac{2\pi}{\gamma \delta G_y \tau}$$

Finally, the slice selection direction doesn't have the same field of view problematic as the image is reconstructed slice by slice and cannot be subject to any aliasing.

1.2.6 *Signal to Noise Ratio*

The strength of the frequency coding gradient, also called readout gradient, has an influence on the Signal to Noise Ratio. A larger gradient involves a larger receiver bandwidth BW and a spread of the signal which leads to an enlargement of noise contribution. Finally, the signal-to-noise ratio can be expressed as

$$SNR = KB_0(\frac{x}{N_x}\frac{y}{N_y}\delta z)\sqrt{\frac{N_x N_y N_{average}}{BW}}$$

where the constant K includes detection factors (see Chapter 3 and 4), sequence parameters (TR, TE, ...) and tissues factors (body noise, spin density, T_1, T_2, ...), N_x and N_y are the number of frequency and phase encoding steps, $N_{average}$ is the number of signal averages and B_0 the applied permanent field.

We want to compare the SNR of two identical phantoms A and B respectively sampled at $B_{0,A} = 1.5$ T and $B_{0,B} = 10^{-2}$ T with the same relative field homogeneity and the same sequence. If we call δB_A and δB_B the absolute field inhomogeneity between A and B, we have

$$\frac{\delta B_A}{\delta B_B} = \frac{T^*_{2,B}}{T^*_{2,A}} = \frac{B_A}{B_B}$$

where T_2^* is the apparent relaxation time of the transverse component. We suppose here that the main external inhomogeneity is coming from our permanent field. This imposes conditions on gradients strength such as

$$\frac{BW_A}{BW_B} = \frac{B_A}{B_B}$$

Finally,

$$\frac{SNR_A}{SNR_B} = \frac{K_A}{K_B}\sqrt{\frac{B_A}{B_B}} \approx 12.2\frac{K_A}{K_B}$$

In a first approximation, Very Low Field MRI presents a reasonable disadvantage in signal-to-noise ratio in comparison to High Field MRI. With equivalent sensors in both configurations, we would lose a factor $\sqrt[3]{12.2} \approx 2.3$ in resolution in each direction. This would correspond to a typical resolution of 2x2x2 mm^2. However the ratio $\frac{K_A}{K_B}$ corresponding to sensors efficiency between 10 mT and 1.5 T should be equal to 1. Chapter 3 and 4 will describe new detection methods that are trying to reach this achievement. However, the signal-to-noise is not the only interesting MRI parameter.

1.2.7 *Contrast-to-noise ratio*

The signal-to-noise ratio and the resolution are two interconnected parameters that clearly define the quality of MRI images. However, contrast is also determinant for clinical study of images as it reveals environmental interactions and intrinsic properties of tissues. It can be defined as the relative difference of signal intensities in two adjacent regions A and B. It can be measured by the contrast-to-noise Ratio (**CNR**).

$$CNR = SNR_A - SNR_B$$

where SNR_A and SNR_B stand for the signal-to-noise ratio of both regions. Three main parameters can induce strong contrast differences.

The spin-lattice relaxation time T_1 which depends on the lattice vibration of the sample structure. The longitudinal component M_z of the magnetic moment is relaxing such as

$$M_z(t) = M_{z,0}(1 - e^{-t/T_1})$$

A typical sequence to enhance contrasts between a short longitudinal relaxation time T_{1s} and a long longitudinal relaxation time T_{1l} is to choose a relevant repetition time TR with $T_{1s} \leq TR \leq T_{1l}$ and a short echo time TE to get rid of any T_2 weighting. That way, for identical protons density, the sample with a short T_1 will reveal a higher signal. It is called a T_1 weighted image.

The spin-spin relaxation time T_2 which depends on the random fluctuations of the local magnetic field. The transverse component M_{xy} of the magnetic moment is relaxing such as

$$M_{xy}(t) = M_{xy,0}(e^{-t/T_2})$$

A typical sequence to enhance contrasts between a short transverse relaxation time T_{2s} and a long transverse relaxation timeT_{2l} is to choose a relevant echo time with $T_{2s} \leq TE \leq T_{2l}$ and a long repetition time TR to get rid of any T_1 weighting. That way, for identical protons density, the sample with a long T_2 will reveal a higher signal. It is called a T_2 weighted image.

The proton density ρ which depends on tissues properties. The main difficulty of such weighted image is to suppress all other weighting. A long repetition time TR combined with a short echo time TE provide a pure proton density map. It has to be noticed that clinically, this type of acquisition doesn't bring much information.

Some contrast agents are sometimes used. After oral or intravenous administration, they enhance the contrast-to-noise ratio of specific tissue lesions. Very low field MRI present strong particularities about relaxation time. The Bloembergen-Purcell-Pound (BPP) theory [8] proposes a 2-spin system model with a rotational movement characterized by the correlation time τ_C of the molecular tumbling motion. According to this model, the relaxation times T_1 and T_2 of such molecule depends on the Larmor frequency in the following way :

$$\frac{1}{T_1} = K[\frac{\tau_C}{1+\omega_0^2\tau_C^2} + \frac{4\tau_C}{1+4\omega_0^2\tau_C^2}]$$

$$\frac{1}{T_2} = \frac{K}{2}[3\tau_C + \frac{5\tau_C}{1+\omega_0^2\tau_C^2} + \frac{2\tau_C}{1+4\omega_0^2\tau_C^2}]$$

where ω_0 is the Larmor frequency and K a constant depending on the molecule.

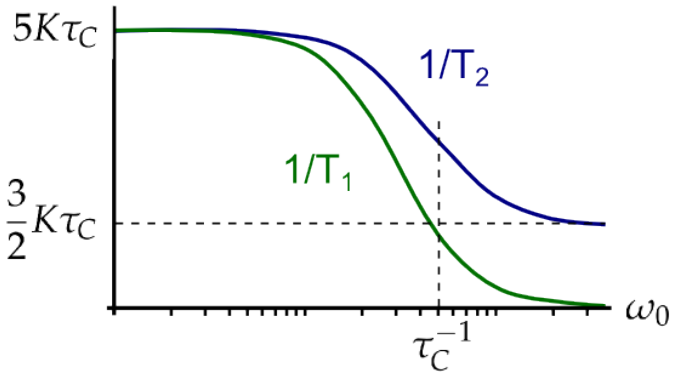

Figure 1.18: Dependency of T_1 and T_2 on the Larmor pulsation ω_0 according to the BPP theory

The correlation time τ_C for H_2O molecules is typically around 10^{-12} seconds in liquid phase without contamination. In vivo, water is

bounded to macromolecules and the correlation time ranges from 10^{-9} to 10^{-6} seconds [27]. When $\omega_0 \ll \tau_c$, it appears that T_2 and T_1 tend to the same value. It has been verified experimentally for brain tissues [58].

	Grey matter at 1.5 T	Grey matter at 46 μT	White matter 1.5 T	White matter 46 μT
T_1	1130 ms	103 $\pm$ 5 ms	889 ms	75 $\pm$ 2 ms
T_2	102 ms	106 $\pm$ 11 ms	86 ms	79 $\pm$ 11 ms

Table 1.2: Relaxometry of brain tissues at high field and at ultra low field [58]

We can also notice that both T_1 and T_2 become more sensitive to the correlation time τ_C. This parameter related to macromolecules motion brings a new specific information contained inside T_1 and T_2 . In [33], the T_1 of two samples with different concentration of agarose (and then a different τ_C) are monitored at different frequencies. It appears that below 10 mT, their longitudinal relaxation time is diverging. The result is the apparition of new contrasts at those frequencies.

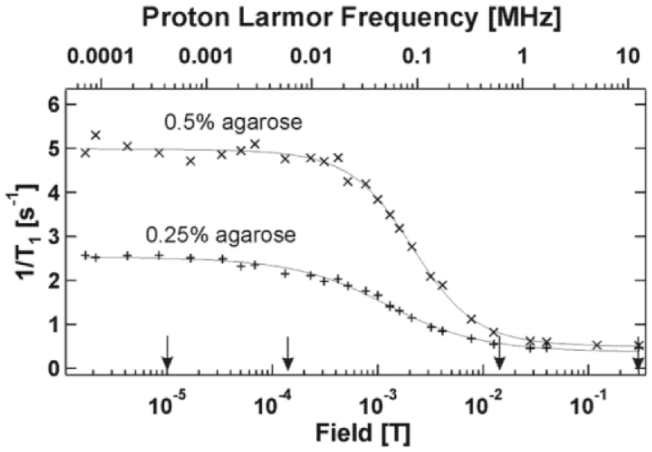

Figure 1.19: Relaxation rate dispersion of 0.25% and 0.5% agarose gel in water measured between 72 Hz and 12.8 MHz.[33]

A clinical application of this relaxation change has been studied concerning the prostate cancer. S. Bush and al. [10] have recently shown in ex-vivo prostate that cancerous tissues were presenting a different T_1 than normal tissue at low frequency.

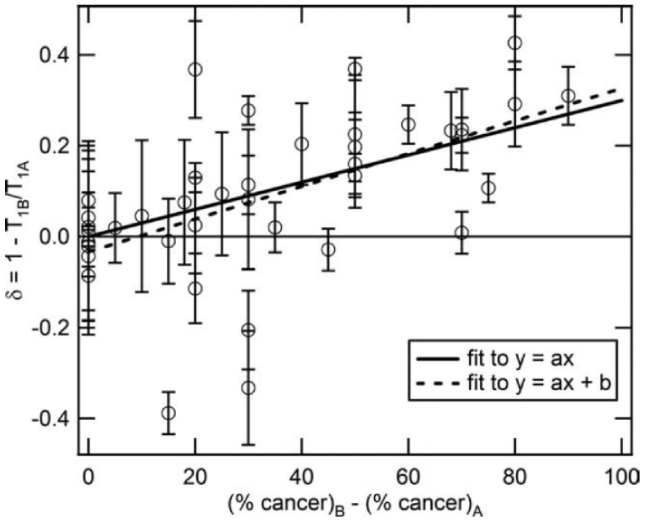

Figure 1.20: Contrast δ versus the percentage cancer between two ex-vivo prostate A and B. The solid line fit respect $y = 0.003x$ and $R^2 = 0.3$. The dashed line fit respect $y = 0.0036x - 0.0334$ and $R^2 = 0.31$.[10]

Intrinsically, very low field MRI presents a lower signal-to-noise ratio than high field MRI. However contrasts at those frequencies are more sensitive to some biological environment properties and could then lead to new diagnosis possibility.

CONCLUSION

Very low field MRI relies on the same principle than high field MRI but important differences have been enlightened. The polarization of the nuclear magnetic moment is much smaller but its impact on signal-to-noise ratio is compensated by a reduced acquisition bandwidth due to a better absolute homogeneity. Thus a factor 2.3 in resolution is lost for every direction in comparison to 1.5 T devices. Moreover, the frequency of the nuclear magnetic relaxation is much lower which implies difficulties for the detection. It will be precisely developed in Chapter 3 and 4. Regardless of the sensor, the fundamental noise limit is related to the magnetic noise generated by the body. At very low field, this noise has a lower amplitude as the conductivity of biological tissues is decreasing with frequency. With ideal sensors, we would then lose only a factor 1.8 in resolution in comparison to 1.5T devices. Finally, this loss could be balanced by a better contrast-to-noise ratio due to molecular motion influence on T_1 below 10 mT.

2

EXPERIMENTAL SETUP

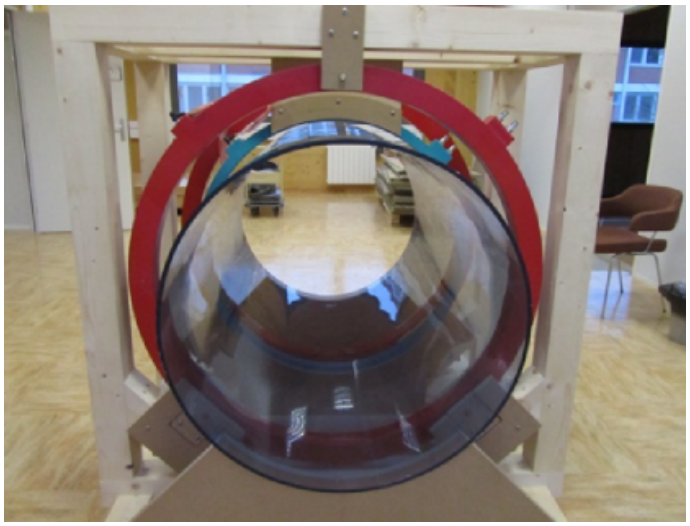

Full-head setup for MRI at very low field

Magnetic Resonance Imaging uses a complex combination of fields. Each one of them must be precisely defined in terms of amplitude, frequency, homogeneity and timing. Therefore a complete study of needed components is necessary to achieve a correct acquisition. From gradients to radio-frequency pulses including spectrometer and permanent field, all of them will be designed and then tested to fulfill very low field requirements. The methodology and results will be presented through three different sections.

2.1 PERMANENT FIELD AND HOMOGENEITY

In this section, permanent field is discussed. Different methods are explored to generate a field with an amplitude and homogeneity adapted to very low field MRI. Two setups are described :

- One existing setup adapted for small objects imaging [18]
- One new setup adapted for full-head imaging

The design of both configurations is described and a precise characterization of all relevant parameters (amplitude, homogeneity, noise) is performed.

2.1.1 *Different kind of magnets*

In MRI, several options exist to generate a magnetic field.

Superconducting electromagnets are the most common devices for clinical MRI with a field above 1.5 T. Superconducting material like niobium-titanium or niobium-tin are used to wind the coil. Those materials lose their resistance below their critical temperature (around 10 K). When the alloy is cooled by liquid helium to 4K, it thus becomes superconductor. This important physical effect will be explained more precisely in Chapter 3. Without resistance, an important current can flow through the coil and generate a high field with a good stability. However those magnets are extremely costly to produce and the cryogenic helium is expensive and difficult to handle for such sized coils. Their cylindrical geometry also imposes a confined space for the patient which can induced claustrophobia problem.

Permanent magnet are conventional magnets made of ferromagnetic materials containing steel alloys with rare earth elements. Compared to superconducting magnets, they generate a weak field (usually $\leq$ 0.4 T) which is limited in precision and stability. Moreover, it is impossible to adjust accurately the field or to "turn off" those magnets. Finally, reaching such field strength requires large and bulky elements that can weight over 100 tonnes. Even if they are inexpensive to maintain, those magnets are not easy to use for clinical MRI.

(a) (b)

Figure 2.1: a) 3 T MRI system with superconducting electromagnets (SIEMENS) and b) 0.35 T MRI system with permanent magnets (NEUSOFT)

Resistive electromagnets are very similar to superconducting magnets in term of design. The coil is a solenoid wound from copper. Field strength and stability of such electromagnet are limited and require an important electrical energy during operations. However it is a relevant method for very low field MRI applications. The initial cost is low and it is possible to build open and light systems to generate a field as high as 10 mT with a good homogeneity. This is the solution that has been chosen for our very low field MRI system.

2.1.2 *Homogeneity required*

The homogeneity of the permanent field B_0 is of primary importance for MRI applications. For a magnetic field variation of δB on a sample, we have

$$\frac{1}{T_2^*} = \frac{1}{T_2} + \frac{1}{2\pi}\gamma\delta B$$

Then T_2^* can be defined as the relaxation time due to spin-spin relaxation and all external magnetic field inhomogeneities. Spins inside the sample will present different precession frequencies and will move out of phase much faster. Then

$$T_2^* \leq T_2$$

This relaxation time defines the linewidth at half-height δv of our NMR signal such as

$$\delta v = \frac{1}{T_2^*}$$

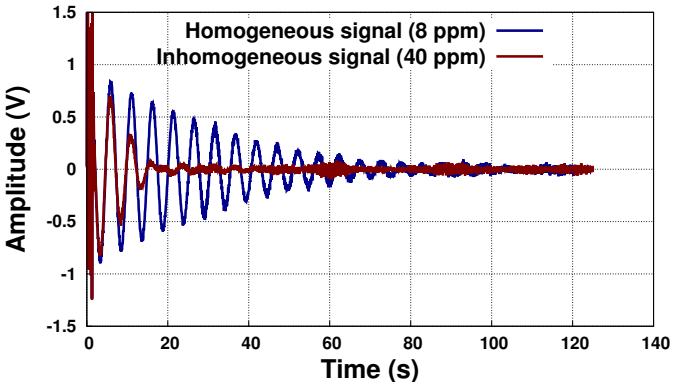

Figure 2.2: Free induction decay of two NMR signals in two different inhomogeneous fields.

Reducing the linewidth to its minimum intrinsic value $\frac{1}{T_2}$ is useful to perform images with a good resolution on a small bandwidth acquisition. Then we should always try to reach

$$\delta B \leq \frac{2\pi}{\gamma T_2}$$

In biological tissues , spin-spin relaxation time T_2 are of the order of 50 ms or less [3] which gives us $\delta B \leq 0.47\mu T$. For Very Low Field MRI (1 mT to 10 mT), this corresponds to a maximum homogeneity of 47 ppm. Based on those observations, two setups of different size have been used.

2.1.3 *Coils design*

The conception of an homogeneous field is a difficult problem which requires a specific mathematical framework. Based on the work of Roméo and Hoult [49], a simplistic introduction of the usual methods to perform such field optimization is presented here.

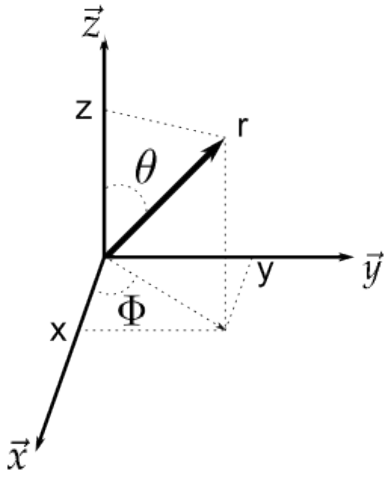

Figure 2.3: Spherical polar coordinates

In a volume through which no current passes, we know that a magnetic field $\vec{B}$ respects Laplace equation such as

$$\vec{\nabla}^2 \vec{B} = 0$$

Solutions of this equation in a spherical polar coordinates can be expressed as spherical harmonics of the form

$$T_{nm} = C_{nm} r^n P_{nm} cos\theta \begin{pmatrix} sin \\ \\ cos \end{pmatrix} m\Phi$$

where C_{nm} are constants, $P_{nm}cos\theta$ are Ferrer's associated Legendre functions and $n \geqslant m \geqslant 0$. Then any field generated by a current element can be expressed as a sum of spherical harmonics. It is then possible to think about relevant combination of current element in order to eliminate unwanted spherical harmonics while enhancing the harmonics of interest ($n, m = 0, 0$ in the case of an homogeneous field). This optimization of the field should always respect physical constrains of size and weight. Moreover the presence of unavoidable higher-order harmonics places an upper limit upon the volume over which the field is considered as a single harmonic.

2.1.4 *Small size setup*

This setup was build during Hadrien Dyvorne's thesis [18]. The geometry chosen for the small size setup is a rescale version of a magnet system for Low-Field Electron Paramagnetic Imaging imaging used by Rinard and Al [48]. This set of four coils have been optimized to ideally cancel unwanted harmonics until the $8th$ order.

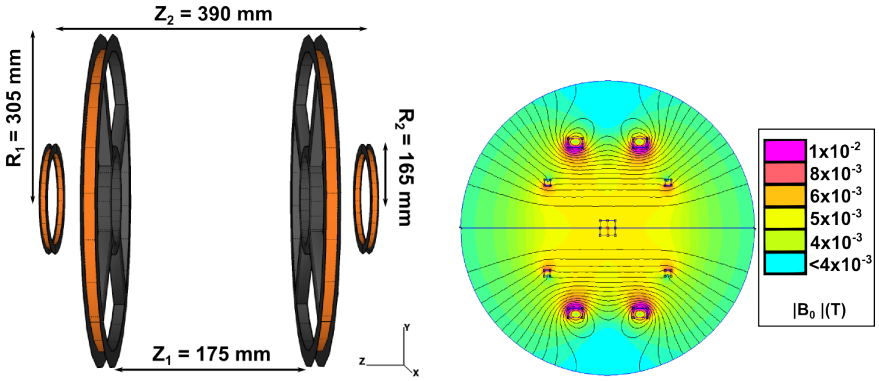

(a) (b)

Figure 2.4: a) Four-coil magnet that generates a permanent field B_0 along z axis and b) its magnetic field amplitude map in 2D using a finite element method simulation for a current of 10 A(FEMM 4.2)

This four-coil magnet design has been chosen as it is offering a large volume of magnetic field homogeneity for a rather compact and

open system compatible with the use of a cryogenic dewar. The two large inner coils C_L and the two small outer coils C_S are supplied by the same current, circulating in the same direction. Precise characteristics of each coil are described in Table 2.1.

Coil	Number of Turns	Wire Section	Turns/Layer	Total Section
C_L	120	2*6.5mm^2	5	48*32.5mm^2
C_S	30	2*6.5mm^2	3	20*19.5mm^2

Table 2.1: Winding parameters for the four-coil magnet

A finite element method software (FEMM 4.2) [15] is used to predict the generated magnetic field. Coils material, size, position and section are taken into account to obtain the Figure 2.5. The simulation is obtained for a circulating current of 10 A. It should be noticed that the final homogeneity depends also on the winding procedure which is considered as negligible in this ideal model.

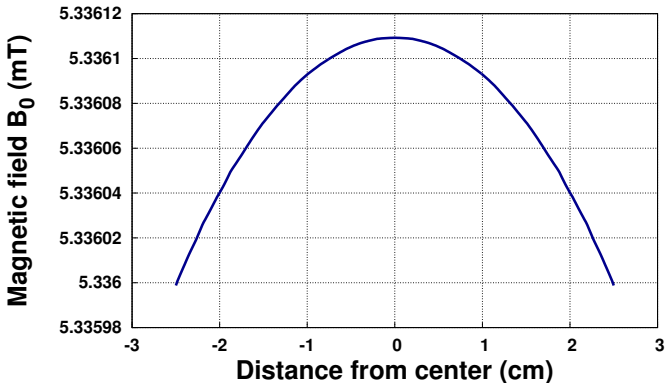

Figure 2.5: B_0 simulated profile along z axis for a current of 10 A

The simulation predicts a magnetic field per unit current around $B_0 \approx 5.33$ G/A with an homogeneity of 20 ppm over a 5 cm x 5 cm x 5 cm square sample. Coils are supported by a non magnetic aluminum structure. This metallic material could be sensitive to field change (see Chapter 2.2) but with a permanent polarization, no Eddy currents are created. Moreover, the magnetic noise coming from the thermal noise inside the aluminum has been evaluated and is less than 0.4 $fT/\sqrt{Hz}$.

A stable and low noise power supply is needed to achieve the theoretical homogeneity of 20 ppm. A DC supply Delta 1500W (model SM 35-45) has been chosen. It is well adapted given that the four-coil system has a total a resistance around 1 Ω.

Maximum voltage	Maximum current	Current stability	Ripple current noise
35 V	45 A	$9 * 10^{-5}$ A/h	15 mA

Table 2.2: Delta SM 35-45 characteristics

In Table 2.2, the peak to peak ripple current noise is measured on a bandwidth of 50 MHz. It is rather high and it leads to an important homogeneity degradation. A 20 ppm homogeneity at 10 mT requires an equivalent ripple current noise of 380 μA or lower. The main part of this ripple noise comes from 50 Hz and 100 kHz harmonics (MOSFET power conversion frequency).

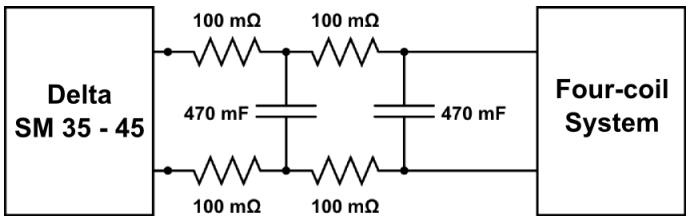

Figure 2.6: RC Filter to minimize power supply ripple current noise

A RC filter (Figure 2.6) is added to the power supply to filter those perturbation. The ripple current noise is divided by a factor 20 ($\approx 760\mu A \equiv 40$ ppm). At 1 mT, this current perturbation involves a degradation of the homogeneity up to 400 ppm. It remains the main limitation of our permanent polarization and the current drift of $9 * 10^{-5}$ A/h is negligible even for long acquisition time ($\lesssim 8$ hours).

2.1.5 *Full size setup*

This particular system has been planed to be able to make in-vivo imaging of a human brain. The design has been chosen with the help of a private company *Cedrat*. It was necessary to have a rather good homogeneity on a large volume with an open and compact geometry. The patient-friendliness criteria was defined as a large free area in his field of view in order to minimize enclose feelings and subsequent claustrophobic effects. It has been assume that a 90° free vision angle was sufficient.

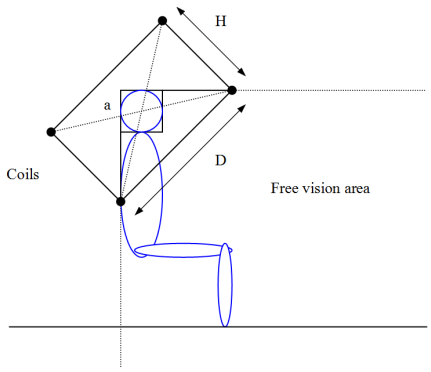

Figure 2.7: Schematic of the proposed patient-friendly structure

A three-coil Maxwell configuration was first proposed but it was not respecting the patient-friendliness criteria. The height of this configuration was modified to fulfill this condition and then the central coil size and Ampere-turn in each coil were optimized to reach the best homogeneity at 10 mT (see Figure 2.8). The configuration has been built horizontally for a better ease of use but could be adapted vertically.

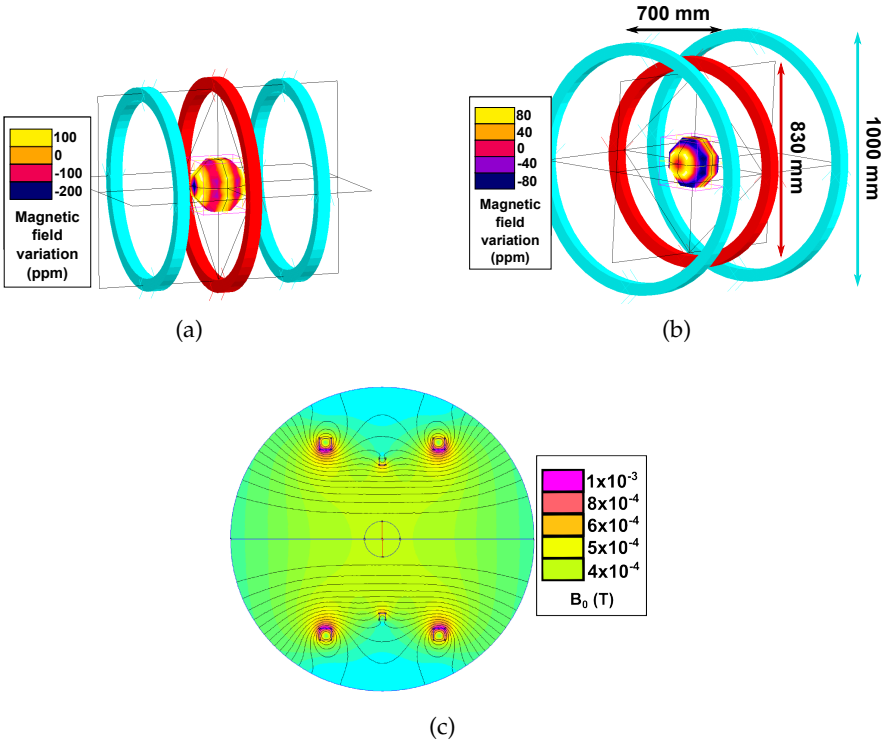

(a) (b)

(c)

Figure 2.8: a) Classic three-coil Maxwell configuration b) Optimized three-coil configuration and c) its finite element method simulation of B_0

The entire structure to maintain the coil is in wood which excludes all parasite effects of conducting material like Eddy currents or extra

magnetic noise. The same current is applied on both external coils, in the same direction. The current circulating in the central coil is lower but also in the same direction. The ratio is

$$Ratio = \frac{I_{central}}{I_{external}} = 0.56$$

The considered working zone is a sphere with a diameter of 20 cm at the center of the structure. The total winding mass is around 180 Kgs and an integrated cold loop provide efficient cooling for the dissipated power (1,4 kW).

Coil	Wire diameter	Number of turns	Total section
Central	1.4 mm	72	35*35 mm
External (data for 1 coil)	1.4 mm	280	65*65 mm

Table 2.3: Winding parameters for the three-coil magnet

A finite element method simulation is performed again with a current of 1 A (Figure 2.8). A magnetic field profile is measured along x in the working zone (Figure 2.9).

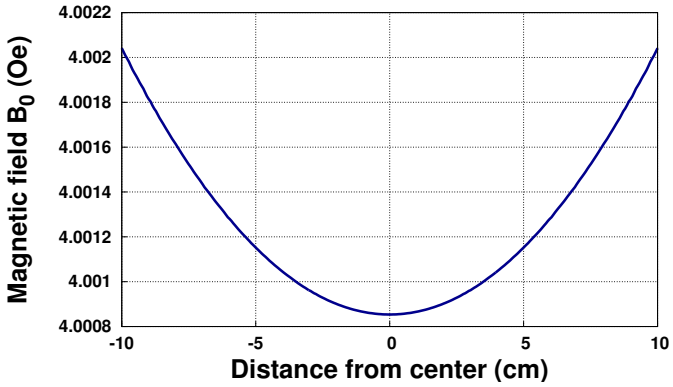

Figure 2.9: Magnetic field B_0 profile along x

On a sphere of 10 cm radius, the FEMM simulation predicts a magnetic field around $B_0 \approx 5.3$ G/A with an homogeneity of 150 ppm with a perfect current source. The real current source brings some more perturbations that need to be taken into account. For the total resistance of 3.588 Ω, a Delta 1500 W (SM 70-22) has been chosen.

Maximum voltage	Maximum current	Current stability	Ripple current noise
70 V	22 A	$9 * 10^{-5}$A/h	10 mA

Table 2.4: Delta SM 70-22 characteristics

Another RC filter has been added to the power supply to filter the ripple current noise.

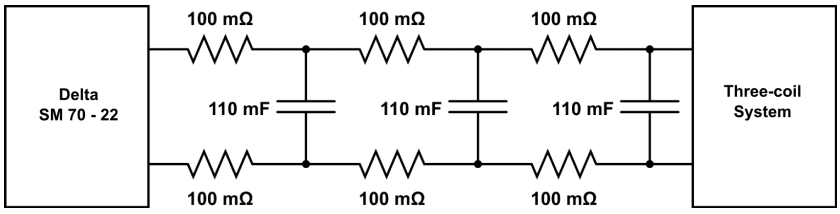

Figure 2.10: RC Filter to minimize power supply ripple current noise

2.1.6 *Measurements of strength and homogeneity*

Nuclear Magnetic Resonance is a powerful tool to evaluate magnetic field properties. For both setup, the same procedure has been used to measure the strength of the magnetic field B_0 and its homogeneity. A sample, corresponding to the working volume of the system, is positioned at the center and filled with pure water : a square of 5x5x5 cm^3 for the small setup and a sphere with a radius of 15 cm for the full-head setup. A tuned coil is used here as detection with a resonance frequency of 300 kHz for the small setup and 190 kHz for the full-head setup. Our first experiment is to find the current to generate a field corresponding to the Proton Larmor Frequency adapted to the tuned coil. A single $\frac{\pi}{2}$ pulse is applied on the sample with a repetition time of 1 second. For a precise value of current, an NMR signal should appear at 300 kHz (or 190 kHz for the full-head setup) on our monitoring devices (see Chapter 2.3). This gives us a precise measurement of the signal strength in function of the current circulating in the coils.

	Magnetic Field Strength Predicted	Magnetic Field Strength Measured
Small Size Setup	5.1 G/A	4.6 G/A
Full Size Setup	5.3 G/A	4.7 G/A

Table 2.5: Magnetic field strength of both experimental setup

As we have seen before, the inhomogeneity inside a sample is translated into a transverse relaxation time change. This relaxation can be directly measured by the half-height linewidth of the NMR signal Fourier Transform. It is of prime importance to use a sample with a long T_2 ($\geq$ 250 ms) to avoid any intrinsic transverse relaxation limitation. The small setup has been tested at 7 mT and the full size setup has been tested at 4.4 mT. A spherical phantom has been used for the full-head setup. In both setup, the Free Induction Decay width has

been measured for 1 acquisition and for 300 averaged acquisitions to evaluate the current supply noise impact.

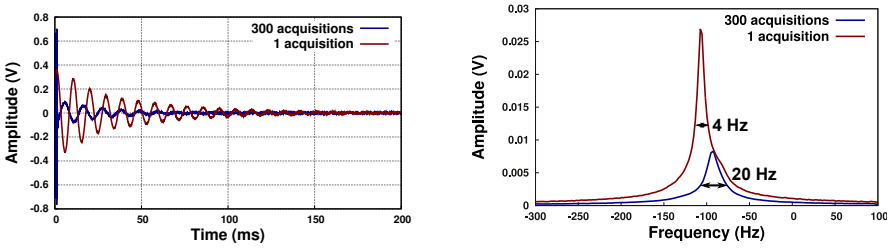

(a) (b)

Figure 2.11: Inhomogeneity measurements in the small size setup for one acquisition and 300 acquisitions. a) The Free Induction Decay and its b) Fourier Transform.

The half-height linewidth can then be translated into an inhomogeneity level. The difference between the measurement for one acquisitions (4 Hz) and 300 acquisitions (20 Hz) comes mainly from the ripple current noise coming from the current supply. Those punctual variations participate to the widening of the peak.

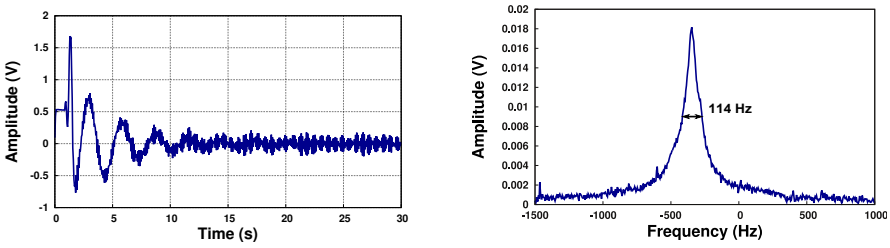

(a) (b)

Figure 2.12: Inhomogeneity measurements in the full-head setup for 300 acquisitions. a) The Free Induction Decay and its b) Fourier Transform.

For the full-head setup, no differences were measured for one acquisition or 300 acquisitions. It corresponds to a linewidth of 114 Hz. All results are combined in Table 2.6.

	Linewidth for 1 acquisition	Inhomogeneity for 1 acquisition	Linewidth for 300 acquisitions	Inhomogeneity for 300 acquisitions
Small size setup (7 mT)	4 Hz	8.5 ppm	20 Hz	42.5 ppm
Full size setup (4.4 mT)	114 Hz	600 ppm	114 Hz	600 ppm

Table 2.6: Inhomogeneity measurements

Any MRI acquisition requires averaging. Thus the relevant inhomogeneity measurement is given after 300 acquisitions. It should be pointed out that the small setup was tested in different environments : a classic laboratory and a non-magnetic building. No differences were measured after 300 acquisitions confirming that the current supply is the main limitation here.

The inhomogeneity measured for the full size setup is much larger than the simulation. It is mainly due to an error in the Ampere-turn ratio between the central coil and external coils. It has been compensated using parallel resistances but the precision is limited.

2.2 GRADIENTS AND RF PULSES

Linear gradients are essential for precise MRI acquisitions. The required strength and linearity needed for very low field applications are discussed here. Three different gradient designs are presented. Each one of them is adapted to one particular MRI setup. Their geometry is described and a characterization of their strength and linearity is also given. Finally, an RF coil design is proposed to fulfill precise requirements previously defined. Its homogeneity is then experimentally measured.

2.2.1 *Gradient specificity*

Unlike permanent field, gradients need to be switch off and on during an MRI acquisition and require reasonable amplitude. At high fields, gradients amplitude up to 100 mT/m can be used. For those reasons, resistive electromagnets are perfect candidates to generate such fields. An important drawback of those gradients at high field is the acoustic noise. The alternation of currents in the presence of the strong static field produces significant Lorentz forces that act upon the gradient coils. Then motion and vibration of gradients generate an acoustic noise typically around 90 dB. But those noises depend on the strength of gradients. At low field, their amplitude is lower and so is the resulting acoustic noise. Moreover, currents alternation often comes with Eddy currents which implies dedicated active screening for such gradients to minimize perturbations. This problem is also greatly reduced at low fields.

In both developed setup, gradients are also used as active shimming coils. Permanent external inhomogeneity can be compensated by sending a DC current inside coils.

2.2.2 *Gradient strength and linearity required*

The gradient strength G is determined by the resolution δr we want to achieve in addition to the fundamental linewidth δv of our NMR signal. As we have already seen in Chapter 1.2,

$$G = \frac{2\pi}{\delta r \gamma T_2^*} = \frac{2\pi \delta v}{\delta r \gamma}$$

We understand here the importance of a good homogeneity. A low amplitude gradient sharpens the acquisition bandwidth, increases the signal-to-noise ratio, lowers the acoustic noise and reduces parasite eddy currents. The relative homogeneity at low field is approximately the same as at high field. It means that we have a linewidth 150 times lower at 10 mT if we neglect the intrinsic linewidth of our

product (100 ms ≈ 10 Hz). We should then require a gradient amplitude around 1 mT/m.

Another important point is linked to the linearity of gradients. Due to the reconstruction pattern (Fast Fourier Transform), a cartesian acquisition of the K-space is extremely important to obtain a correct image.

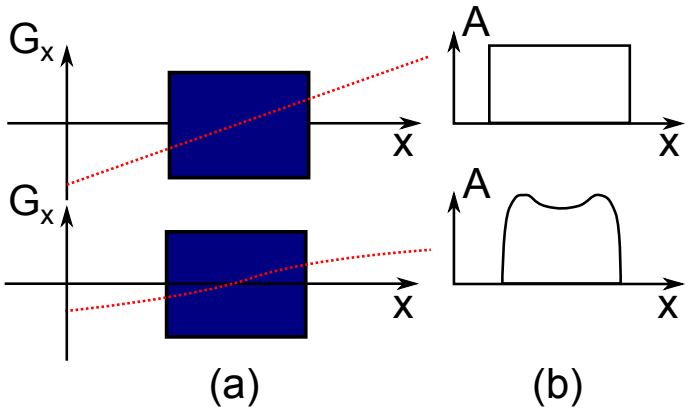

Figure 2.13: (a) Two similar square samples are acquired in one dimension along x with two different gradients. (b) The resulting images are given for the linear and the non linear gradient.

Any deviation from a perfect linear gradient will result in a deformation of our image. At a point (x,y,z), the non-linearity $\delta G_{norm}(x,y,z)$ of a gradient is defined as the normalized difference between its actual value and its ideal value

$$\delta G_{norm}(x,y,z) = \frac{B(x,y,z) - B_{ideal}(x,y,z)}{B_{ideal}(x,y,z)}$$

The parameter we are considering is the maximum absolute value of this non-linearity on the working volume $\mid \delta G_{norm} \mid_{max}$. Most of the time, this maximum concerns the surface of the working volume. It is important to notice that gradients non-linearity is not a random perturbation like regular noises. On one hand it means that gradients non-linearity will always dominate the background external noise at some point after enough averaging. On the other hand some reconstruction algorithms can be used to compensate an important δG_{norm}. The optimization of such field is based on the same principle than for a permanent field. However, the relevant harmonic corresponds to $n, m = 1, 0$ for a linear gradient.

2.2.3 *Small size setup*

A specific geometry has been chosen to satisfy the problematic of this small size setup. Because of the screening effect of the aluminum frame of the B_0 coils, the gradients have to be placed between the permanent coils structure. The main field homogeneity of 47 ppm at

10 mT imposes a minimum amplitude limit. A gradient strength as high as 0.4 mT/m to reach a 1 mm resolution is required. The three directions gradients are generated by using two different coil design.

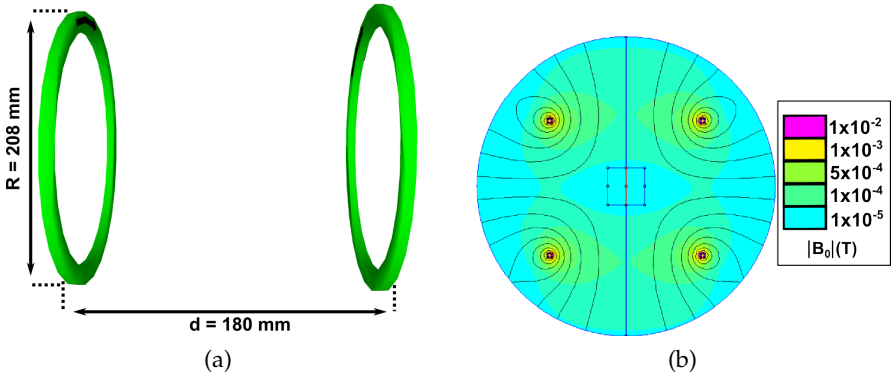

(a) (b)

Figure 2.14: (a) Gradient field along Z and (b) the FEMM simulation

Circular Maxwell coils are used to create the gradient field along z direction. The cancellation of harmonics until the fourth order is obtained if their centers are spaced by a distance $d = R\sqrt{3}$ where R is the coil radius. A finite element method simulation is performed with FEMM 4.2 to determine our linearity and strength.

d	R	Number of turns	Z gradient strength	Gradient linearity
180 mm	104 mm	30	2.2 $mT.m^{-1}.A^{-1}$	9.10^{-3}

Table 2.7: Parameters of the Maxwell coils for the small size setup

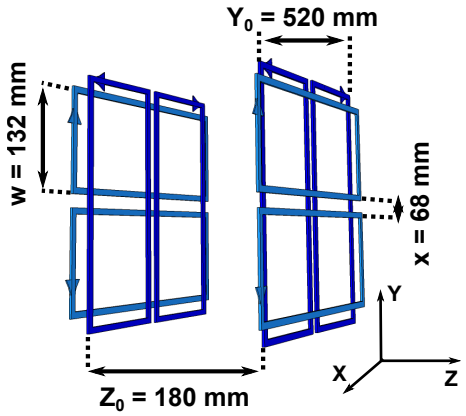

Figure 2.15: Gradient coils to encode along direction X (dark blue) and Y (light blue).

Rectangular planar coils are used to create the gradient fields along x and y directions. Inspired by [5], those gradients are perfectly adapted to the small size geometry as the central zone remains easily accessible. A simulation using FLUX [1] is performed.

Number of turns	X and Y gradient strength	Gradient linearity
10	$0.7\ mT.m^{-1}.A^{-1}$	6.10^{-3}

Table 2.8: Parameters of rectangular coils

The three supplies output deliver ± 20 V and up to ± 3 A with a rise time of few μs. The switching limitation is coming from the intrinsic inductance of our gradient coils which are limiting the rise time to few ms. An RC filter is also added to each supply in order to attenuate the high frequency noise injected inside the system.

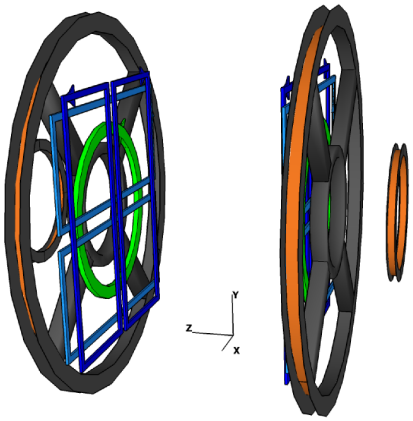

Figure 2.16: Small size setup with permanent coils (in orange) and gradient coils (X : dark blue, Y : light blue, Z : green).

We finally obtain an open system which is adapted to the use of a dewar close to the sample. The entire setup is inside an aluminum box. This "shield" of 3 mm thick has been designed to attenuate all radio-frequency laboratory perturbations.

2.2.4 *Full size setup*

The full size setup has a cylindrical geometry. The gradients have been designed to respect this particular shape and to offer a maximum space for experiments and patients. According to the previous section, we have an homogeneity around 600 ppm at 10 mT which imposes a gradient as high as 4.8 $mT.m^{-1}$. As for the small size setup, two different coil designs have been used.

Circular Maxwell coils are used again to generate a gradient field along z direction. As for the small size setup, this geometry cancels harmonics until the fourth order. The ratio $d = R\sqrt{3}$ is respected like in 2.14 however dimensions have changed.

d	R	Number of turns	Z gradient strength	Gradient linearity
693 mm	400 mm	10	0.15 $mT.m^{-1}.A^{-1}$	9.10^{-3}

Table 2.9: Parameters of the Maxwell coils for the full size setup

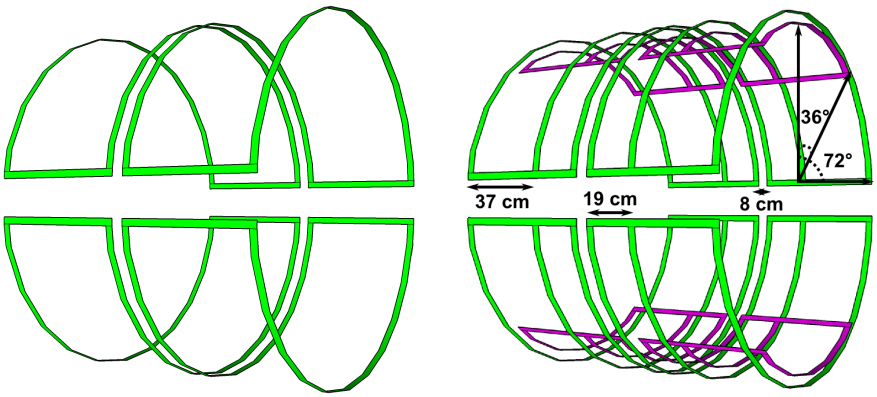

(a) (b)

Figure 2.17: a) Classic gradient saddle coils and b) Double split saddle coils to encode along X direction. The same set of coils rotated by 90° would encode along Y direction.

Double split saddle coils are used to generate a gradient field along x and y directions. Usually, simple saddle coils are enough to generate a linear gradient in a decent working volume. However, due to fabrication constrains, the entire length had to be below 1.25 meters. According to [53], this variation of the classical saddle coil geometry cancels unwanted harmonics up to the eights order with compact geometry. It is called double split saddle coil because of the angular split and the internal arc split. Based on this study, we have determined specific dimensions adapted to our system. In Figure 2.18, we can see that each coil has one external arc (K_{ex}) and two split internal arcs (K^1_{int} and K^2_{int}).

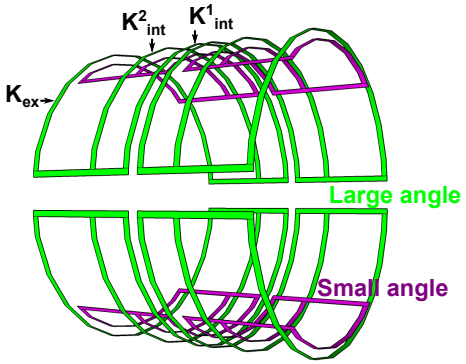

Figure 2.18: Double split saddle coils : geometry details

They respect a specific ratio in number of turns such as

$$N(K_{ex}) = N(K^1_{int}) + N(K^2_{int}) \; and \; \frac{N(K^2_{int})}{N(K^1_{int})} = 2.3$$

Moreover each coil has a large angle version (green coils) and a low angle version (violet coils). They also respect a specific ratio in number of turns

$$\frac{N(green)}{N(violet)} = 1.6$$

Finally, this entire set generates a gradient along X. A similar set can be added and rotated at 90° to generate a similar gradient along Y.

Radius	Number of turns $N(K_{ex})$	X gradient strength	Gradient linearity
40 cm	10	0.12 $mT.m^{-1}.A^{-1}$	$\geq 1\%$

Table 2.10: Parameters of the double split saddle coils for the full size setup

Three AE Techron (7224) output supplies are used with a slew rate of 70 $V/\mu s$ and a power amplification of 1 kW. An RC filter is also added to each supply in order to attenuate the high frequency noise injected inside the system.

2.2.5 *Strength and linearity measurement*

The strength and the linearity of each geometry have been predicted by simulations and we want to verify those values experimentally. The widening bandwidth of our NMR signal during a gradient application is linked to its strength and we have

$$G_x = \frac{2\pi * Bandwidth_{Sample}}{d * \gamma * I}$$

where I is the current supplied to the coils, γ the gyromagnetic factor and d the size of the sample along the readout direction. All gradients are tested at 7 mT for the small setup and 3.3 mT for the full-head setup. A water sample of 2 cm radius is first used to evaluate the strength in both setups. A 1 mm resolution in one dimension is targeted and then a straight measurement of the injected current gives us the actual gradient strength.

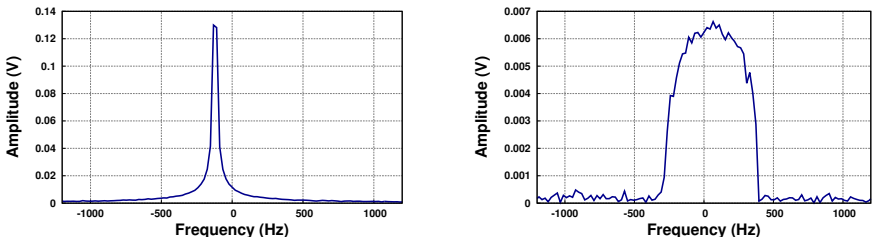

(a) (b)

Figure 2.19: Measurement of the gradient z strength in the small setup. a) The NMR signal after an echo without gradients gives the resolution bandwidth (1 point = 20 Hz). b) The z gradient widened the signal to achieve a 1 mm resolution (4 cm = 40 points = 800 Hz).

In Table 2.11, we see that our measurements are consistent with predictions. To test the linearity of our gradients, we have imaged a square phantom of 5 cm x 5 cm x 5 cm composed of 4 smaller square of 2.5 cm x 2.5 cm x 2.5 cm filled with doped water (Figure 2.20). A tuned coil is used to perform those measurements. Gradients are set to achieve a 1 mm resolution. For the small setup, we work at 7 mT in one dimension. For the full-head setup, we work at 3.3 mT and we move the square to test the entire working volume. Any deviation in gradients linearity will result in a modification of the shape between squares. Some intensity variation exists because of tuned coil filtering and excitation pulse bandwidth.

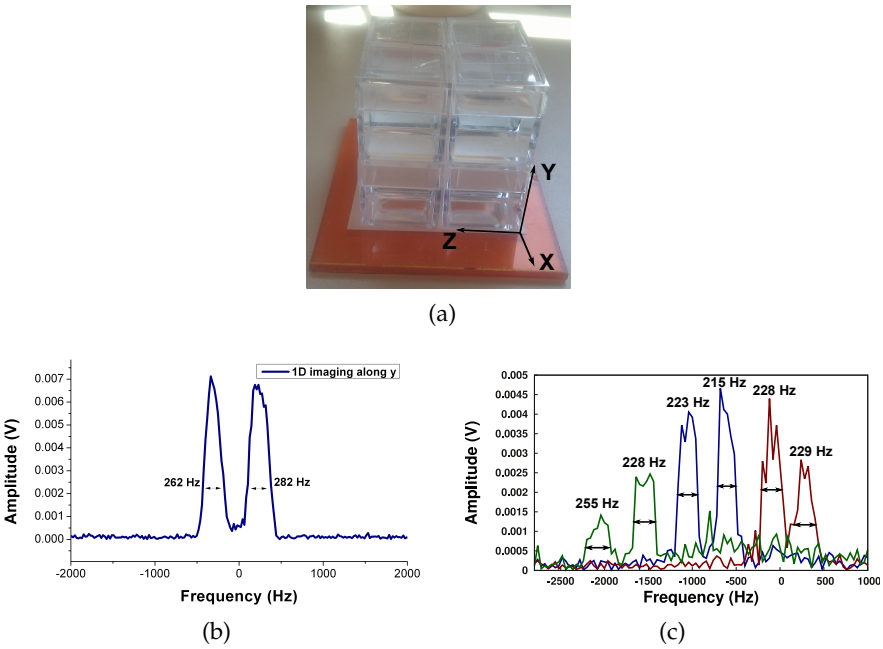

(a)

(b)

(c)

Figure 2.20: a) Square sample and b) its one dimensional representation along y direction in the small setup c) several one dimensional images along y direction in the full-head setup (Green = right ; Blue = Central ; Red = Left)

The linearity is directly measured on our image profile as the normalized absolute deviation of bandwidth between all square sides.

$$\delta G_{norm} = \frac{\mid BW_{left} - BW_{right} \mid}{BW_{total}}$$

For exemple, Y gradient on the small setup has a linearity error of

$$\delta G_{norm} = \frac{282 - 262}{1000} = 2\%$$

We performed also two dimensional imaging to check any effect of concomitant gradient. No significant influence was measured.

	Small size G_z	Small size G_x/G_y	Full size G_z	Full size G_x/G_y
Measured Strength $(mT.m^{-1}.A^{-1})$	2.2	1.1	0.11	0.14
Measured Linearity error	2 %	2 %	1%	1%

Table 2.11: Measured parameters of both setup gradients

All gradients have been experimentally tested and respect requirements for very low field MRI.

2.2.6 *RF coil*

An RF coil has to generate an homogeneous field B_1 at the Larmor frequency ω_0 to tip the sample's magnetic moment. We chose to uncoupled this emission coil to the detection coil to avoid any saturation of the preamplifier. Then both coils are orthogonal to each other in a quadrature position. The tip angle α is defined by

$$\alpha = \gamma B_1 \tau$$

where γ is the gyromagnetic factor and τ the pulse time. To achieve precise excitation angle, the pulse time has to be much larger than the period of the proton nutation such as

$$\tau \gg \frac{2\pi}{\gamma B_0}$$

where B_0 is the permanent field applied on the sample. However, the time τ should not be too large as it impacts the acquisition time. Finally, we should maximize B_1 and respect

$$B_1 \ll \frac{B_0}{4}$$

At 10 mT, it implies a RF field amplitude of order 100 μT . Any inhomogeneity of B_1 will result in intensity perturbations. If we consider that we can tolerate an error close from gradients inhomogeneity, a voxel should present an intensity variation below 3 % at 10 mT to be negligible. This corresponds to an angle error

$$\delta\alpha = arccos(\frac{0.97 * M_0}{M_0}) = 14°$$

where M_0 corresponds to the longitudinal magnetic moment at equilibrium. Then we have

$$\frac{\delta B_1}{B_1} = \frac{2\delta\alpha}{\pi}$$

In our case, this corresponds to an inhomogeneity of 15 %. An untuned saddle coil is a perfect candidate to generate such field [29].

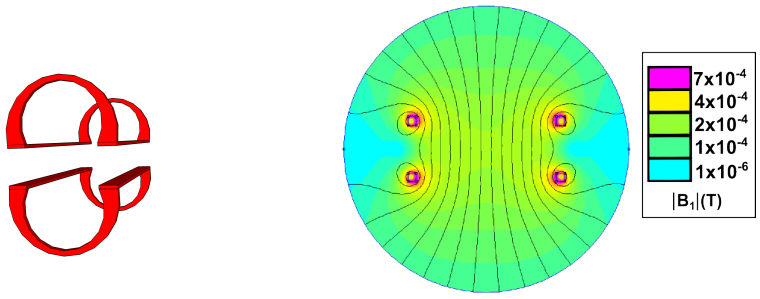

(a) (b)

Figure 2.21: a) Saddle coil for RF pulses and b) its simulated field map

An experimental B_1 mapping is performed using a double angle method [16]. We acquire two gradient echo images with flip angles α and 2α. Both images have a different magnetization such as

$$M_{xy,\alpha} = M_0 sin(\alpha)$$

$$M_{xy,2\alpha} = M_0 sin(2\alpha)$$

Then the ratio removes the M_0 dependence and we have

$$\alpha = cos^{-1}(\frac{M_{xy,2\alpha}}{2 * M_{xy,\alpha}})$$

A tip angle α map is obtained and the B_1 homogeneity can be deduced from it.

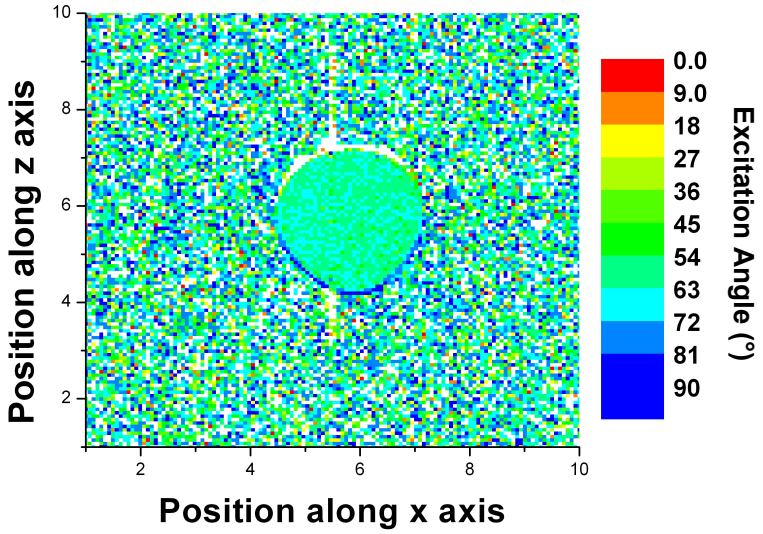

Figure 2.22: Two dimensional B_1 mapping of a plastic bottle excited with an angle $\alpha = 45°$

The angle variance observed inside the bottle is mainly due to background noises. A mean value is measured at the center and at limits of the working volume. The resulting properties of the small size RF coil are given in Table 2.12.

Number of turns	Field per unit current	Inhomogeneity
5	1 G/A	4%

Table 2.12: Parameters of a simple saddle coil for RF pulses

This RF emission free from any capacitors generates a field B_1 that varies slowly with frequency. The pulse amplifier used is a TOMCO BT-01000 series delivering a maximal outpout power of 1kW. It has an output impedance Z of 50 Ω. The circuit impedance Z_0 is matched to

minimize the power reflexion coefficient for an optimal transmission such as

$$Z = Z_0 = L\omega_0 = 50\Omega$$

An untuned RF system can be used with different kind of sensors with limited disturbance in B_1 field.

2.3 RMN SPECTROMETER

The homemade spectrometer that has been used during my thesis is presented here. It has been separated in three main parts : the emission part, the reception part and the gradients part. Electronic components and their functions for MRI are described to enlighten capabilities and limits of this setup.

2.3.1 *Emission part*

The excitation pulse B_1 is generated by the emission part of the spectrometer and then amplified by an RF amplifier (TOMCO BT-01000). Parameters of interest for this pulse are its amplitude, its phase, its frequency and its application time.

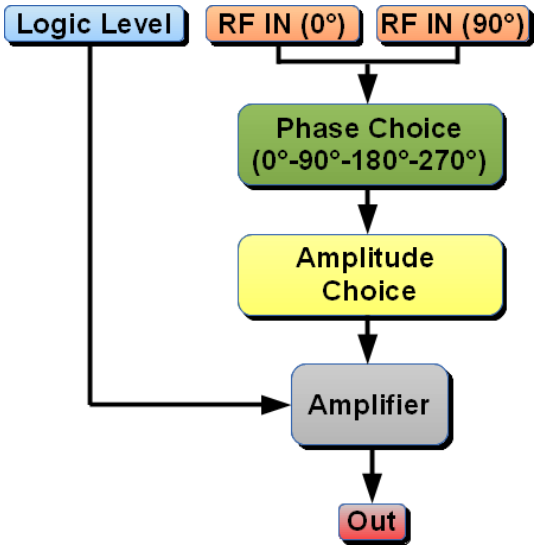

Figure 2.23: Emission chain

The amplitude can be modulated in 2048 steps and the phase can be chosen between 4 values (0°,90°,180°,270°,360°). The generated pulses have the frequency of the RF IN signal generated by a Low Frequency Function Generator (Agilent 33522A) and are applied according to the logic level. This way we can program sequences complex enough for many applications.

2.3.2 *Reception part*

The NMR signal is measured by our sensor which is connected to a complex detection chain including a preamplifier (see Chapter 3), an homemade spectrometer (reception card) and an acquisition card.

Figure 2.24: Acquisition chain from the sensor to the computer

The reception card has several functions (see Figure 2.25).

A protection level is here to keep safe electronic components of the spectrometer.

An amplification can be chosen between 4 different values (1,5,10,50). According to the used sensor, we can change our amplification level to minimize the noise weight of subsequent electronic devices.

A demodulation is applied at a precise working frequency (the Larmor frequency) that we choose through the same Low Frequency Function Generator (Agilent 33522A) that is used for the emission. Thus the emission and the reception are coupled. The signal is demodulated in two different signals, one in phase and one in quadrature. This way, we acquire two channels corresponding to a real and an imaginary part of the same signal and the noise is reduced.

A low-pass filter is finally applied with a cutoff frequency at 10 kHz. This filter level is important to avoid any aliasing effect and to obtain a smoothed signal.

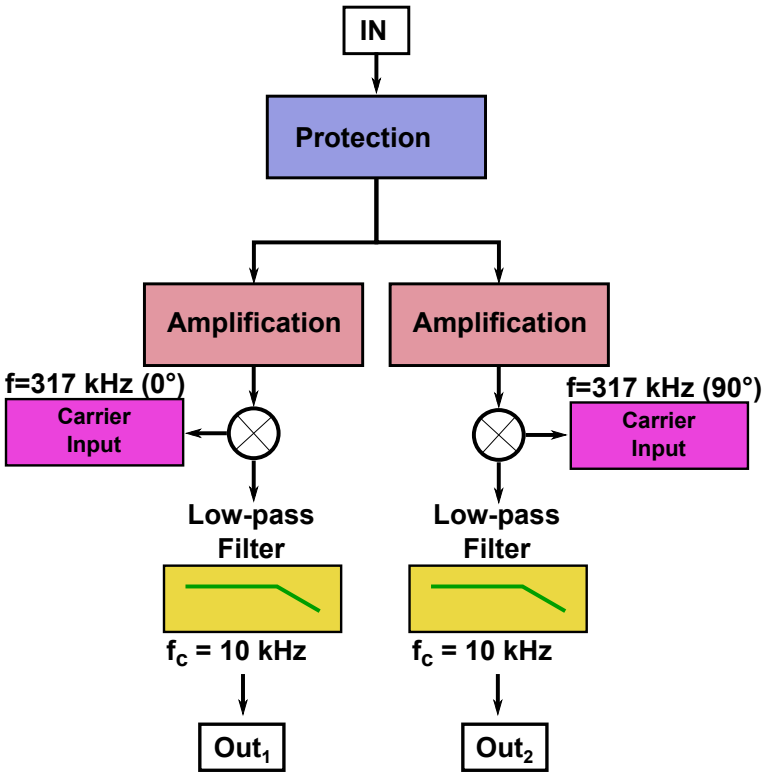

Figure 2.25: Reception Card

The signal is then acquired on an acquisition card (DT9836 Series).

2.3.3 *Shims and Gradients*

Shims are specific coils used to adjust the homogeneity of a magnetic field. Indeed, permanent inhomogeneity of the environment can not be shielded and then must be compensated. Instead of dedicating a new set of coils to that purpose, both very low field setup are using gradient coils as shims. It implies the development of a specific spectrometer control of gradients.

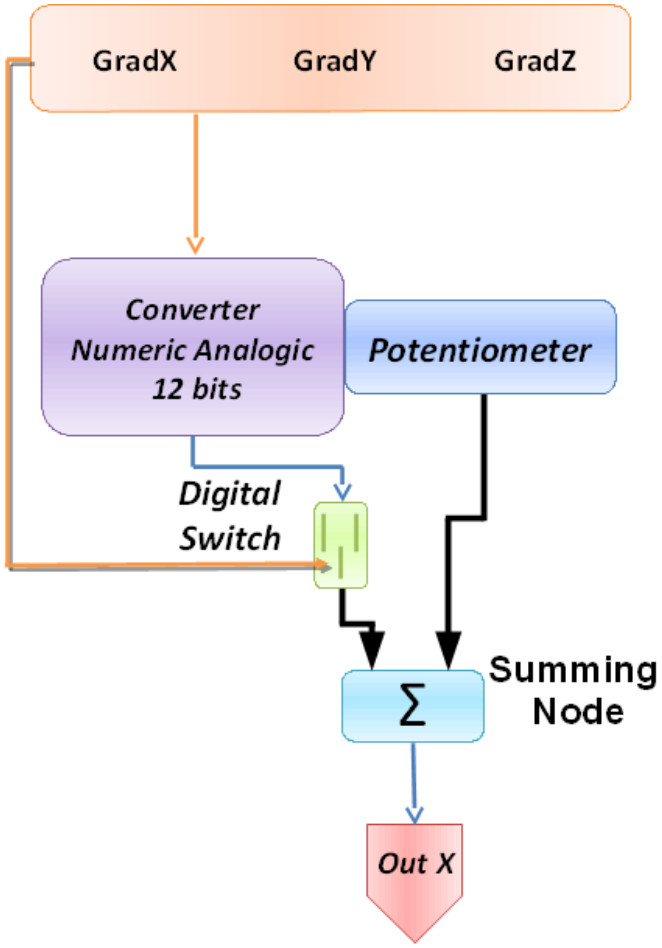

Figure 2.26: Gradient Card

Gradients are controlled by a potentiometer and a numerical signal generated by the computer. Both are then added up and amplified by the power supplies (see Section 2.2). The potentiometer set a permanent DC current inside gradients to correct external inhomogeneity. The numerical signal set an intermittent DC current inside gradients to encode our sample according to a chosen sequence.

CONLUSION

Two MRI setups have been entirely characterized. The small one has been modified from the previous version made by Hadrien Dyvorne [18]. It has been integrated to the homemade spectrometer with new current supplies and filters in order to achieve requirements of very low field. Finally, we obtain a working MRI device adapted for imaging volume of 5x5x5 $cm^3$with a resolution of 1x1x1 mm^3. The linearity and the homogeneity are respectively of 2 % and 43 ppm. This structure is adapted for the use of a cryogenic dewar and will be employed to test sensors and sequences. A new full-head MRI device has been built and is adapted for imaging spherical volume with a radius of 7.5 cm. A 1x1x1 mm^3 resolution is achieved and the linearity and the homogeneity are respectively of 1% and 600 ppm. It should be adapted for future in-vivo brain imaging applications.

Finally, the homemade spectrometer has been designed to acquire low field NMR signals coming from tuned coils or mixed sensors. It is controlling gradients and excitation pulses to allow advanced sequence programming.

3

FEMTOTESLA SENSORS

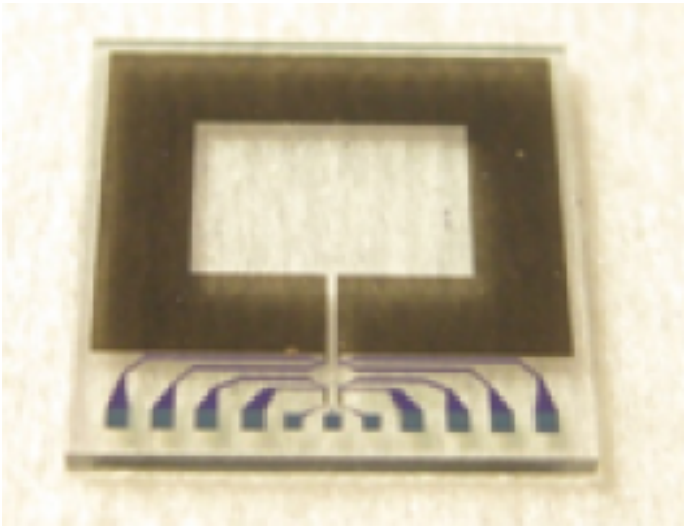

Mixed sensor of 1 cm^2

Very Low Field MRI requires highly sensitive devices. Unlike high field MRI, the dominant noise at those frequencies comes from sensors. It is then of prime importance to optimize them to reach high Signal to Noise Ratio. In this Chapter, we will see different existing techniques for magnetic detection at low frequency. The detectivity of tuned coils, SQUIDs and atomic magnetometers will be compared as well as their properties. Then a complete description of the mixed sensor used in this thesis will be developed.

3.1 TUNED COILS

There are several ways of detecting a NMR signal. In this section, tuned coils are introduced. Its efficiency for very low field MRI applications is evaluated through the description of Faraday sensor principle. Then a simulation of its detectivity is performed and and validated by experimental measurements. Afterward it is incorporated in the small setup to test its robustness in a MRI environment. Finally, a NMR signal is acquired with this sensor.

3.1.1 *RLC Circuit*

Tuned coils are commonly used in high field MRI as they present a strong detectivity at high frequencies. Moreover they are passive devices, inexpensive to develop and easily adjustable. At low frequencies, this superiority is contested due to their typical characteristics. A description of their behavior is then necessary to highlight strength and weakness of such sensors.

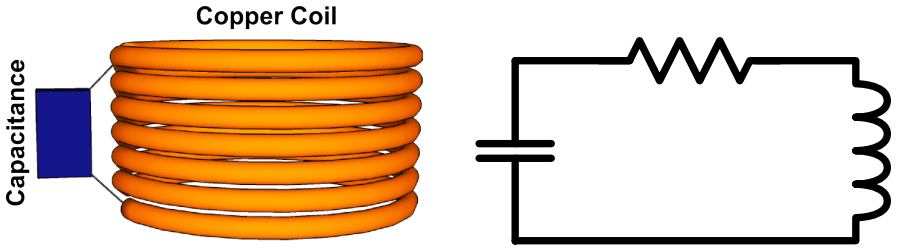

(a) (b)

Figure 3.1: a) Three dimensional model of a tuned coil and b) its schematic representation

A tuned coil is the combination of a copper coil with a capacitance (Figure 3.1). This RLC circuit has a resonant frequency ω_0 defined as

$$\omega_0 = \frac{1}{\sqrt{LC}}$$

where L and C are respectively the inductance and the capacitance of the tuned coil. It corresponds to the frequency where the total impedance of the circuit is minimal

$$Z(\omega_0) = jL\omega_0 - \frac{j}{C\omega_0} + R = R$$

where Z is the total impedance of the circuit, R its resistance and j the imaginary unit. A magnetic flux Φ through this sensor will generate a potential V which obeys to Faraday's Law

$$N\frac{d\Phi}{dt} = V = ZI_{signal}$$

where I the current passing through it and N the number of turns of the coil. At resonance, the current circulating in the tuned coil will be maximum such as

$$I_{signal} = \frac{\omega N \Phi}{R}$$

The measured signal is the potential at the terminal of the capacitance

$$V_{signal} = \frac{1}{C\omega} I_{signal} = N \frac{L\omega^2}{R} \Phi$$

A decisive parameter for a tuned coil is the quality factor Q which is defined as

$$Q = \frac{L\omega}{R}$$

It characterizes the amplification level of the tuned coil at resonance. It is also linked to the bandwidth detection of the sensor such as

$$Q = \frac{\omega_0}{\Delta\omega}$$

where $\Delta\omega$ is the half-power bandwidth (see Figure 3.2). Finally, we have

$$V_{signal} = N * Q * \omega\Phi$$

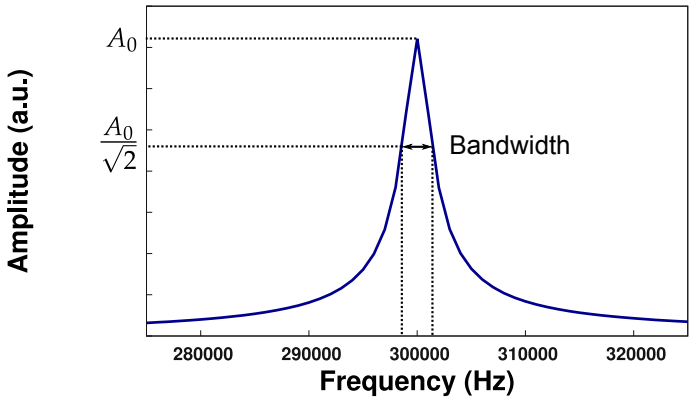

Figure 3.2: Bandwidth of a tuned coil

In a tuned coil, there are three main noise sources : the thermal noise, the sample noise and the preamplifier noise. In regard to Chapter 1, we can consider the sample noise as negligible here. The thermal noise can be described as

$$\sqrt{4k_b RT} = ZI_{noise}$$

Then the measured noise at resonance is

$$V_{noise} = \frac{1}{\omega C} I_{noise} = Q\sqrt{4k_b RT}$$

The signal-to-noise ratio with this sensor can be expressed as

$$SNR = \frac{V_{signal}}{\sqrt{V_{noise}^2 + V_{preampli}^2}}$$

where $V_{preampli}$ is the voltage noise of the preamplifier. Then, at resonance

$$SNR = \frac{N\omega\Phi}{\sqrt{4k_bRT + (\frac{V_{preampli}}{Q})^2}}$$

Working with a high Q factor is then essential for two reasons : to overcome the preamplifier noise and to reduce the thermal noise coming from the resistance R. The number of turns is limited because of the parasite capacitance it adds and the size of the coil which should fit the sample.

The resulting bandwidth needs to be adapted for low field MRI. In the small setup seen previously, we typically work with 3 kHz bandwidth which correspond to a maximum quality factor of 14 at 1mT (140 at 10 mT). Those values are close to high field typical quality factor. A non adapted bandwidth would result in a loss in signal-to-noise ratio on edges of the image.

3.1.2 *Detectivity*

Figure 3.3 presents our typical tuned coil detection setup.

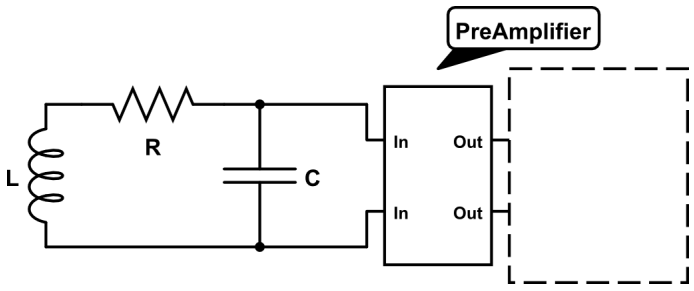

Figure 3.3: Electrical circuit of a tuned coil for MRI measurements

The signal coming from the tuned coil is amplified by a NF SA-421F5 preamplifier. Its input voltage noise density $V_{preampli}$ is around 0.5 $nV/\sqrt{Hz}$. Its input noise current density is around 100 $fA/\sqrt{Hz}$ which is negligible in regards to the tuned coil impedance. A 50 turns Faraday sensor of 6 cm diameter with an inductance of 250 μH is introduced in the small MRI setup. We consider a capacitance C in parallel so that the circuit resonates at 300 kHz. A simulation is performed before experimental measurements. We consider a magnetic field B_{signal} applied on a tuned coil with a detection surface A such as $\Phi = B_{signal} * A$. The measured value V_{signal} is the tension to the terminals of the capacitance.

$$V_{signal} = \frac{B_{signal} * A * N}{Z * C}$$

The voltage noise density V generated by our tuned coil is

$$V_{noise} = \frac{L\omega\sqrt{4k_bRT}}{Z}$$

A relevant method to express the efficiency of a sensor is to calculate its equivalent field noise which is also called "detectivity". It corresponds to the magnetic field we should apply on the sensor to obtain a signal-to-noise ratio of 1 without any averaging. It can be calculated easily by normalizing the thermal noise voltage by a calibrated signal measured with the sensor. The detectivity of our tuned coil is

$$Detectivity = \frac{\sqrt{V_{noise}^2 + V_{preampli}^2}}{V_{signal}} * B_{signal}$$

Two simulations were performed. In the first one the circuit resonates at 300 kHz.

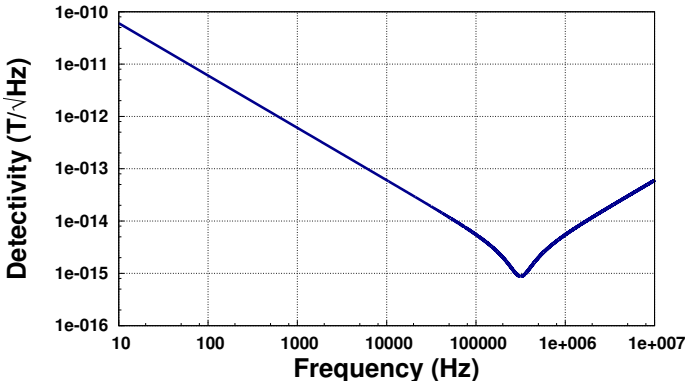

Figure 3.4: Tuned coil detectivity profile for a resonance at 300 kHz.

The detectivity improvement due to the resonance clearly appears here. We reach a 1 $fT/\sqrt{Hz}$ detectivity at 300 kHz. Then in a second simulation, the coil is tuned at different resonance frequencies (with a working bandwidth of 3 kHz) in order to plot its maximum sensitivty as a function of working frequency.

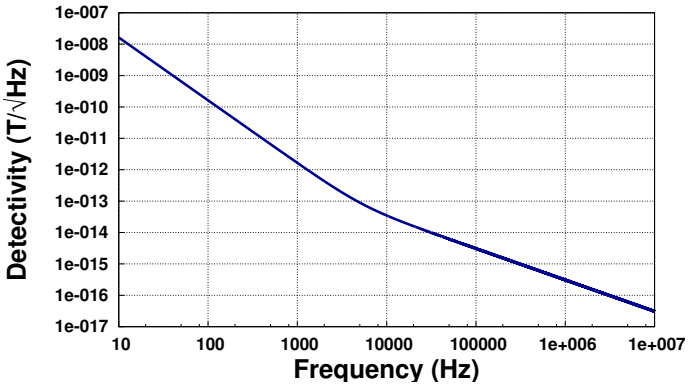

Figure 3.5: Tuned coil detectivity profile for a resonance between 10 Hz and 10 MHz.

As it is well known in Faraday detector, higher frequency comes with better sensitivity. This is the reason why tuned coils are really

popular at high field. The "break" in the curve around 10 kHz corresponds to the threshold under which the preamplifier noise becomes non negligible. According to the working bandwidth frequency at very low field, this preamplifier perfectly fits our requirements. An experimental measurement is then performed at 300 kHz with the same tuned coil. The signal is emitted by a large coil to obtain a precise calibration. The measured detectivity is 1.9 $fT/\sqrt{Hz}$ close from the simulation (1 $fT/\sqrt{Hz}$). The same coil is then modified to resonate at 70 kHz. The new detectivity is measured around 4.5 $fT/\sqrt{Hz}$ for a predicted value of 4.4 $fT/\sqrt{Hz}$.

3.1.3 *Pulses and noise*

Additionally to their good sensitivity, Faraday detectors are strongly coupled to other emitting coils. As we have seen before, an MRI setup is composed of several coils to generate required fields. One of them is strongly coupled to the tuned coil, the excitation coil. Pulses, generated by this untuned copper wind, are amplified by the tuned coil. This coupling comes down to concomitant excitation creation, especially on the edges.

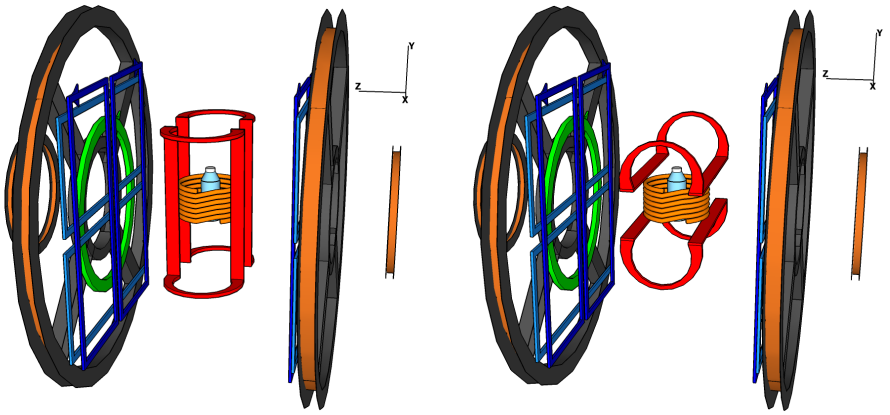

(a) (b)

Figure 3.6: Setup in a) perpendicular and b) parallel state

We put the excitation coil perpendicular to the reception coil to minimize the coupling (Figure 3.6). Then we measure pulses amplitude B_1 on X,Y and Z directions with a small coil ($\varnothing = 1$ cm).

	Untuned Coil	Tuned Coil
B_{1x}	60 mV	68 mV
B_{1y}	2 mV	12 mV
B_{1z}	2 mV	6 mV

Table 3.1: Effect of tuned coil on B_1 excitation pulse

We have a concomitant excitation of 15% along Y and 7 % along Z. As a result, it is difficult to perform an homogeneous $\frac{\pi}{2}$ pulse on large sample and some small intensity variations can appear. Moreover, such sensor with a high detectivity is sensitive to laboratory noises. We tried to measure the tuned coil noise floor in the MRI setup when all power supplies are successively OFF and ON. We also tried to orientate the excitation coil along the X and Y direction to see its impact on the tuned coil.

	Alimentation OFF	Alimentation ON
Noise with parallel pulse coil	6 $nV/\sqrt{Hz}$	8.1 $nV/\sqrt{Hz}$
Noise with perpendicular pulse coil	5.5 $nV/\sqrt{Hz}$	5.5 $nV/\sqrt{Hz}$

Table 3.2: Tuned coil sensitivity to external noise

It appears here that we should always work with an excitation perpendicular to the reception coil. Despite the fact we reduce the noise inside our receptor, we also protect it more efficiently against strong pulse that could damage it or blank the preamplifier.

3.1.4 *Nuclear Magnetic Resonance*

NMR measurements with this tuned coil at 300 kHz (7mT) have been performed to test its robustness in MRI conditions. A $\frac{\pi}{2}$ pulse excites a water bottle. Shims are set to reach a reasonable homogeneity around 20 Hz and the signal is averaged 100 times.

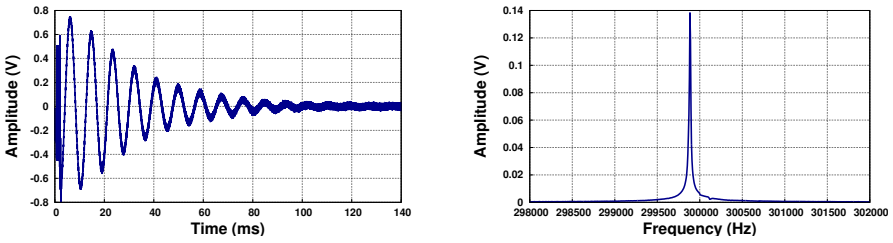

(a) (b)

Figure 3.7: Tuned Coil NMR a) Free Induction Decay and b) its Fast Fourier Transform

The resulting signal-to-noise ratio is calculated such as

$$SNR = \frac{Amplitude_{peak}}{Amplitude_{noise\ floor}}$$

It is around 876 for 20 seconds acquisition with 50 averagings. Our preamplifier is not saturated during pulses and the peak width correspond to the expected homogeneity. Advanced images are presented in Chapter 5 and compared with mixed sensor performance.

3.2 SQUIDS AND ATOMIC MAGNETOMETERS

Two alternatives to tuned coils are presented here. A small introduction to Superconducting Quantum Interference Devices and Atomic Optical Magnetometers is given. Capabilities and restrictions of both sensors are described. Their integration in MRI environments is also discussed. Finally, imaging examples obtained by other research team are presented.

3.2.1 *DC SQUIDs*

For magnetic measurements, other very sensitive devices can be used to compete with tuned coils, especially at low frequencies (under 400 kHz). Direct Current Superconducting QUantum Interference Device (DC SQUID) is one of the most promising alternative sensor [13]. It is made of a superconductive loop interrupted by two Josephson junctions diametrically opposed. It uses properties of those both elements to manage a precise measurement of a magnetic field applied on the element.

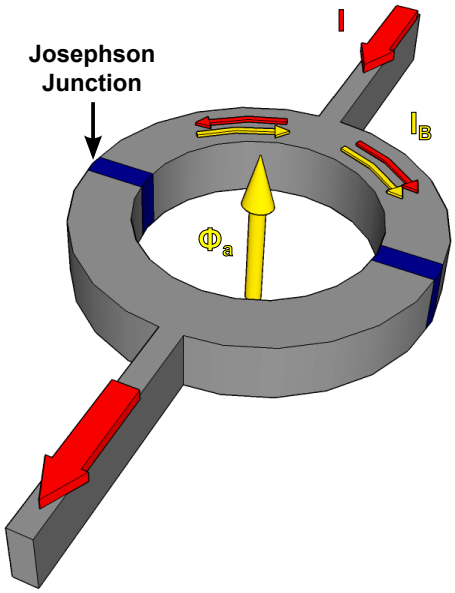

Figure 3.8: SQUID schematic : Because of an external field Φ_a, a super current is circulating in the loop (in yellow). At the same time, a current is applied on the superconducting loop (in red).

A Josephson junction can be described as a weak link between two superconductors. It can be constituted by a thin insulating barrier, a non superconducting metal or a physical constriction. The current passing through this Josephson junction can be described as

$$I_j = I_c sin(\delta) \tag{3.1}$$

where δ is the phase difference across the junction. When a field Φ_a is applied on a SQUID which is not alimented, both branch are crossed by the same circulating current I_B. This super current appears because of a special property linked to superconductivity called Meissner effect for which no magnetic field can exist inside a superconductive material. As a result, a current appears in the SQUID to screen Φ_a . The phase change around the ring can be described by

$$\alpha + \beta + 2\pi\frac{\Phi_a}{\Phi_0} = 2\pi n$$

where α and β are the phase change due to the Josephson Junctions and $\Phi_0 = \frac{h}{2e}$ is the flux quantum. In this configuration, both junctions are similar and introduce the same phase change

$$\alpha = \beta = \pi(n - \frac{\Phi_a}{\Phi_0})$$

If the SQUID is supplied with a current I, it is not the case anymore. One junction is crossed by $I_B + \frac{I}{2}$ and the other by $I_B - \frac{I}{2}$. The corresponding phase change are now

$$\begin{cases} \alpha = & \pi(n - \frac{\Phi_a}{\Phi_0}) - \delta \\ \beta = & \pi(n - \frac{\Phi_a}{\Phi_0}) + \delta \end{cases} \tag{3.2}$$

with δ depending on I. According to 3.1 and 3.2, we have

$$I = 2I_c cos[\pi(n - \frac{\Phi_a}{\Phi_0})]sin[\delta]$$

This equation shows that the critical current circulating in the SQUID depends periodically on the applied flux. With a judicious bias current, a change in flux could result in a change of voltage which is then easy to measure. Figure 3.9 shows the variation of the I-V curve of the SQUID depending on the applied flux. According to the bias current we inject, the voltage response will change.

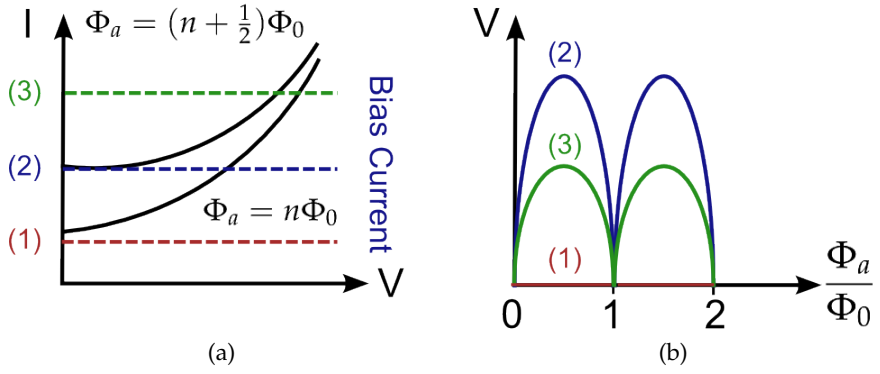

Figure 3.9: a) I-V Curve of a SQUID b) Voltage response according to the chosen bias current

The ideal bias current to use is slightly higher than the maximum junction critical current (Figure 3.9 - (2)). It should be precised that the I-V characteristic is usually hysteretic. This can be solved by shunting the junction with a resistance R.

Another important point is the periodicity of the voltage response to flux variation which limits the SQUID range. The use of a Flux Locked Loop [4] is used to overstep this dynamic range limitation. As for any sensors, a DC SQUID is subject to noise. First, the current supply introduces some noise that can be minimized with the use of judicious filter. Shunt resistances also come with Johnson noise. Finally, $\frac{1}{f}$ noise has been observed. It is coming from fluctuations in the Josephson junctions as well as motion of vortices trapped in the body of the SQUID. Moreover it is difficult to work with this sensor with a static field higher than several hundreds of microTesla which saturates the SQUID. Thus SQUIDs are usually limited to Ultra Low Field MRI with a prepolarization stage. In the white noise regime, at 77K, SQUIDs (2 cm x 2 cm) reach a detectivity of 10 $fT/\sqrt{Hz}$ [12].

3.2.2 *SQUIDs for MRI*

For MRI applications, SQUIDs are often used with flux transformer (superconductive, resistive or tuned) to increase the filling factor without increasing their inductance. For a superconductive one, the circuit is composed of two inductance in series, the pickup coil and the input coil respectively coupled to the sample and the SQUID.

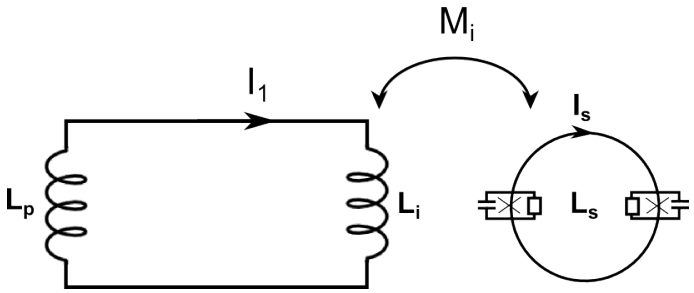

Figure 3.10: SQUID coupled with a superconductive flux transformer

For a flux Φ_{ext} applied on the pickup coil and a negligible current circulating in the SQUID, Faraday's Law gives us :

$$\begin{cases} \Phi_{ext} &= -(L_p + L_i)I_1 \\ \Phi_s &= M_i I + L_s I_s \end{cases}$$

with Φ_s the flux across the SQUID and $M_i = k\sqrt{L_i L_s}$. Because of Josephson junctions, we have $L_s I_s \ll M_i I$. Then the gain in flux from the pickup loop to the SQUID becomes :

$$G = \frac{\Phi_s}{\Phi_{ext}} = \frac{M_i}{L_p + L_i}$$

An optimized flux transformer respects $L_p = L_i$. Then we have

$$G = \frac{k}{2}\sqrt{\frac{L_s}{L_p}}$$

To maximize the gain, a strong coupling is required (k = 0.8 to 0.9 for input coils deposited on top of SQUID washer [28]) as well as a low inductance for the pickup coil (only 1 turn in most cases). A low T_c SQUIDs coupled to a niobium flux transformer with a pickup coil area of 1 cm^2 achieves 1 $fT/\sqrt{Hz}$ field noise[13]. The flux transformer can also be resistive and behave like a RL filter. In this case, we have to work at high frequency to reach the same gain than a niobium flux transformer. It can also be tuned by adding a capacitance. In this case, the flux transformer becomes a Faraday detector and the SQUID acts like a low noise preamplifier. Both cases will be discussed later with Mixed Sensors.

In MRI experiments, lots of external noise can be generated by the environment (magnetic field supplies, 50 Hz,...). On way of reducing this external contribution is to use gradiometers pickup coil. For a first order gradiometer, the pickup coil is separated in two identical coils wound in opposite directions and separated by a baseline. This way, depending on the coils orientation, the gradiometer cancels all homogeneous contribution to magnetic field along 1 direction. The sample contribution is saved because of its proximity to one of the loop.

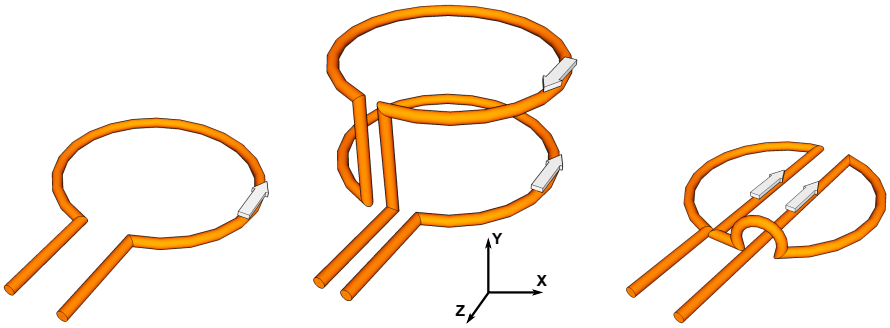

(a) (b) (c)

Figure 3.11: a) Classic pickup coil b) Gradiometer along Y direction c) Gradiometer along X direction

However this solution is not perfect as it is reducing significantly the filling factor. Therefore it becomes interesting only if the working environment presents strong homogeneous noise components. With limited RF shielding, Seton and Al. [52] observed an important gain in Signal to Noise Ratio using those gradiometers instead of a classic 1 turn pickup coil.

With the use of a prepolarization field of 40 mT, John Clark et al.[13] presented in vivo measurement of a human forearm using SQUIDs at 132 μT.

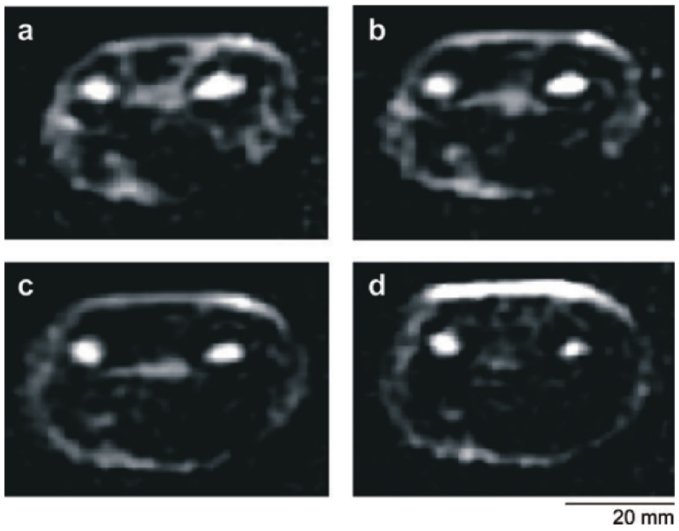

Figure 3.12: Slices (a-d) of 20 mm thickness with an in-plane resolution of 2 mm x 2 mm

The prepolarization step is necessary at this field to obtain enough NMR signal. Its use imposes a polarization time in sequences (limiting the possibilities) and a particular attention to Eddy currents that can be generated in the shielding room.

3.2.3 *Atomic Optical Magnometers*

Atomic Optical Magnetometers are highly sensitive sensors which have been extensively developed since 2000. Their implantation in magnetic measurement experiments are higher and higher as they present a very good detectivity and requires no cryogenic cooling.

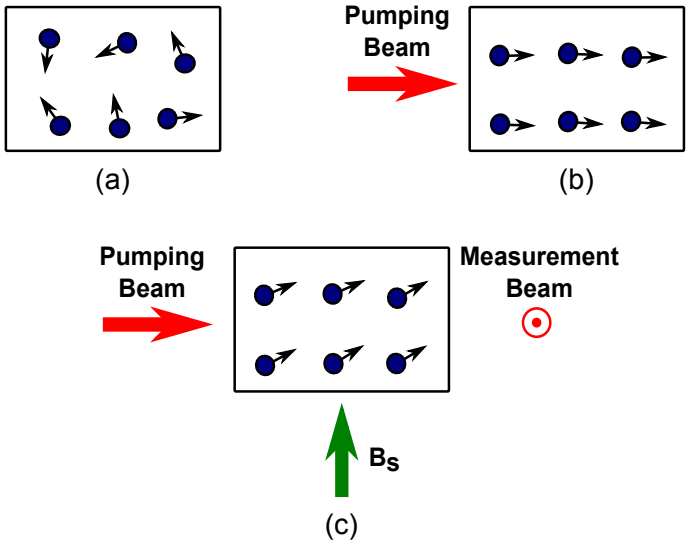

Figure 3.13: Atomic Magnetometer Principle : a) Randomly oriented magnetic moments b) are oriented along the pump beam direction and c) precess because of the applied magnetic field. This precession is being measured with another orthogonal beam.

The general idea is to measure interactions between a magnetic field and electronic spins of an atomic vapor inside a glass cell. Due to their unpaired electron, alkali atoms (Potassium, Cesium, Rubidium) present an intrinsic magnetic moment. In a gas, those magnetic moment are randomly oriented and no magnetic moment appears on a macroscopic level. An optical pumping near the resonance of the appropriate electronic transition create a spin polarization along the pump beam direction. According to the applied field, this macroscopic magnetic moment will precess at a frequency v. Then a linearly polarized light shining through the gas is sent. Its absorptive and dispersive properties will change according to the precession and thus to the applied field. Limited by the shot noise, those devices achieve $1\ fT/\sqrt{Hz}$ for a cell volume of $500\ cm^3$ [9].

A huge improvement in detectivity has been achieved with the spin exchange relaxation-free (SERF) regime. At low magnetic field, atom-atom spin exchange collisions in the gas cell are no longer a source of decoherence and the alkali atom density can be dramatically increased and improve the detectivity. A detectivity of $1\ fT/\sqrt{Hz}$ kHz for a $1\ cm^3$ cell can be achieved with such sensor. The theoretical limit of magnetic field detectivity is below $0.01\ fT/\sqrt{Hz}$ for a cell of $1\ cm^3$ [31]. However both methods are relevant only for quasi-static magnetic fields ($\lesssim 20Hz$). For very low field MRI applications, an alternative method based on same optical properties is used.

An atomic optical magnetometer can also operate as a resonant receiver of radio-frequency.

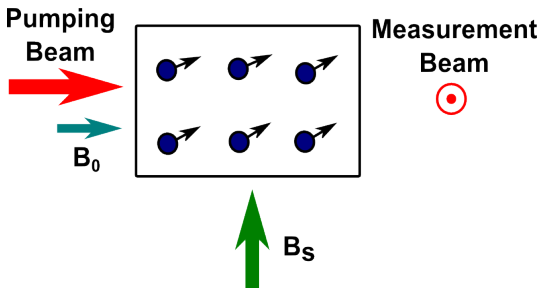

Figure 3.14: Tuned RF Magnetometer

The alkali metal vapor is optically pumped. We apply a static magnetic field B_0 such as the ground state Zeeman splitting of the alkali atoms is tuned at the signal frequency. Then any transverse signal B_s at this frequency will induce a transverse polarization of the atomic spin :

$$P_x = \frac{1}{2}\gamma B_s T_2$$

where T_2 is the transverse relaxation time of the polarization and γ the gyromagnetic ratio. This polarization is measured again with a linearly polarized laser beam passing through the cell. Detectivity of 0.24 $fT/\sqrt{Hz}$ at 400 kHz is achieved with a 100 cm^3glass cell [32].

Combining multiple beams and photo-detector arrays, those devices could be easily used for multichannel measurements.

3.2.4 *Atomic Optical Magnetometers for MRI*

For MRI application, this technique requires a specific setup which implies some new limits. First the Larmor frequency of protons (4.26 kHz/G) is quite different from the bias field required to make the cell resonate (700 kHz/G). This implies that we need to apply two different fields. Atomic optical magnetometer does not require homogeneity like NMR (100 ppm for NMR and 1% for Atomic optical magnetometer). And we also need to apply important gradients exclusively on NMR sample. If the gradient is also applied to the cell, this would broaden the atomic magnetometer line-width and reduce its detectivity. Consequently flux transformer is necessary to decouple fields and gradients.

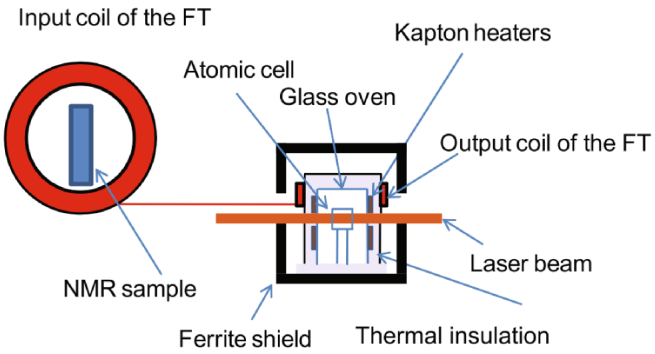

Figure 3.15: Entire setup for MRI applications

This flux transformer introduces a thermal noise which becomes the limit of detectivity of the system. Actually a 1 $fT/\sqrt{Hz}$ system has been realized for practical MRI images [51].

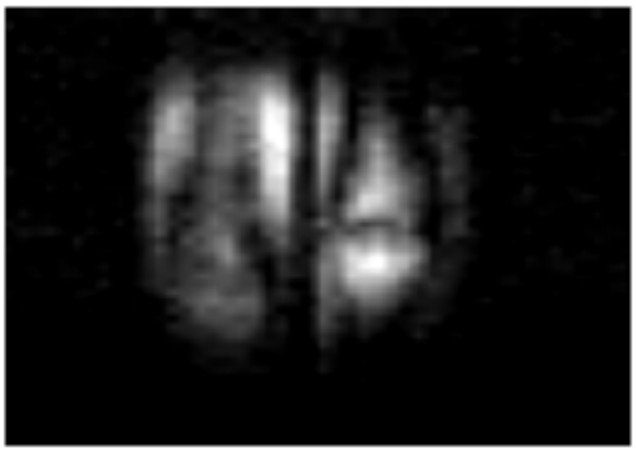

Figure 3.16: Slice (4.4 mm)of fingers with a 1.1 mm x 1.4 mm resolution

This in-vivo image has been acquired in 12 min 30 [50] at 85 kHz with one Atomic Optical Magnetometer channel. To achieve a good detectivity, the atomic optical magnetometer requires very low external magnetic field perturbations. The use of a ferrite shield is very important here as it is protecting the sensor from external fields by a factor 100.

3.3 MIXED SENSORS : THEORY

In this thesis, a new kind of sensor called Mixed Sensor has been used to perform MRI images. Here is a quick review of this sensor and its characteristics. The principle of Giant MagnetoResistance is presented as well as its coupling to a superconducting flux-to-field transformer. The noise sources of such a device are described and its equivalent noise field is then deduced.

3.3.1 *Giant MagnetoResistive Sensor*

At the end of the 80s, the giant magnetoresistance effect has been discovered in layered material composed of two or more coupled ferromagnetic layers separated by non magnetic spacers [7]. They presented a large change in resistance when a relatively large magnetic field was applied. This magnetoresistance effect arises as the result of the spin-dependent conductance in the ferromagnetic layers, and/or as a result of spin-dependent scattering at the interfaces. Based on this effect, a three layer structure called Spin Valve has been developed by IBM for hard-disks read heads applications. This sandwich stack of two ferromagnetic layers around one non magnetic spacer presents conductance changes with small field variation. Because of its microscopic size and the amplitude of its GMR effect, it is used in mixed sensor. To understand this change in resistance, the current is represented as two conduction channels in a classic Spin Valve stack(Figure 3.17).

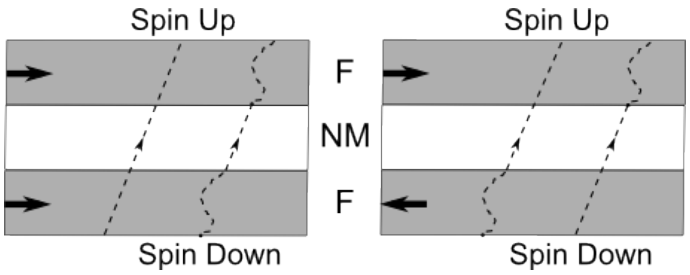

Figure 3.17: Electronic transport of 2 conduction channels in a Spin Valve composed of two ferromagnetic layers (F) around one non magnetic spacer (NM).

The spins up channel has different conduction properties than the spins down channel in magnetic material according to the magnetization direction. In a Spin Valve, a parallel alignment will diffuse only one channel which results in a low resistance. At contrary, an antiparallel alignment will diffuse both channel which gives a high resistance. (Figure 3.18)

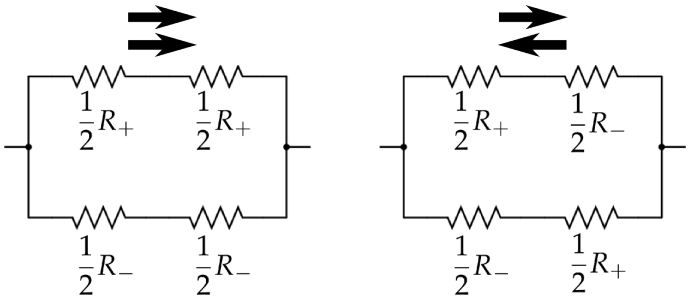

Figure 3.18: Resistor scheme of a Spin Valve

To link this conductance change with an external field variation, one of the layer should be sensitive to this external field. This is why a Spin Valve stack is always composed of one hard layer and one soft layer decoupled by a nonmagnetic spacer. Depending on the hard layer position, either at the bottom or at the top, the spin valve is respectively said to be bottom-pinned or top-pinned.

Each layer of the Spin Valve stack is composed of several sublayer that have been optimized for Mixed Sensor applications ([21]) :

- The Hard Layer needs to have a constant magnetization direction which requires a high coercive field. Moreover it needs to polarize efficiently conduction electrons. This polarization is directly linked to the amplitude of the GMR effect. To fix the magnetization, anti-ferromagnetic materials are good candidates. They have a fixed orientation which doesn't depend on any external magnetic fields. Then such material (FeMn, IrMn, PtMn) are coupled with a ferromagnetic material (CoFe) which is a powerful spin polarizer. Thus we obtain a hard layer. The magnetization can be stabilized by a more complex anti-ferromagnetic coupling between two CoFe layers separated by a Ru layer. This structure provides a null net moment.

- The spacer is made of Cu material. Its thickness (around 3 nm) has to be under the spin diffusion length for an optimum GMR effect.

- The soft layer is composed of two ferromagnetic layers. A soft magnetic material (NiFe) is coupled to a high spin polarizer material (CoFe). Thanks to the coupling between those two layers, we obtain a stack with a low coercive field while polarizing electron spins to increase the GMR effect.

The whole stack is sandwiched by two layers of tantalium (Ta) to adapt the device easily to substrate, isolator and contacts, depending on the use. It also protects the stack from oxidation.

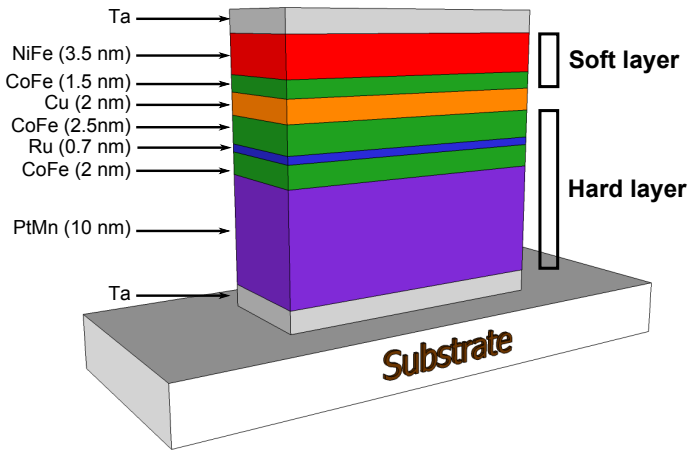

Figure 3.19: GMR stack example

For sensors applications, magnetic layers must have crossed anisotropies ($\theta = 90°$). When a field is applied, the hard layer with a high coercive field keeps its direction but the free layer with a low coercive field tends to align with $\vec{B}$. The resistance variation depends on the angle formed by the two magnetization directions and can be expressed as [14]:

$$R(\theta) = R(\theta = 0) + \frac{\Delta_{GMR}}{2}(1 - cos\theta)$$

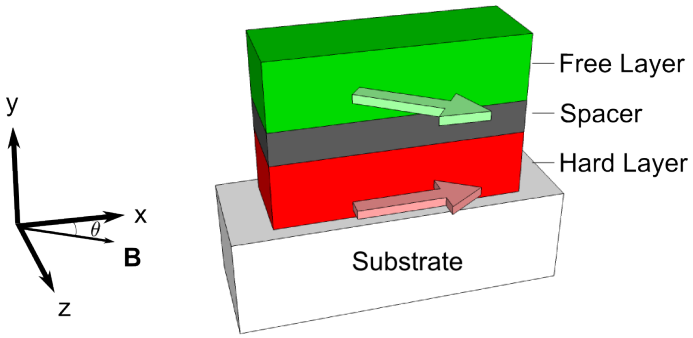

Figure 3.20: Spin Valve in a Field

The last issue is related to the geometry of the stack. Because of mixed sensors requirements, the spin valve element must be around 5 μm width and 200 μm length. On microscopic sized magnetic layers, magnetic domains appears. Those are responsible of an hysteretic behavior of the GMR and the apparition at low frequency of a random telegraphic noise. A yoke shape has been designed to avoid those magnetic domains in a specific working zone. A simulation of the distribution of magnetic moments in a soft layer (Figure 3.21 - [46]) shows the magnetic vortex pushed to the extremities while a single domain is formed in the main bar (the working zone).

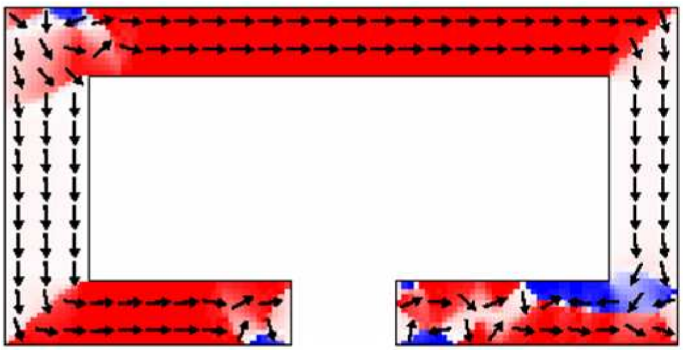

Figure 3.21: Magnetic configuration of a NiFe yoke. Small arrows indicate the direction of domain magnetic moments

The magnetization of this single domain lies along the direction of the yoke because of the shape anisotropy. To obtain a cross anisotropy at zero field, the hard layer has to be perpendicular to the yoke. This yoke is then coupled to a flux to field transformer.

3.3.2 *Superconducting Flux-To-Field Transformer*

The GMR yoke has a rather good sensitivity (dozen of $pT/\sqrt{Hz}$) for its size but it is still far from SQUIDs performance. One solution to enhance its sensitivity is to find a way to increase the field seen by the stack by integrating it over a larger surface. First solution to do that was to use a field concentrator made of soft magnetic material [23]. The sensitivity obtained (around 1 $pT/\sqrt{Hz}$) are still poor. Another solution is to use a superconducting current loop. This is the solution used for mixed sensors.

Below its critical temperature T_C, a superconductive material becomes non resistive because of the electrons that form Cooper pairs. This loss-less conduction comes with another phenomenon called Meissner Effect. As we have seen before for SQUIDs, it states that no magnetic field can exist in a superconducting material. When a magnetic field is applied on a superconductive loop, the result is the creation of a screening current I_s that cancels the applied field. The flux Φ_a applied and the flux Φ inside the loop respect :

$$\Phi = \Phi_a + L_{ms} I_{ms} = 0$$

where L_{ms} is the inductance of the superconductive loop and I_{ms} the screening current circulating. Now if the loop width is reduced at some point, the current density will be much higher in this constriction than on the rest of the loop. Thus the magnetic field B_s close to the constriction will be strongly enhanced with respect to B_a. Then if the GMR Yoke is placed upon this superconductive constriction, we

obtain a sensor much more sensitive than the classic Spin Valve alone. The gain of the superconductive loop is :

$$G = \frac{B_s}{B_a}$$

Depending on the loop geometry and its material composition, we usually reaches gain between 400 and 2000.

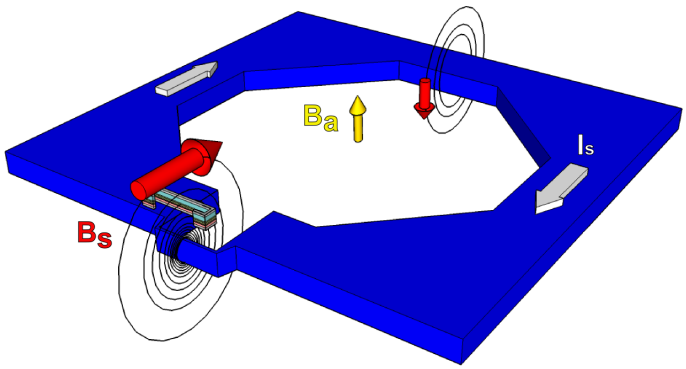

Figure 3.22: Mixed sensor schematic : An external field B_a generates a current I_s in the superconducting loop. On the constriction, the field seen by the GMR yoke becomes B_S.

Two superconductive materials are mainly use for mixed sensors loop :

Niobium is a low temperature superconductor. It's a superconductive material of type 2 which implies a state where super-current flow but a flux can enter into the material. Its T_C is around 9K, far above Helium liquid temperature (4K). Moreover it is a metal rather easy to grow on thin films.

YBaCuO is a high temperature superconductor. This ceramic behaves like a type 2 superconductor too. It's critical temperature is around 90 K, far above Nitrogen operating temperature(77K).

3.3.3 *Superconductive loop Inductance*

The superconductive loop gain can be predicted if we have a precise measurement of its surface and its inductance. The surface measurement is straightforward. However the inductance measurement is difficult and a simulation software is usually used to determine an approximate value. A new method of coupling measurement (Chapter 4.3) allows us to experimentally measure that inductance. An input coil is coupled to the mixed sensor.

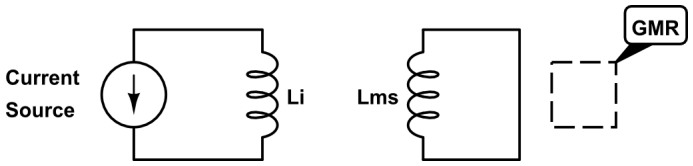

Figure 3.23: Electric circuit of an input coil coupled to the superconducting loop of a mixed sensor.

If we send a current into the input coil, we obtain

$$L_2 I_2 + M I_1 = 0$$

The response of our mixed sensor is corresponding to a flux (knowing the sensitivity) applied on it and this flux correspond to $L_2 I_2$. Finally

$$k\sqrt{L_1 L_2} = -\frac{\phi}{I_1}$$

Then,

$$L_2 = \frac{\phi^2}{L_1 k^2 I_1^2}$$

With a precise measure of k (see Chapter 4.3), we can experimentally access to L_2. We tried to compare simulations to this experimental value on a YBaCuO loop of 1x1 cm^2 . The simulation gave an inductance of 20 nH and we measured an experimental value of 18.6 nH .

3.3.4 *Noise sources*

The noise in a mixed sensor is mainly due to the GMR device. The superconductive loop does not introduce any intrinsic noise.

First this component has an intrinsic resistance which implies an electric noise due to thermally motion of charge carriers. This noise is equivalent to a fluctuating voltage source V_{th}. On a 1 Hz bandwidth, we can write :

$$V_{th} = \sqrt{4 k_b R T}$$

where R is the intrinsic resistance of the GMR, T its temperature and k_b the Boltzmann constant. This noise is the fundamental limit of sensitivity of our sensor at any frequency. To convert this voltage noise into a field noise, we have to determine the response V_B of our sensor. Then,

$$B_{th} = \frac{V_{th}}{V_B}$$

This is the best sensitivity that can be achieved with the sensor. For example, with a typical Spin Valve sensor with a GMR effect $\rho_{GMR} = 2\%/mT$, a resistance R = 1 $k\Omega$, a working temperature of 77K and a sensing current of 10 mA, we have :

$$V_{th} \approx 2\, nV$$

$$V_B = 0.2\,V/mT$$

Finally, the sensitivity of this Spin Valve alone is around 10 $pT/\sqrt{Hz}$. Now if we consider a loop of 1 cm^2 with a gain of 450, this leads to a sensor of 23 $fT/\sqrt{Hz}$. This is true only if the thermal noise is the only source of noise. However, for small GMR devices, at low frequency, a noise caused by fluctuation of conductance due to charge traps by defect exists. It is called $1/f$ noise. The mean power spectral density of this noise can be expressed phenomenologically as [26]:

$$P_{1/f} = \frac{\alpha_H V^2}{Nf}$$

where V is the potential difference across the conductor, N the number of charge carriers (depends on the volume), f the frequency and α_H is an empirical parameter called the Hooge constant. For large size giant magnetoresistance device, the volume is important enough to neglect the 1/f noise at very low field frequencies. However in the yoke, this 1/f noise can be important even for MRI application above 42 kHz (1 mT). It depends mainly of the mixed sensor fabrication. In the best case, a Spin Valve Sensor presents a 1/f noise corner (frequency under which 1/f noise become predominant) around 100 Hz for a bias current of 1 mA. In those cases, for MRI application, we always work in the thermal noise limited regime.

A simple way to determine the working regime consists in applying different bias current to a mixed sensor. If we are in thermal regime, sensitivity increases linearly with the current. If it is not, it means that the device is dominated by the 1/f noise of the spin valve or it could also mean that the laboratory noise is more important than the giant magnetoresistance noise. To distinguish between them, we increase the current across the giant magnetoresistance until the constriction of the superconductive loop warms up. A drop in noise would be a clear signature of external noise contribution.

CONCLUSION

For high field MRI, tuned coils are an indisputable reference. However, their equivalent field noise decreases linearly with the magnetic field. The detectivity measured at low frequencies (1 $fT/\sqrt{Hz}$ at 300 kHz) opens the way towards new detection methods. Combined with a flux transformer, SQUIDs present a good detectivity (around 1 $fT/\sqrt{Hz}$ at 6kHz). They are especially adapted for ultra low field MRI as their are very sensitive to static fields above several hundred of microTesla. Atomic Optical Magnetometers presents also a good detectivity (1 $fT/\sqrt{Hz}$ at 85 kHz) with the use of a tuned flux transformer. This sensor needs to be totally shielded from any external static field. In this thesis, another kind of sensor is used. Based on the combination of a giant magnetoresistance and a superconducting

loop, it could offer interesting detection performance and does not present any intrinsic incompatibility with external static field. Experimental detectivity measurements and optimal configurations will be discussed in the next Chapter.

4

MIXED SENSORS FOR VERY LOW FIELD MRI

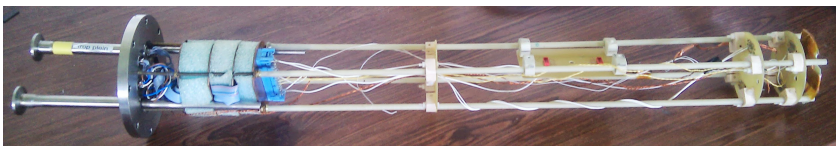

Cryogenic stick for mixed sensor testing

Mixed sensors are complex devices that need to be precisely characterized. A complete description of the experimental protocol used to measure their detectivity is presented here. Like for SQUIDs and Atomic Magnetometer, mixed sensors could benefit from the use of a flux transformer. However a low field flux transformer needs to fulfill specific constrains depending on precise parameters. Choices and measurements of those parameters are going to be discussed through experimental measurements and simulations.

4.1 CHARACTERIZATION OF MIXED SENSORS

Previously, the physic principle of a mixed sensor was developed. The experimental procedure to characterize it is discussed here. Optimized giant magnetoresistance configurations are also detailed through the use of specific electronic bridge. Finally, the integration of YBaCuO mixed sensors into the small MRI setup is described with the use of an adapted preamplifier. Their detectivity and behavior in this particular environment are measured for two fabrication processes.

4.1.1 *GMR Characterization*

To characterize a mixed sensor, the first thing is to determine the giant magnetoresistance effect of the corresponding stack. A layout of resistive coils generates a magnetic field B_{SCAN} which is applied perpendicularly to the yoke.

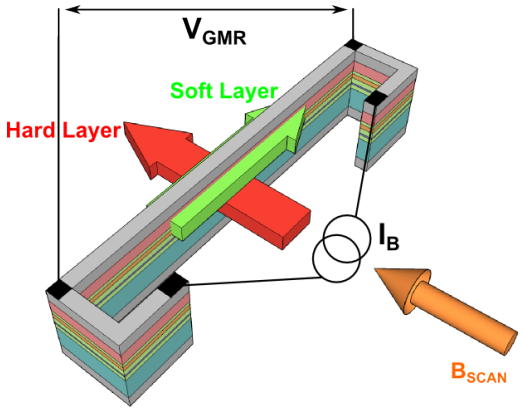

Figure 4.1: Giant magnetoresistance Characterization

A four-terminal sensing measurement is performed to obtain the resistance of the device. This method suppresses the contribution of contacts and wires resistance . A scanning magnetic field is applied to reach both states of the transfer curve, parallel and anti parallel. In this way we obtain the Magneto-Resistance transfer curve. The Magneto-Resistance ratio is deduced as :

$$MR_{ratio} = \frac{R_{par} - R_{anti}}{R_{par}} * 100$$

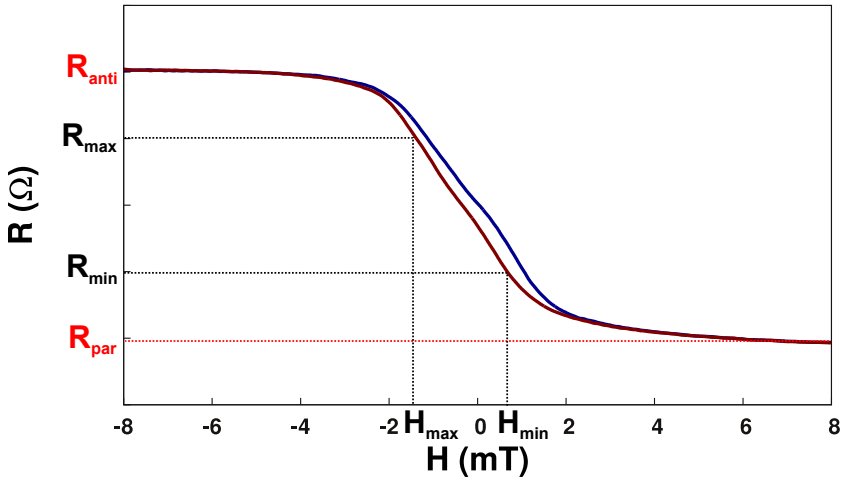

Figure 4.2: Giant magnetoresistance cycle

The sensitivity ρ_{GMR} of the yoke is here defined as the resistance change (%) per unit field (mT) at zero field. In the linear response region, this can be expressed as

$$\rho_{GMR} = \frac{1}{R_{min}} * \frac{R_{max} - R_{min}}{H_{max} - H_{min}} * 100 = \%/mT$$

This value is related to the MR ratio but it remains the most meaningful parameter for sensor applications. It has to be optimized in order to obtain the best device performances. However other factors should be taken into account :

- First the curve should be centered around $B_{SCAN} = 0$. Any shift is the result of a residual interaction between the hard layer and the soft layer and is thus related to the fabrication of the spin valve. This will lead to a degradation of the effective detectivity of our giant magnetoresistance sensor. A solution to correct this shift is to put a small magnet close from the giant magnetoresistance element. This will influence the orientation of the soft layer and result in a modification of the magnetoresistance response by shifting and flattening the curve. Thus, this will lead anyway to a small degradation of our detectivity.
- Secondly, a residual hysteresis due to inhomogeneous magnetic domains could be observed. This hysteresis often comes with a high low frequency random telegraphic noise and a non linearity of the curve. Again the use of a small magnet can stabilize disordered magnetic domains and then reduce hysteretic behaviors.

4.1.2 *Bridge Configuration*

A single giant magnetoresistance configuration is convenient for MRI measurements but not optimal. It has a strong DC component which

needs to be filtered to protect the preamplifier and its resistance fluctuates, which requires the use of a low noise current source. The use of a Wheatstons Bridge can be an adapted solution. This classical circuit configuration is usually used to measure unknown resistance. However, the use of 3 resistances at room temperature to complete the bridge would bring a huge thermal noise input. It would dominate all other noise sources and therefore reduce our detectivity. The commodious solution is to use a "Giant Magnetoresistance Bridge".

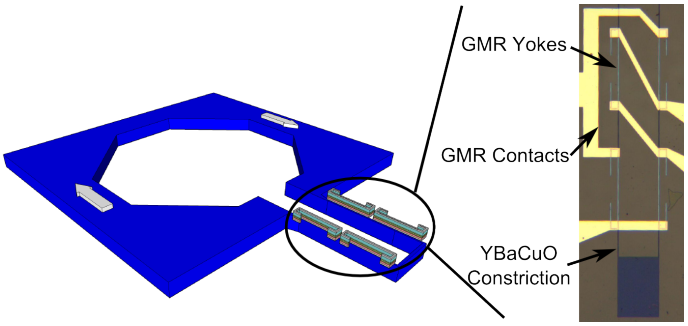

Figure 4.3: Giant magnetoresistance Bridge

In this configuration, one giant magnetoresistance's arm will have a resistance changing of $R + \delta R$ and the other arm will have a change of $R - \delta R$. According to the contacts of Figure 4.3, we obtain a full Wheatstone Bridge (see Figure 4.4).

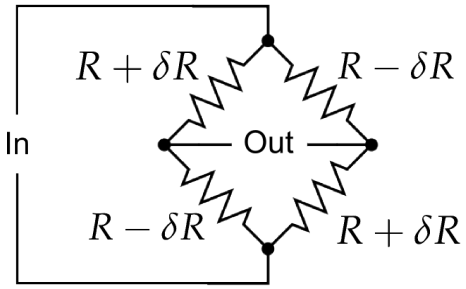

Figure 4.4: Antiparallel Bridge

In this configuration, any changing field will result in a symmetric change in resistance in both arms. The total resistance remains independently from the external field. This is a important point because it allows the use of a low noise voltage source as a battery which is much easier to implement than current source. Also, the output differential voltage is

$$V_{out} = \frac{V_{in}}{R}\delta R$$

This is twice larger than a single giant magnetoresistance fed with the same current. However, the Johnson noise generated by the bridge is equivalent to the one of a resistance R. The signal-to-noise ratio

is then twice that of an equivalent mixed sensor with only one giant magnetoresistance. We can notice that the differential voltage obtained is balanced to zero. This is not a relevant advantage for MRI applications but this is an important point for DC and low frequency measurements (magnetoencephalography applications). Finally, all four giant magnetoresistances are in the same environment and on the same substrate. Any changes in resistance temperature will be compensated avoiding any voltage drift.

4.1.3 *Mixed sensor Characterization*

The characterization of a mixed sensor in "full bridge" configuration is close to the giant magnetoresistances characterization. This time the use of a cryogenic environment is necessary for the superconductive loop.

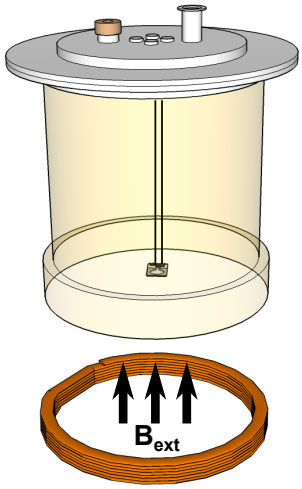

Figure 4.5: Characterization setup for a mixed sensor. An external coil is generating a calibrated signal B_{ext} on a mixed sensor in its cryogenic environment.

The applied field is now perpendicular to the loop plan. The amplitude required to obtain a full cycle is much lower than for the yoke alone. We scan the field until the critical current is reached, in both directions. The sensitivity is again linked to the slope of the curve.

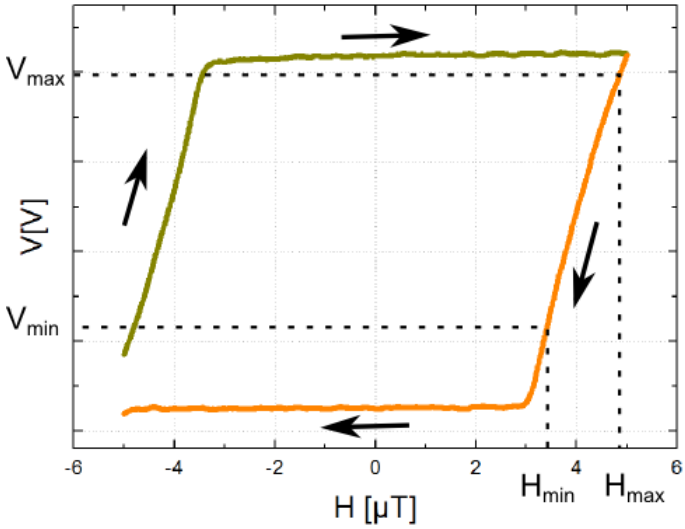

Figure 4.6: Mixed sensor cycle

This curve presents two zones :

- First we have two linear slopes which are the working zone. This is when the field is weak enough to be fully screened by the super-current.
- Secondly the flat zones corresponding to the saturation mode. This is when the critical current is reached and any further increase in the magnetic field can not be compensated. It should be noticed that this critical current is defined by the weakest part of the superconductive loop. In our case this corresponds to the constriction.

Once the saturation regime is achieved, the system enters in a mixed state in which vortices can penetrate the loop. This causes an hysteresis in the mixed sensor transfer curve. The sensitivity can be expressed :

$$\rho_{ms} = \frac{1}{V_{alim}} \frac{V_{max} - V_{min}}{H_{max} - H_{min}} * 100 = \%/\mu T$$

where V_{alim} is the voltage applied on the full bridge. It is possible to deduce the gain of the superconductive loop with

$$G = \frac{\rho_{ms}}{\rho_{GMR}}$$

To access the detectivity of our sensor, we need to convert its voltage thermal noise (if we are working in the thermal regime) into the corresponding field noise, knowing its sensitivity. This leads to

$$D = \frac{V_{Noise}}{\rho_{ms} * V_{alim}}$$

It should be noticed that the detectivity has been measured at low frequency, escaping the filtering of the cryogenic dewar super-isolation,

but the noise is considered in the thermal regime (above 40 kHz). It is the "intrinsic" detectivity of the mixed sensor. A measurement at 40 kHz would give a detectivity weighted by the dewar filtering.

4.1.4 *Preamplifier*

The output of the giant magnetoresistance bridge is connected to a differential low noise preamplifier. Its characteristics are resumed in Table 4.1.

PreAmplifier SA 421-F5 (NF Corp)				
Input Impedance	Output Impedance	Voltage Gain	Input Voltage noise at 100kHz	Input Current Noise at 100Hz
1 $M\Omega$	50 Ω	46 dB	0.5 $nV/\sqrt{Hz}$	100 $fA/\sqrt{Hz}$

Table 4.1: PreAmplifier Characteristics

The behavior of this preamplifier depends on the working frequency. It is described in Figure 4.7 (NF corp data).

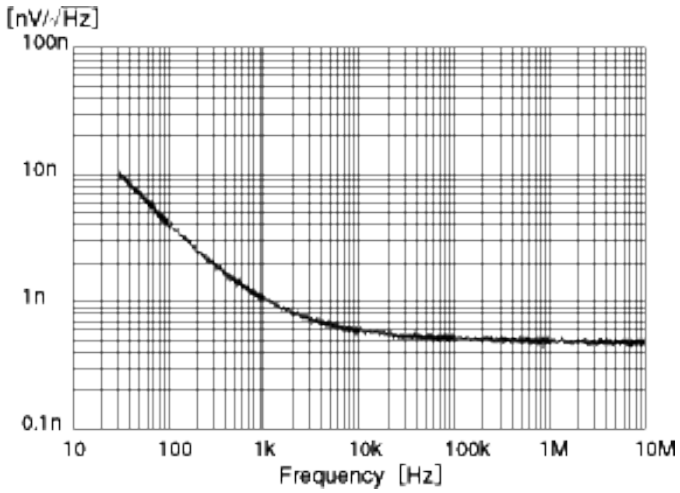

Figure 4.7: Preamplifier SA 421-F5 input voltage noise depending on frequency

The total noise of this system (Mixed sensor + Preamplifier) is

$$S_{V,Tot} = 4k_b R_{ms} T_{ms} + S_{V,a} + R_{ms}^2 S_{I,a}$$

where R_{ms} and T_{ms} are respectively the mixed sensor resistance and temperature. $S_{V,a}$ and $S_{I,a}$ are the power spectral density of the volt-

age and current noise. An interesting value to estimate is the ratio between the sensor and preamplifier's noise.

$$A_{ratio} = \frac{S_{V,a} + R_{ms}^2 S_{I,a}}{4k_b R_{ms} T_{ms}}$$

When A_{ratio} is bigger than 1 it means that our preamplifier is dominating the total noise which is a bad amplification situation. We plot this ratio at 77K and 4K.

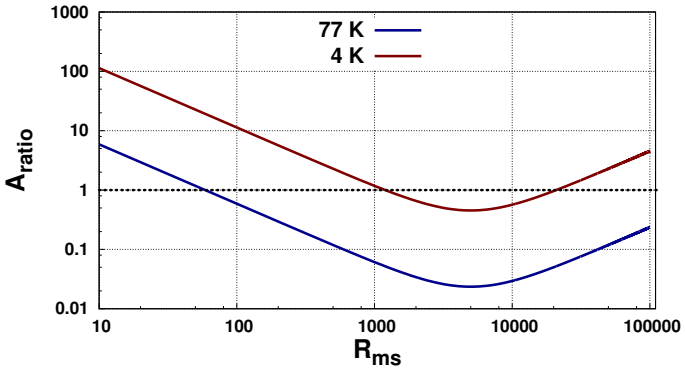

Figure 4.8: Ratio Noise

At 77K, the preamplifier will not be the main limitation but we should take care at 4K where its contribution can become important if giant magnetoresistance are beyond 1500 Ω. In such situation, a cryogenic preamplifier could be tested to achieve even lower noise.

4.1.5 *Detectivity*

Different kinds of YBaCuO mixed sensors have been tested for MRI applications. The first type have been processed by a private company Sensitec. They all have a superconducting loop of 1 cm^2 . A typical noise profile is performed from 1 Hz to 4 kHz with a voltage supply of 10 V in liquid nitrogen. This voltage corresponds to the ideal working voltage at 300 kHz (the 1/f noise is not dominant).

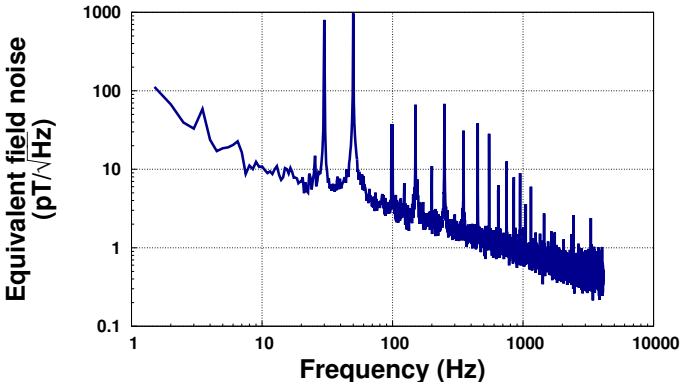

Figure 4.9: Noise profile of a typical Sensitec sensor of $1cm^2$ (KC005-F09)

An important $1/f$ noise is observed for this type of sensors. The reason is not clearly defined. At 300 kHz, this sensor (KC005-F9) has a detectivity of 120 $fT/\sqrt{Hz}$. Another type of YBaCuO sensors is tested in same conditions. Those sensors are homemade. Their superconducting loop lateral size were varying from 0.7 cm to 2.3 cm.

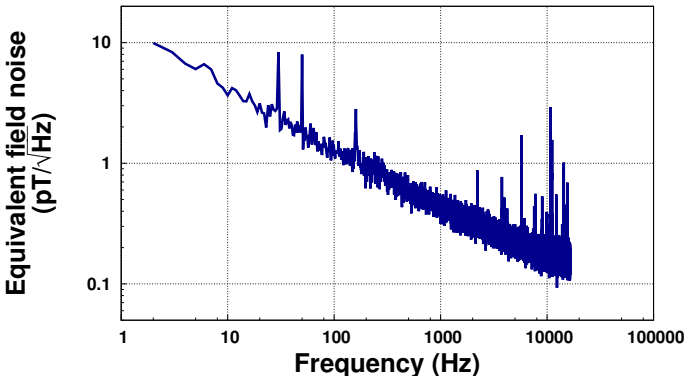

Figure 4.10: Noise profile of a typical homemade YBaCuO sensor of 1 cm^2

The $1/f$ noise is lower than Sensitec sensors due to a better giant magnetoresistance quality. At 300 kHz, this sensor has a detectivity of 30 $fT/\sqrt{Hz}$. The size of the loop is linearly increasing its gain and then the sensitivity of the sensor. Different sensors size have been compared in sensitivity.

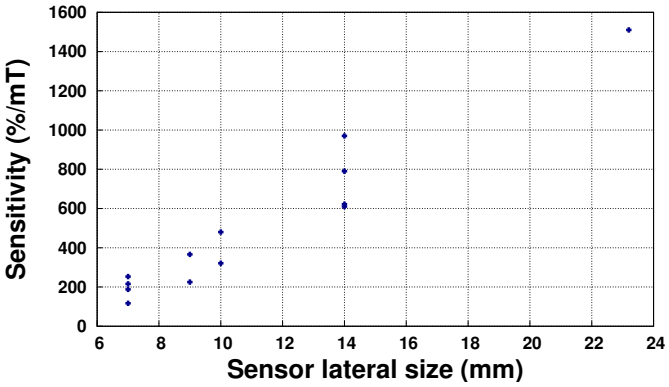

Figure 4.11: Sensitivity of homemade mixed sensors as a function of their lateral size

The relation between the sensitivity and the lateral size is linear and the small differences that can be noticed are the result of magnetoresistance effect changing between sensors. In this configuration, we should then use large sensors. However we will see that this statement is not true when we use a flux transformer. Those homemade sensors were not used for MRI measurements in my thesis because of a low robustness of the YBaCuO loop. After several utilizations, the gain of the loop was deteriorating. I've chosen to work with more stable sensors with a lower detectivity.

4.1.6 *Very Low Field MRI applications*

A detectivity measurement is performed inside the MRI setup, in same conditions to evaluate the environmental influence on the mixed sensor behavior. All permanent and excitation fields are set ON and sensor detectivity is monitored according to the rotation θ of the cryogenic dewar.

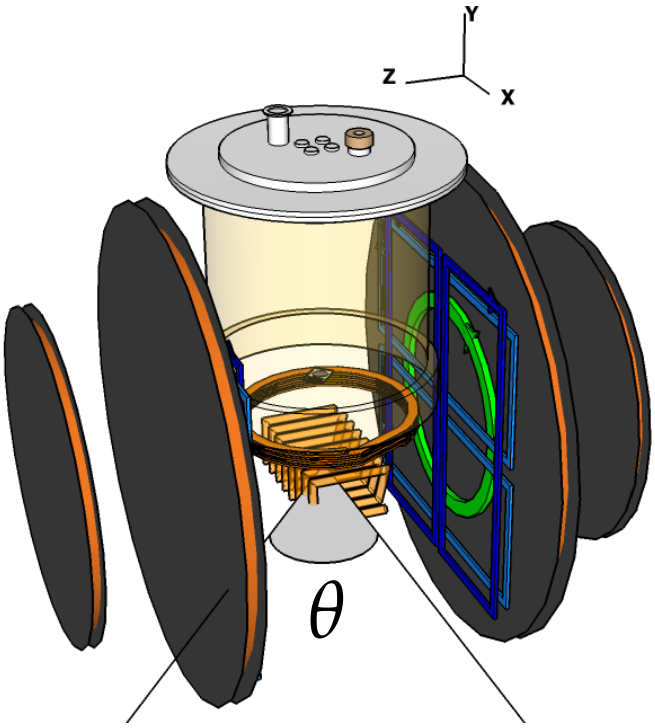

Figure 4.12: Sensitivity measurement in MRI conditions

The angle is not measured with high precision. The reference ($\theta = 0°$) is arbitrary chosen as the best position for the sensitivity. A current source is connected to a calibrated coil and a signal is sent at 300 kHz which is equivalent to a 7mT NMR signal frequency.

	$\theta = 0°$	$\theta = 90°$
Detectivity Measurement (Fields ON)	$120\ fT/\sqrt{Hz}$	$480fT/\sqrt{Hz}$
Detectivity Measurement (Fields OFF)	$145fT/\sqrt{Hz}$	$145fT/\sqrt{Hz}$

Table 4.2: Detectivity measurement of an YBaCuO sensor

In Table 4.2, we see that the detectivity does not suffer from MRI conditions. Pulses do not blank the response and the permanent magnetic field has a beneficial effect on the detectivity. As we have seen previously, a good orientation helps centering and linearizing the giant magnetoresistance response. Moreover, field and gradients supplies add only strong specific noise peak which can be easily avoided by working at pertinent frequencies. This lead to an increase of our detectivity.

An important drawback of the cryogenic dewar is its filtering due to its super-isolation. According to the working temperature (77K or 4K), the signal "seen" by the sensor should be weighted by an attenuation factor.

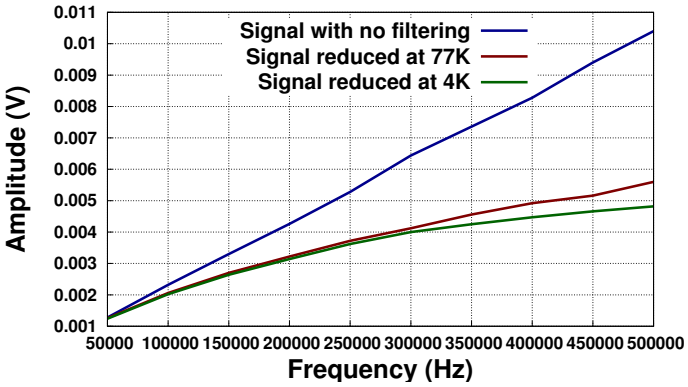

Figure 4.13: Experimental measurements of the superisolation effect on signal

This filtering could be avoided with a different cryogenic dewar geometry. All detectivity measurements performed are corrected by those factors to reflect the intrinsic sensitivity of mixed sensors.

All Sensitec YBaCuO sensors that have been tested around 300 kHz had a detectivity from 70 $fT/\sqrt{Hz}$ to 150 $fT/\sqrt{Hz}$. This is 100 times worse than a tuned coil at this frequency with a Q factor of 100. For a simple NMR measurement, this implies an averaging approximately 10 000 times longer than with a tuned coil to achieve the same signal-to-noise ratio. We performed one NMR measurement, to check the reliability of those predictions, but all MRI attempts are excluded with such detectivity. A bottle a water was used with a classic 90° pulse sequence with 1 second repetition time. The signal was averaged during 2 minutes for both configurations. The bottle was at the same distance of the tuned coil and the mixed sensor.

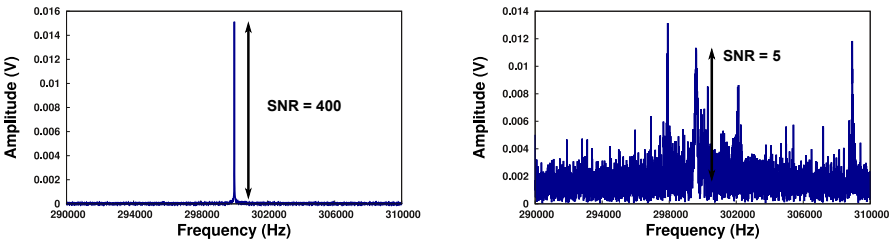

(a) (b)

Figure 4.14: NMR Signal with a) a tuned coil and b) a mixed sensor. Both sensors are at the same distance of the sample (5 cm).

This YBaCuO mixed sensor has a detectivity around 100 $fT/\sqrt{Hz}$. It's signal-to-noise ratio is 80 times lower than a tuned coil for a same averaging time. This difference comes from the attenuation due to the super-isolation (factor 1.6 at 300 kHz), the filling factor (tuned coil of 28 cm^2 and mixed sensor of 1 cm^2) and finally the detectivity. If we neglect the effect of the size, the detectivity of the tuned coil is experimentally around 2 $fT/\sqrt{Hz}$ here.

Those first results highlight the necessity of using another configuration to detect efficiently NMR signals with a mixed sensor. As for SQUIDs and Atomic Magnetometers, this implies the use of flux transformers.

4.2 INTRODUCTION TO FLUX TRANSFORMERS

Using a mixed sensor imposes some restrictions. For medical applications, working at low temperature (77K or 4K) and having a sensor with rigid shape raise important issues directly impacting the signal to noise ratio. Therefore, in real experiment conditions, tuned coils are always superior to mixed sensors because of a better filling factor. As for SQUIDs and Atomic Optical Magnetometers, the use of a flux transformer allows to be more adaptable. A pair of two coils are linked together, the pickup coil and the input coil, respectively coupled to the mixed sensor's superconductive loop and the sample.

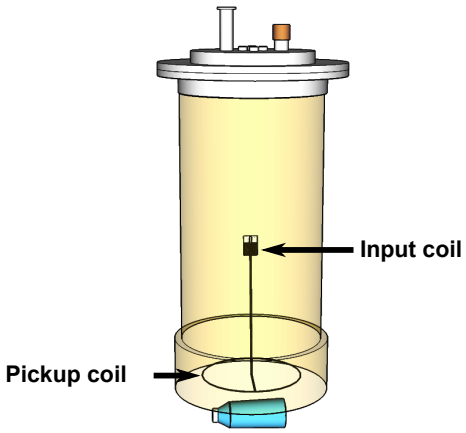

Figure 4.15: Flux transformer configuration in a cryogenic environement

A cryogenic dewar has been used to test limits of flux transformers. Three types of flux transformers have been simulated and experimentally tested to determine relevant configurations for very low field applications : Superconducting, resistive and tuned flux transformers.

4.2.1 *Non resistive flux transformer*

The first flux transformer that was tested was a superconductive flux transformer. Using a niobium wire, we realized a non resistive flux transformer working at 4K.

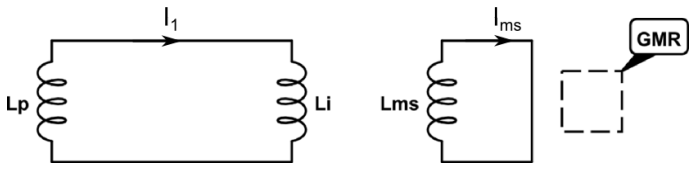

Figure 4.16: Electronic scheme of a non resistive flux transformer circuit coupled to a mixed sensor

The gain of this flux transformer is defined as :

$$G = \frac{L_{ms} I_{ms}}{\phi}$$

where ϕ is an external calibrated field which is applied on the pickup coil. To calculate this gain, we use the Faraday's Law which gives us:

$$\begin{cases} 0 & = Z_1 I_1 + N_{L_p} \frac{d\phi}{dt} + N_{L_i} \frac{d\phi_{2\to1}}{dt} \\ 0 & = N_{L_{ms}} \frac{d\phi_{1\to2}}{dt} + N_{L_{ms}} \frac{d\phi_{sens}}{dt} \end{cases}$$

where $\phi_{2\to1}$ and $\phi_{1\to2}$ are respectively the flux influence of the superconducting loop on the input coil and conversely. It leads to

$$\begin{cases} -N_{L_p} j\omega\phi - j\omega M I_{ms} & = Z_1 I_1 \\ -j\omega M I_1 - j\omega L_{ms} I_{ms} & = 0 \end{cases}$$

where M is the mutual inductance between the superconducting loop and the input coil. It can be expressed as $M = k\sqrt{L_{ms} L_i}$ where k is the coupling coefficient. Then,

$$\begin{cases} -N_{L_p} j\omega\phi & = Z_1 I_1 + j\omega M I_{ms} \\ -\frac{L_{ms} I_{ms}}{M} & = I_1 \end{cases}$$

Finally,

$$G = N_{L_p} * \mid \frac{Z_1}{j\omega M} - \frac{M}{L_{ms}} \mid^{-1} \tag{4.1}$$

The gain can be maximized by adapting L_i and L_p

$$\frac{\partial G}{\partial L_i} = 0 \Longrightarrow L_p = (1 - k^2) L_i \tag{4.2}$$

To obtain the detectivity of this entire device, we need to take into account all contributions to the noise. The Johnson noise coming from GMRs is the main source as our superconductive flux transformer has no resistance. In term of magnetic field, GMRs' noise can be expressed as :

$$B_{GMR\,Noise} = \frac{\sqrt{4 k_b R_{GMR} T_{GMR}}}{V_B} \tag{4.3}$$

where V_B is the voltage response per field unit of this sensor. Finally, we can expressed the detectivity as

$$Detectivity = \frac{A_{ms}}{A_p} * \frac{B_{GMR\,Noise}}{G}$$

A simulation is performed for a YBaCuO Sensitec mixed sensor of 1 cm^2 , with a detectivity in the thermal regime of 42 $fT/\sqrt{Hz}$ for 10V (210 $fT/\sqrt{Hz}$ for 2V) at 4K coupled ($k \approx 0.6$) with an adapted flux

transformer in niobium with a pickup diameter of Ø=3 cm. This simulation is accurate as soon as the 1/f noise is negligible. The model predicts a detectivity of 10 $fT/\sqrt{Hz}$ at 10 V (50 $fT/\sqrt{Hz}$ at 2V) (see Figure 4.18). The detectivity is then measured experimentally between 5 kHz and 410 kHz (see Figure 4.17).

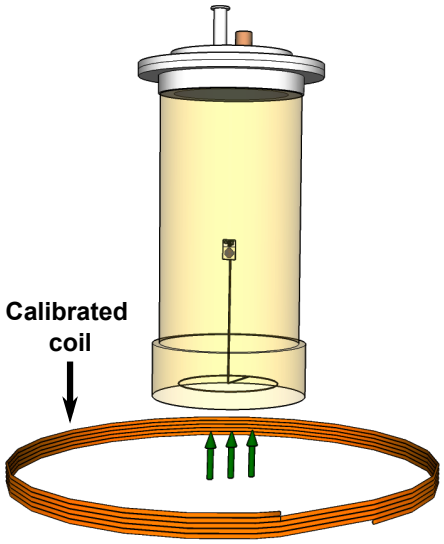

Figure 4.17: Experimental setup for detectivity measurements

A large emission coil is used to obtain a precise defined field at the center. The calibration is done by sending 1A in the emission coil and measuring the corresponding field using a gaussmeter. The calibration has also been verified with a SQUID sensor. As we are using a voltage function generator, the emission coil impedance needs to be constant over frequency. As a result, a high resistance ($120k\Omega \gg L\omega$) is associated to the emission coil which is only composed of 2 turns to minimize its inductance. We also had to consider the cryogenic dewar's superisolation effect on the effective field seen by our sensor (see 4.13). We used the corresponding coefficients to correct our detectivity measurement (see 4.18).

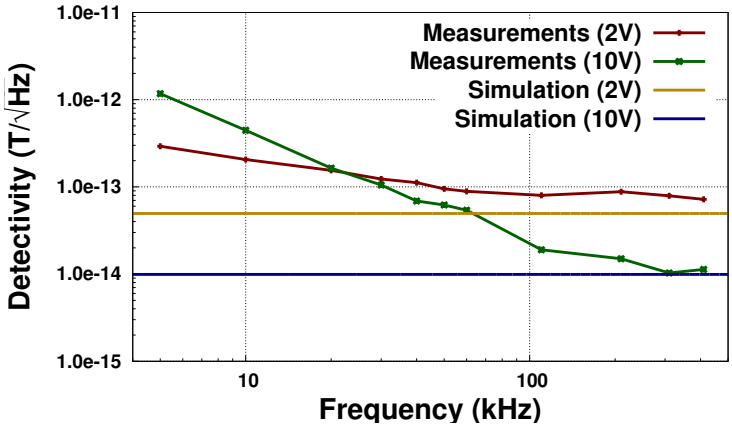

Figure 4.18: Detectivity of a Non Resistive Flux Transformer

This YBaCuO sensor presents an important $1/f$ noise as we have already seen previously. At 2 V, the detectivity is close from simulations above 80 kHz. We reach a detectivity around 75 $fT/\sqrt{Hz}$ (50 $fT/\sqrt{Hz}$ predicted). At 10V, the detectivity is close from simulations above 300 kHz. We reach a detectivity around 11 $fT/\sqrt{Hz}$ (10 $fT/\sqrt{Hz}$ predicted). Below 300 kHz at 10V and below 50 kHz at 2V, the simulation is not correct anymore as the $1/f$ noise is dominating.

It can be noticed that the voltage supply should be adapted according to the working permanent field to obtain an ideal detectivity. Performances are still worse than tuned coils and the use of liquid helium is not trivial.

4.2.2 *Resistive flux transformer*

This configuration is really close from the previous one except we now have a resistance R.

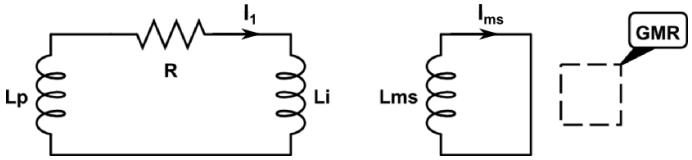

Figure 4.19: Electronic scheme of a resistive flux transformer circuit coupled to a mixed sensor.

The gain can still be expressed by equation 4.1 . This resistance introduces a low frequency filter (RL) with a cutoff frequency

$$\omega_c = \frac{R}{L_i + L_p + \frac{M^2}{L_{ms}}}$$

At very low field, the working frequency ω should always be higher than ω_c and then equation 4.2 to maximize the gain is still true. How-

ever a resistance comes with thermal noise that we need to take into account. It can be expressed like

$$\begin{cases} \sqrt{4k_b R_{TF} T_{TF}} & = Z_1 I_1 + j\omega M I_{ms} \\ L_{ms} I_{ms} & = -M I_1 \end{cases}$$

We can then write the noise contribution of the flux transformer like

$$B_{FT\,Noise} * A_{ms} = L_m I_{ms} = \mid \frac{-M\sqrt{4k_b R_{TF} T_{TF}}}{Z_1} * (1 - \frac{j\omega M^2}{Z_1 L_{ms}})^{-1} \mid \quad (4.4)$$

or

$$B_{FT\,Noise} * A_{ms} = L_m I_{ms} = \mid \frac{-j\omega M^2\sqrt{4k_b R_{TF} T_{TF}}}{N_p * Z_1^2} * G \mid$$

Finally, the detectivity becomes

$$Detectivity = \frac{A_{ms}}{A_p} * \frac{\sqrt{(B^2_{GMR\,Noise} + B^2_{FT\,Noise})}}{G}$$

Another simulation is performed with the same YBaCuO sensor of 1 cm^2 used previously. In liquid nitrogen (77 K), its detectivity is around 120 $fT/\sqrt{Hz}$ at 10V (600 $fT/\sqrt{Hz}$ at 2V) in the thermal regime. It is coupled ($k \approx 0.6$) with an adapted flux transformer in copper with a pickup diameter of Ø=3 cm. The introduced resistance has been measured experimentally at 77 K around 55 $m\Omega$ (35 $m\Omega$ due to the input coil and 20 $m\Omega$ do to the pickup coil). The model predicts a detectivity of 28 $fT/\sqrt{Hz}$ at 10V (140 $fT/\sqrt{Hz}$ at 2V) for frequencies above ω_c (see Figure 4.20).

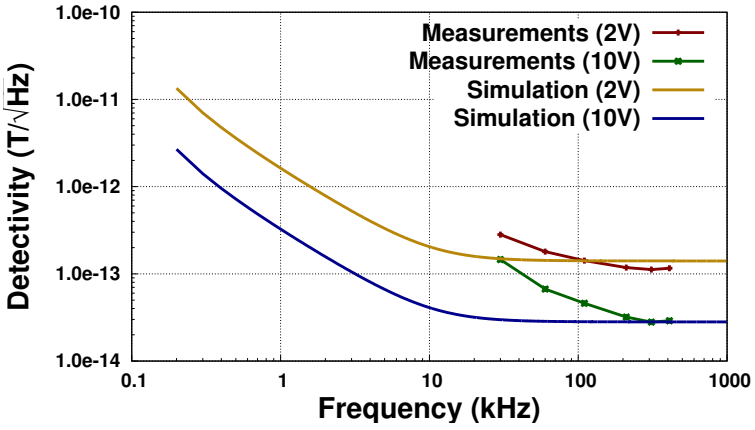

Figure 4.20: Detectivity of a Resistive Flux Transformer

The detectivity is then measured experimentally between 5 kHz and 410 kHz. We use the same measurement setup as before but super-isolation does not have the same behavior at 77K (Figure 4.13). We used the new corresponding coefficients to correct our measurements. In Figure 4.20, the $1/f$ noise is degrading the detectivity. At 10

V, we have to work above 300 kHz to be in the thermal noise regime and we measure a detectivity of 29 $fT/\sqrt{Hz}$. At 2 V, the working zone is above 100 kHz and we measure a detectivity of 116 $fT/\sqrt{Hz}$. Below those thresholds, the $1/f$ noise is dominating and the simulation is not accurate anymore. A clear signature of the high pass filter would be a detectivity curve with a slope steeper than $1/f$. It seems that above 30 kHz we have no filtering effect as predicted.

4.2.3 *Tuned flux transformer in series*

To obtain a resonant circuit, we add a capacitance in series to the previous configuration.

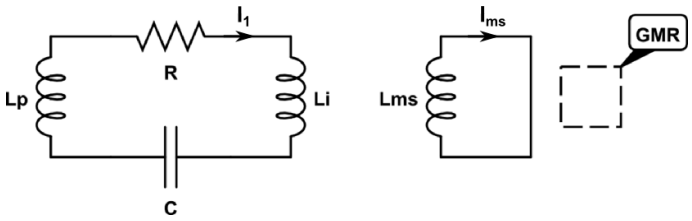

Figure 4.21: Electronic scheme of a tuned flux transformer circuit coupled with a mixed sensor

According to equations 4.1, the gain resonant frequency can be expressed

$$\omega_0 = \frac{1}{\sqrt{C} * \sqrt{(1-k^2)L_i + L_p - \frac{CR^2}{2}}}$$

At ω_0, the pickup coil's inductance needs to be matched to the input coil to maximize the gain of the flux transformer. The analytical expression allow us to predict (Figure 4.22) this value of L_p.

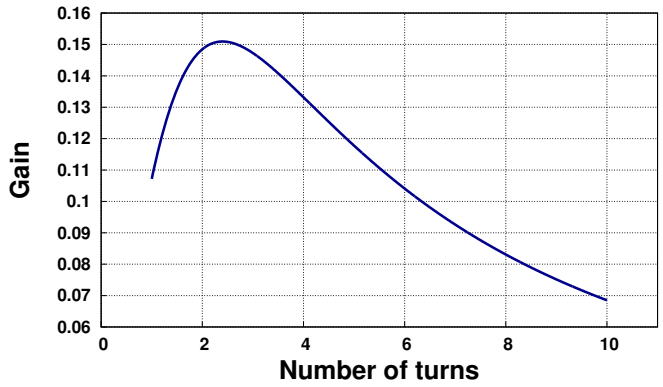

Figure 4.22: Simulation of the gain of a tuned flux transformer at ω_0 according to the number of pickup coil's turn

We plot the detectivity profile of a tuned flux transformer which is built to resonate at 70 kHz and 300 kHz with respective quality

factors of 2 and 20 (to fit with experimental measurements). Both are optimized with the correct pickup coil inductance.

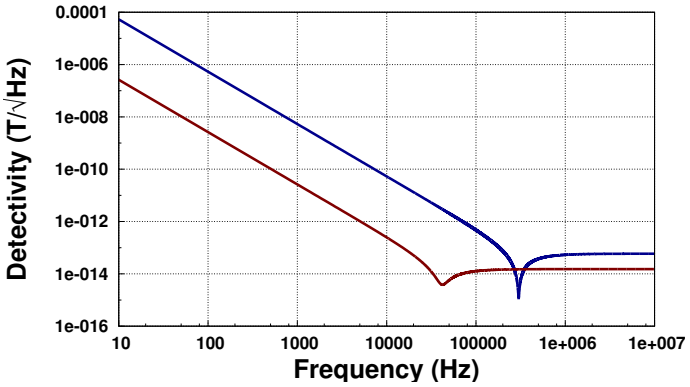

Figure 4.23: The detectivity of a Tuned Flux Transformer

At resonance, we predict a detectivity of 0.7 $fT/\sqrt{Hz}$ at 300 kHz and 3.1 $fT/\sqrt{Hz}$ at 70 kHz. We performed an experimental measurement with the same YBaCuO sensor used previously at 77K. The quality factor Q of the flux transformer was about 20 at 300 kHz and 2 at 70 kHz.

	Detectivity Simulated ($fT/\sqrt{Hz}$)	Detectivity Measured ($fT/\sqrt{Hz}$)
NAOMI + Tuned FT 300 kHz	0.7	1.7
NAOMI + Tuned FT 70 kHz	3.1	6.3

Table 4.3: Detectivity measurements with a calibrated signal ($B_{rms} = 5.1$ nT)

The detectivity has been systematically under-evaluated because of the $1/f$ noise component that has a strong impact on the noise. In this configuration, we are competitive enough to consider NMR and MRI measurements.

4.3 IMPLEMENTATION OF FLUX TRANSFORMERS

The flux transformer is clearly an important asset for mixed sensors. However, several parameters need to be precisely controlled in order to achieve an efficient combination. The resistance of the wire has an important impact on the noise and the signal. The use of specific geometries with special wires is discussed here. The coupling between the superconducting loop and the input coil is also critical and needs to be maximized. A method to measure this coupling coefficient and different input coil geometries is presented. A simulation with different superconducting loop size is also performed to predict an ideal size to obtain a maximum detectivity. Finally, a sensor combined to a tuned flux transformer is integrated in the small MRI setup. Noise measurements are performed as well as NMR acquisitions.

4.3.1 *Resistance*

The flux transformer's resistance determines two important characteristics : the cutoff frequency and the thermal noise. In both cases, the resistance needs to be minimized. However, at 300 kHz we have to compose with the tendency of the electric current to concentrate near the surface of the conductor, known as the "skin effect". The use of a specific wire (Figure [4.24]), composed of several isolated wire in parallel, attenuates strongly this effect.

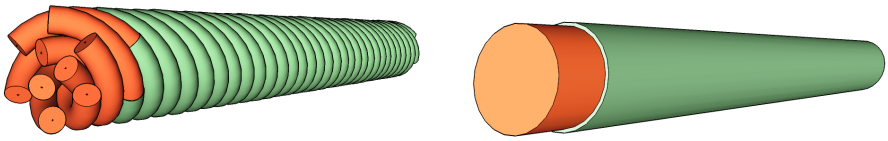

(a) (b)

Figure 4.24: Section of a) Litz wires and b) normal wires. The conductive part is orange and the insulating part is green.

A resistance evaluation of two different wires, one normal and one woven, has been calculated at 300 kHz at a temperature of 300K. Both have a total diameter of 2 mm but the Litz wire is composed of 9 smaller wires. As we can see in Table [4.4], the drop in resistance is substantial.

	Normal Wire	**Litz Wire (9 Smaller Wires)**
Skin Effect Depth (mm)	0.1	0.1
Effective Surface(mm^2)	0.6	1.6
Resistance $(m\Omega.m^{-1})$	27	10

Table 4.4: Resistance of different type of wires at 300 kHz

According to typical inductance and coupling values of low field flux transformers, the total resistance should be lower or equal to 600 $m\Omega$ for a cutoff frequency below 42 kHz (1 mT). We achieve a 50 $m\Omega$ flux transformer using a large ($\varnothing = 0.5mm^2$) litz wire composed of 125 strings for the pickup coil and a thin ($\varnothing = 0.05mm^2$) litz wire composed of 12 strings for the input coil. A larger wire could be used for the pickup coil as the space is not a limitation. For the input coil, the mixed sensor size is limiting wires thickness. Because of the specific geometry of this coil, a larger wire would lead to a loss in coupling and inductance.

4.3.2 *Coupling*

The coupling coefficient k is of prime importance as it determines equilibrium between input and pickup coils and the "amount" of signal we transmit to the mixed sensor. Its measurement is not straight forward and some superconductive loop properties have to be used. We will present here a relatively simple method to evaluate this coupling coefficient. An input coil is coupled to the mixed sensor and connected to a preamplifier and a band-pass filter to be monitored. A large "bias" coil is fed by a current AC generator to create an oscillating magnetic field on the sensor and the input. Both responses are measured.

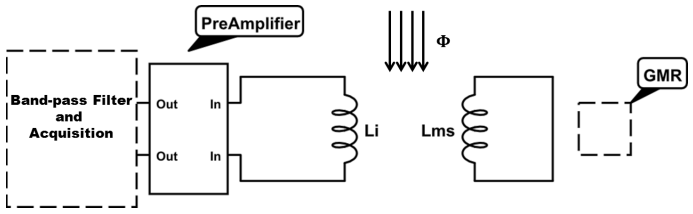

Figure 4.25: Coupling coefficient measurement setup

The magnetic field is high enough to saturate the superconductive loop. The input coil signal is changing depending on whether the su-

perconductive loop is in "saturated" mode or not. First, we'll consider it is not saturated. We know that we have no tension in the superconductive loop and no current in the input coil. Faraday's law gives us :

$$V_2 = 0 = \frac{d\phi_{ext}}{dt} + \frac{d\phi_{sens}}{dt}$$

Here, ϕ_{ext} is the flux created with the bias coil and ϕ_{sens} is the flux created with the superconducting loop to cancel ϕ_{ext} . This leads to :

$$\phi_{ext} = -L_{ms} I_{ms} \tag{4.5}$$

We write the same equation for the input coil :

$$V_1 = N_1 (\frac{d\phi_{ext}}{dt} + \frac{d\phi_{sens \to input}}{dt})$$

Here, $\phi_{sens \to input}$ is the flux induced by the superconducting loop in the input coil due to the mutual inductance. N_1 is the number of turn of the input coil.

$$V_1 = N_1 \omega \phi_{ext} + \omega M I_{ms}$$

Here $M = k\sqrt{L_i L_{ms}}$ is the mutual inductance . Using 4.5, we obtain :

$$V_1 = \omega \phi_{ext} (N_1 - \frac{M}{L_{ms}})$$

We now consider the superconducting loop as saturated which means that it is not able to screen the external magnetic field. The voltage we measure in the input coil becomes :

$$V_{1s} = N_1 \omega \phi_{ext}$$

To obtain k , we do :

$$\frac{V_1}{V_{1s}} = 1 - \frac{M}{L_{ms} N_1} = 1 - \frac{k}{N_1}\sqrt{\frac{L_i}{L_{ms}}}$$

Finally,

$$k = 1 - \frac{V_1}{V_{1s}}$$

A triangular wave at 3 kHz with an amplitude of 50 mA is sent into the "bias" coil. A 1 cm^2 mixed sensor at 77K is coupled to a classic input coil. Both responses are averaged 512 times. Figure 4.26 presents distinctly the change of behavior of the input coil when the superconductive loop becomes saturated.

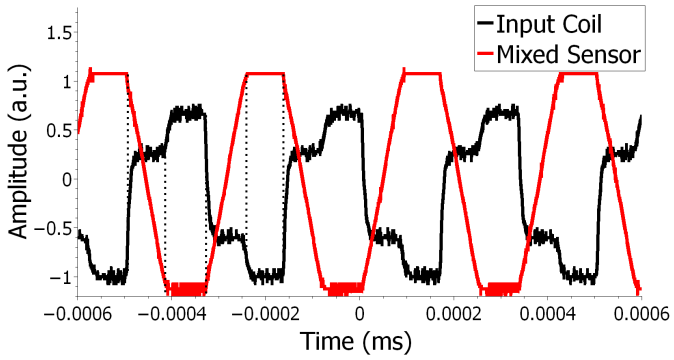

Figure 4.26: Coupling Coefficient Measurement

To maximize the coupling coefficient, we tried two geometries of input coil. One with turns concentrated at the circumference (C coils), an other one with turns distributed across the diameter (D coils) (Figure 4.27). Both are then sticked to the superconducticve loop using Kapton.

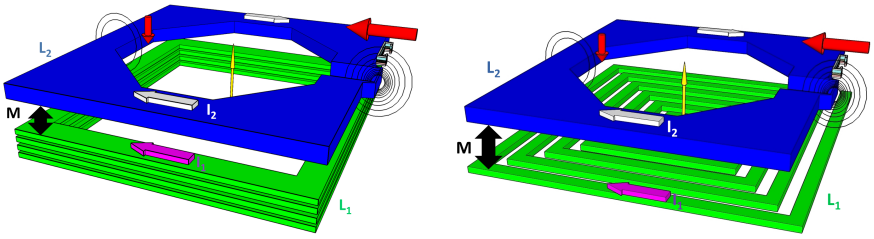

(a) (b)

Figure 4.27: Input coil geometry with a) a coil with turns concentrated at the circumference (C) and b) a coil with turns distributed across the diameter (D)

As predicted by M. Zierhofer [57], the distributed D coil presents a better coupling coefficient. The mixed sensor specific geometry doesn't influence that. We tried different numbers of turns but the changes were negligible (Table 4.5).

	D Input Coil	**D Input Coil**	**C Input Coil**
N	15	7	7
V_{1s}	0.384	0.347	0.234
V_1	0.156	0.139	0.122
k	0.59	0.6	0.47
L_i	$7.6 * 10^{-8}$	$7.1 * 10^{-7}$	$2.1 * 10^{-7}$

Table 4.5: Coupling coefficient for different input coils

For low field MRI, a distributed concentric input coil with the maximum number of turns to maximize the inductance is the best configuration. This inductance is related to wires diameter which is limited by our low resistance requirement.

4.3.3 *Size of the sensor*

A threshold resistance has been determined as well as an input geometry also. Now the only parameter that still remains is the size of the mixed sensor we are using. For the same resistance, we can have a big mixed sensor with a huge input coil which induces a pickup coil with lots of turns. Or on the other side, we can have the smallest sensor with an adapted input coil inducing a 1 turn pickup coil (which is the inferior limit of our system). We tried to simulate the signal-to-noise ratio of this system, according to the dimension of our sensor.

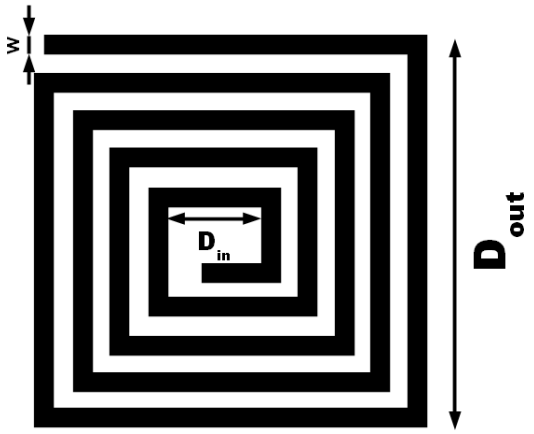

Figure 4.28: Input Coil Dimensions

The flux transformer resistance was considered as constant. When the sensor's side D_{out} is increasing, the wire's diameter w is increasing also so that R doesn't change. The resulting inductance of L_i is calculated. According to [39], we have

$$L_i = 2.34\mu_0 \frac{\left(\frac{D_{out}-D_{in}}{w}\right)^2 \left(\frac{D_{out}+D_{in}}{2}\right)}{1+2.75\frac{D_{out}-D_{in}}{D_{out}+D_{in}}}$$

Then we consider this flux transformer as equilibrated and we deduce easily Lp. Finally we obtain the signal-to-noise ratio variation of a classic flux transformer according to the lateral size D of the mixed sensor.

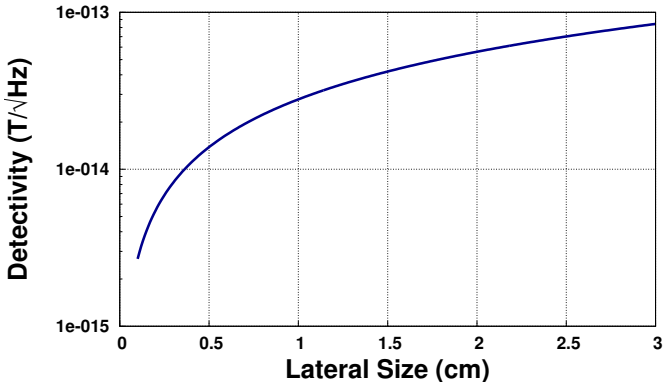

Figure 4.29: Evolution of the detectivity of a mixed sensor coupled with a resistive flux transformer according to the sensor's size

This simulation (4.29) shows that we should minimize the size of the sensor. For an efficient design, the size of the pickup coil should first be adapted to the sample. Then its inductance should be measured for one turn and then the ideal size of the sensor should be deduced.

4.3.4 *Noise, signal and MRI devices*

The geometry of this sensor is very different from the classical tuned coil. Its sensitivity to the external noise, coming from the lab or from MRI power supplies, could be very different. We performed two tests at 300 kHz with a YBaCuO sensor of 1500 Ohms. One measurement was performed inside the MRI system but all devices were off. An other measurement was performed with all power supplies on, with active gradients and pulses sequences.

	Off Configuration	On Configuration
Noise ($nV/\sqrt{Hz}$)	5.51	5.87

Table 4.6: Noise according to MRI activity

Table 4.6 shows almost no differences between the two states. It should be noticed though that some parasitic signals with huge intensity comes with some supply devices (DC current and Pulses) but they appear at very specific frequencies which can be easily avoid or filtered to perform MRI. Another specific difference with this configuration is the position of the sensor. In a non ideal configuration (Figure 4.30), we see that the sensor is inside the permanent field. Its hard layer is in the direction of the permanent field. As we can turn our dewar inside the field, we can change the sensor orientation in the permanent field to linearize it. This way we can chose the position to maximize the GMR response and use this as an advantage.

4.3.5 *Nuclear Magnetic Resonance*

A YBaCuO sensor with a resistance of 1.8 $k\Omega$ and a detectivity of 120 fT is coupled to a flux transformer tuned at 300 kHz with a Q factor of 20. The set is cooled down at 77K and reaches a detectivity of 1.75 $fT/\sqrt{Hz}$ (same configuration than 4.2). We compare it to a classic tuned coil which is intentionally far from the sample to have the same filling factor in both cases (Figure 4.30).

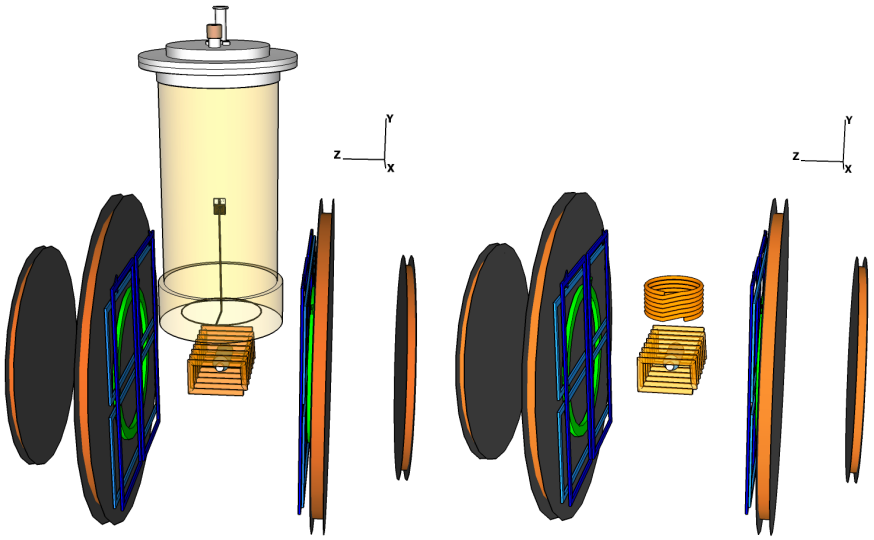

(a) (b)

Figure 4.30: Full setup with a) a mixed sensor coupled to a flux transformer at 77K and b) a tuned coil

An NMR FID was acquired first with the mixed sensor. A $\frac{\pi}{2}$ pulse was applied on a water sample under 7 mT (300 kHz). The FID signal was averaged 100 times.

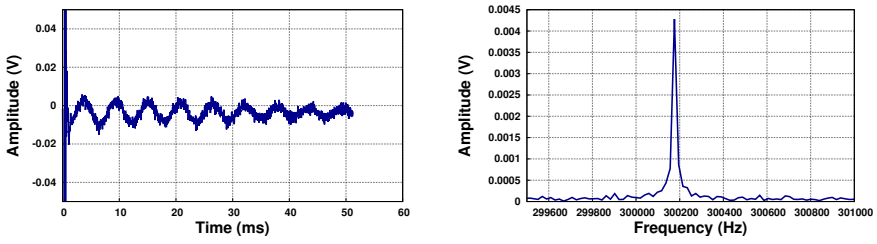

(a) (b)

Figure 4.31: a) NMR Signal with a mixed sensor coupled with a tuned flux transformer and b) its Fourier Transform

Strong pulses has no effect on the sensor. The signal-to-noise ratio ($\frac{P_{signal}}{P_{noise}}$) for 100 acquisitions was around 76. An NMR experiment with a tuned coil in the same conditions is also performed.

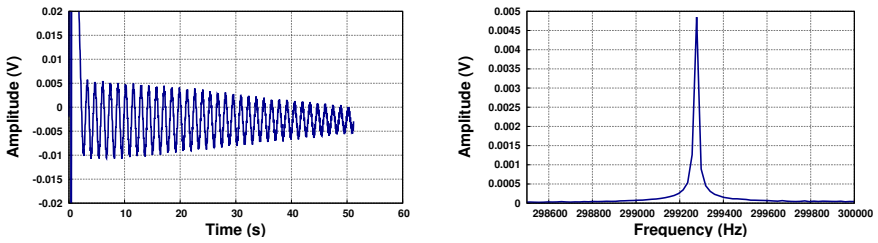

(a) (b)

Figure 4.32: a) NMR Signal with a tuned coil and b) its Fourier Transform

The signal-to-noise ratio for 100 acquisitions is around 112. This is higher than the mixed sensor measurement but this is due to the attenuation of the super-isolation. The use of a classic NMR sequence is fully compatible with our new detection method.

CONCLUSION

In this chapter, we have seen that mixed sensor were presenting interesting characteristics for MRI applications. First they exhibit a good detectivity in the thermal noise regime (around 30 $fT/\sqrt{Hz}$ with homemade sensors). It can be used straightly inside an MRI setup as it is robust against permanent magnetic field providing that a proper orientation is chosen. However, like for SQUIDs and Atomic Magnetometers, the use of an intermediate flux transformer is more advantageous. Figure 4.33 presents the detectivity of all previous detection method. The tuned coil and the tuned flux transformer are considered to be tuned at all frequencies (the capacitance is changed at each point).

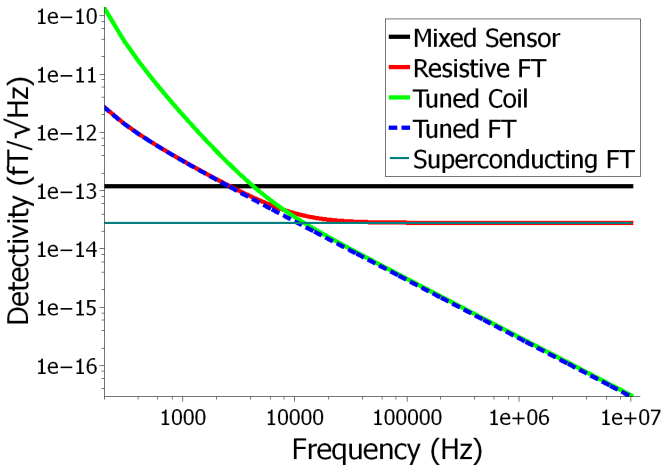

Figure 4.33: Detectivity profile of several detection devices

The compilation of those results gives us a global picture of our options. The superconducting flux transformer is interesting mainly

because it doesn't add any resistive noise to the system. The gain in detectivity is better than with a resistive tuned flux transformer only because of the working temperature (77 K for the resistive flux transformer and 4 K for the superconducting flux transformer). We achieve a detectivity of 11 $fT/\sqrt{Hz}$ at 300 kHz. The resistive flux transformer is then very interesting as it is much easier to manipulate copper instead of niobium. The cutoff frequency is too low to be a problem for very low field MRI. At 77 K, we achieve a detectivity of 28 $fT/\sqrt{Hz}$ at 300 kHz. Still those solutions present a detectivity at least ten times worse than tuned coils. The use of a mixed sensor with a detectivity around 10 $fT/\sqrt{Hz}$ would be enough to obtain a competitive untuned system. Homemade sensors with such characteristics have been processed but they are still too fragile to be experimentally used for MRI. This is why the tuned flux transformer has been proposed. In this configuration, a detectivity of 1.7 $fT/\sqrt{Hz}$ has been achieved at 300 kHz with a Q = 20. It is close from tuned coils (1.9 $fT/\sqrt{Hz}$ for a Q = 100) but with a detection bandwidth five times larger. The use of a better mixed sensor would be beneficial to a lesser extent in this configuration. Indeed, the thermal noise coming from the flux transformer is not anymore negligible (around 0.9 $fT/\sqrt{Hz}$ for this particular wire).

A method has been proposed to design a flux transformer properly. First the resistance has been reduced using Litz wires. The most resistive part is coming from the input coil wire that is limited in size because of geometric constrains. Indeed a good coupling coefficient is needed between the superconducting loop and the input coil which imposes precise winding geometry. We achieved a maximum coupling coefficient k = 0.6. We could not manage to test all configurations with sensors of different size but the simulation suggests that it should be chosen precisely according to the pickup coil. The size of the pickup coil was limited because of the cryogenic dewar. The 1 cm^2 mixed sensor was about twice larger than the ideal size. We could have won approximately a factor two in detectivity with a 0.5 cm^2 sensor.

Finally, NMR measurements have been performed to compare a tuned coil and a mixed sensor combined with a tuned flux transformer. The signal-to-noise ratio obtained is in agreement with previous measurements and is compatible with MRI imaging perspective.

5

CLASSIC SEQUENCES

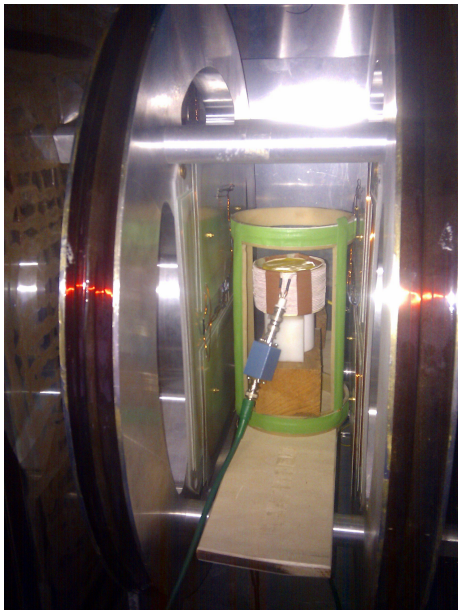

Small MRI setup before a three dimensional acquisition

In this chapter, first Magnetic Resonance Imaging results are presented. Three dimensional images are performed through double phase encoding and slice selection sequences. Experimental phantoms and in-vivo tissues have been acquired with mixed sensors and tuned coils. The impact of metallic implants has been evaluated with titanium metallic pieces and aluminum can. Finally, specific sequences for relaxometry study are presented. They have been tested on several liquids and in-vivo tissues.

5.1 FIRST STEPS INTO IMAGING

Two MRI devices have been built and sensors have been precisely characterized. MRI experiments need to be performed to test the consistency of the entire setup. Basic imaging sequences have been introduced into both MRI system. First a double phase encoding spin echo sequence has been designed especially for very low field MRI. However this method is time consuming and restrictive in terms of reconstruction. A slice selection spin echo sequence has been incorporated. The question of metallic implants is also discussed through several experiments as their influence at very low field MRI is not clearly defined. However, studies have been realized at ultra low field by Clarke et al. and behaviors between 10 mT MRI and 100 μT MRI will be compared. All images have been acquired with tuned coils as it was easier to adapt the geometry to the various phantoms used. However, an MRI image has been performed with a mixed sensor combined with a tuned flux transformer to demonstrate the practicability of the sensor. Finally, in vivo imaging has been tested. All those experiments have been performed in the small MRI setup.

5.1.1 *Double phase encoding*

In chapter 1, we've seen that it was possible to acquire a three dimensional image with a double phase encoding without using any selection pulse. There is two main advantages with this sequence.

The time spent for one acquisition is smaller than slice selection sequence. The pulse doesn't need to be selective. For a 5 cm x 5 cm x 5 cm sample at 10 mT, the NMR width is around 20 Hz. Then according to Chapter 2,

$$\frac{2\pi}{\gamma B_0} \ll T \leq \frac{1}{\Delta f}$$

Therefore, the pulse length can be chosen between 140 μs and 50 ms . To minimize the acquisition time, we are using a pulse around 140 μs in double phase encoding sequences.

A contiguous structure of slices is also typical with such cycle. It offers an ease of use for images interpretation.

Three dimensional imaging examples are presented here. The first one is a cylindrical bottle (l = 4 cm and Ø = 2 cm) filled with water doped with Copper Sulfate. Its T_2 and T_1 have been estimated respectively around 75 ms and 95 ms. A double phase encoding sequence is used to acquire an image with a Field of View of 2048 points x 32 points x 32 points at 7 mT. Each voxel is averaged 100 times for a total acquisition time of 12 hours. The gradients are set to target a resolution of 2 mm^3. The chosen echo time TE is 25 ms and the repetition time TR is 500 ms. Figure 5.18 presents only relevant slices after a three dimensional Fast Fourier reconstruction.

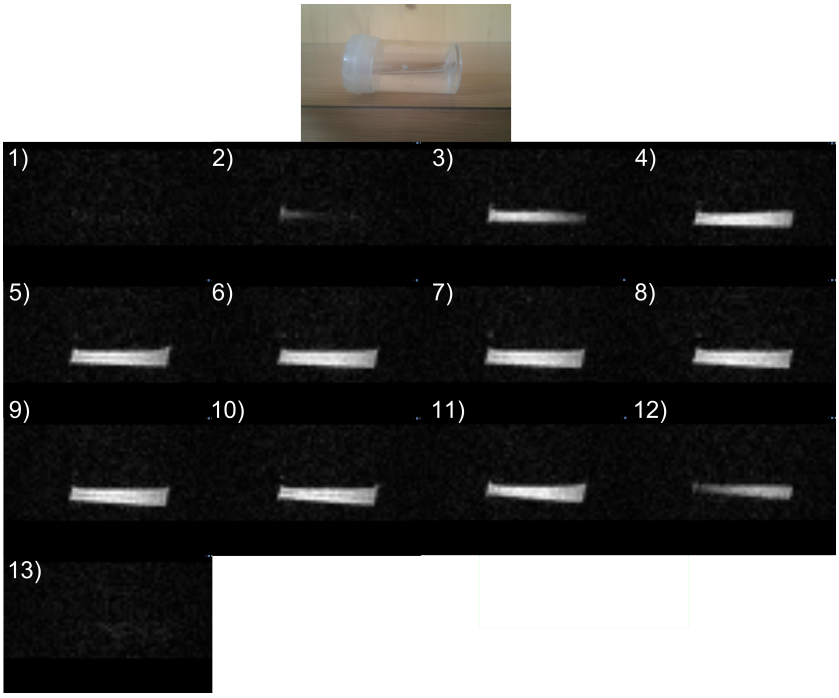

Figure 5.1: Three dimensional imaging of a bottle at 7 mT with a tuned coil (TE=25ms, TR=500ms). The 13th slices of 2mm each are presented here.

Another three dimensional imaging was performed to test our resolution. A small cylindrical piece of plastic (l = 3 cm and Ø = 1 mm) was introduced in the previous bottle. Same parameters as before are used but the gradients are increased to reach a 1 mm^3 voxel. A three dimensional representation is given in Figure 5.2.

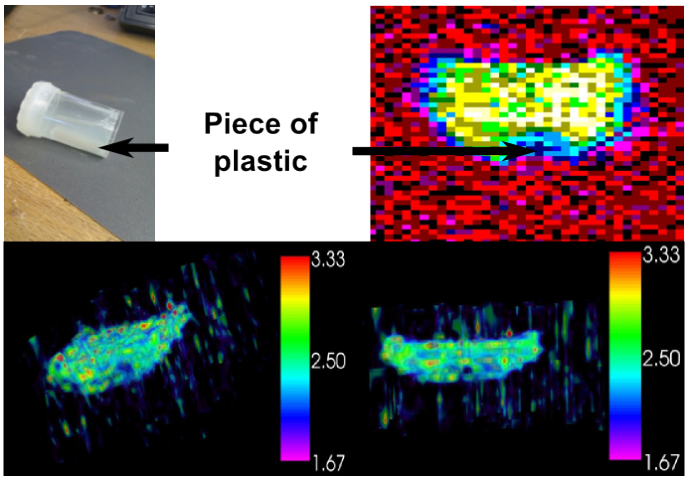

Figure 5.2: Three dimensional imaging of a bottle containing a plastic stick at 7 mT with a tuned coil (TE=25ms, TR=500ms).

However double phase encoding has some disadvantages. Image processing is longer since three Fast Fourier Transformations have to

be performed in order to produce an image. Moreover the entire three dimensional K-space needs to be acquired for a correct reconstruction. It is then impossible to reduce the acquisition time by focusing on a specific slice. It explains mainly why no in-vivo acquisition were performed using a double phase encoding sequence.

5.1.2 *Slice selection*

Another possibility for three dimensional imaging is to use slice selection sequence (see Chapter 1). This type of acquisition is comfortable for two main reasons.

The reconstruction slice by slice opens up possibility of imaging just some particular relevant zone of our sample. It is then possible to decrease the acquisition time drastically as we do not have to image the entire volume. Moreover, a two dimensional Fast Fourier Transform is sufficient to reconstruct a slice, reducing the post-processing time.

The independent relaxation time of each slice could allow the use of parallel sequences. One slice could be acquired while another slice would be relaxing from a previous acquisition. The entire acquisition time could be then reduced.

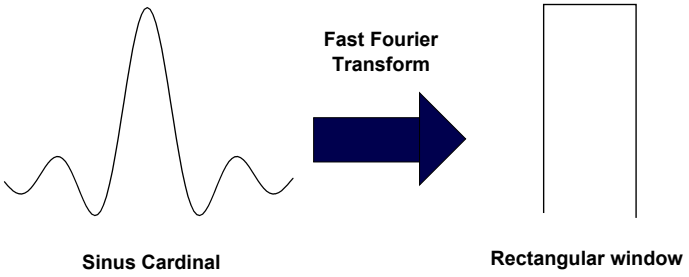

Figure 5.3: Ideal pulse to excite a perfect rectangular window.

A cardinal sinus pulse is used to reduce at its maximum the side lobes. As we can not used a infinite pulse to achieve a perfect cardinal sinus, the excited zone is not perfectly rectangular. To estimate those parasite side lobes, we use a specific configuration of two bottles placed at different heights and filled with water doped with Copper Sulfate (T_1 and T_2 close from 50 ms). A selective pulse of 8 ms is applied before a classic spin echo sequence with an echo time of 25 ms and a repetition time of 300 ms. The targeted resolution is a 2 mm slice with an in-plane resolution of 2 mm x 2 mm.

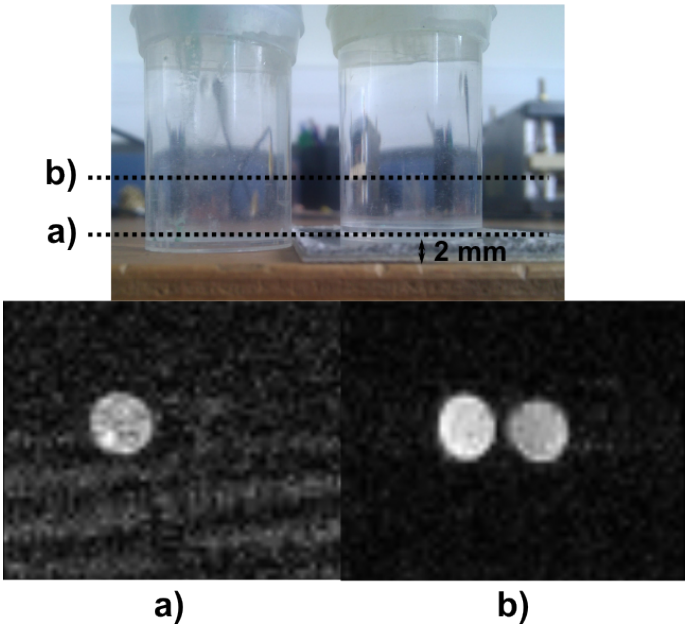

Figure 5.4: Slice selection images. a) The first slice is performed to demonstrate the feasibility of 2 mm thickness and b) the second slice to demonstrate the slice scanning capability.

On Figure 5.4, adjacent slices have a negligible influence and a 2 millimeters slice is achieved in 15 min. With such sequences, the necessary time to perform one slice acquisition is compatible with in vivo imaging.

5.1.3 *Mixed sensors vs tuned coils*

MRI is performed with a classical tuned coil with a quality factor Q around 100 at 300 kHz and then with a mixed sensor coupled with a tuned flux transformer with a quality factor Q around 20 at 300 kHz.

With the tuned coil, a cylinder ($\varnothing = 6$ cm) in teflon with several holes of different size and depth is imaged. It is filled with the same doped water as before (T_1 and T_2 close from 50 ms) and acquired with a spin echo sequence.

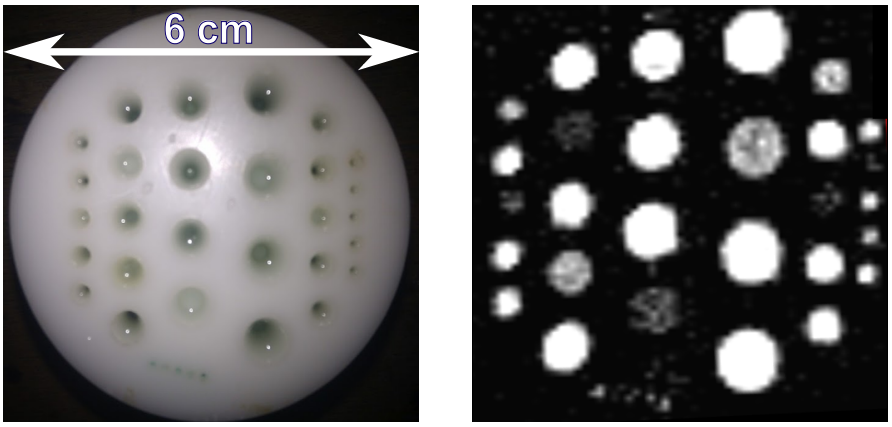

(a) (b)

Figure 5.5: a) Doped water phantom and b) its two dimensional MRI image

Our K-space is composed of 64x64 points to reach a 1mm resolution. The total acquisition time is 60 min for 100 averages of each point. On this particular sample no intensities variation can be seen on the edge (due to inhomogeneous excitations). The total signal-to-noise ratio is the mean amplitude of all regions of interest divided by the mean amplitude of all regions with no signal (only noise). We measure a signal-to-noise ratio around 98. All filled asperities present a signal higher than our noise floor.

With the mixed sensor, a polygon with seven holes of different size and dept is imaged. It is filled again with water doped with Copper Sulfate and acquired with a spin echo sequence.

(a) (b)

Figure 5.6: MRI acquisition in 2 dimensions (X,Z)

No gradients or pulses influence is detected on the sensor or on the flux transformer. Our K-space is composed of 32 x 32 points to reach a 2 mm resolution. The total acquisition time is 60 min for 100 averages of each point. We measure a signal-to-noise ratio around 40.

The main difference in signal-to-noise ratio comes from the position of the pickup coil which is more distant from the sample (we lose a factor 10 in signal) and the shielding of the cryogenic dewar (we lose a factor 1.6).

5.1.4 *Susceptibility artifacts and metallic implants*

In clinical MRI, metallic implants or metallic needle (for image-guided biopsy) raises some important issues. First of all, they are subject to the Lorentz force due to magnetic fields that can cause some damages to the patient by small displacements [30]. Moreover, radio frequency pulses and detected radio frequency NMR signal induce eddy currents in the metal that generates magnetic screening fields and can locally heat tissues and degrade them. Finally, the susceptibility difference between the metal and the surrounding tissue causes a local magnetic inhomogeneity. It induces a local dephasing and an image distortion along the frequency-encoding direction [40].

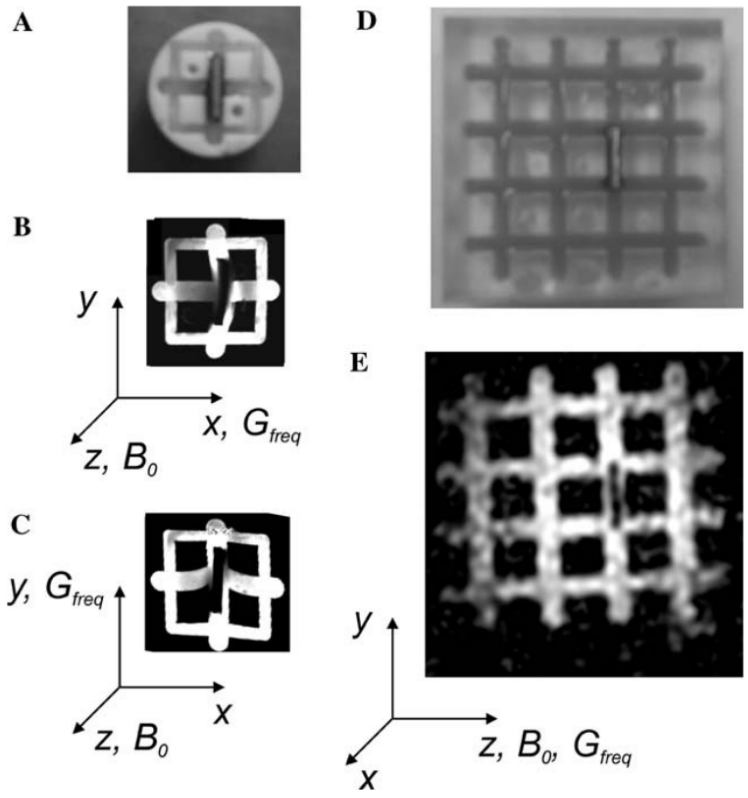

Figure 5.7: Images of water phantoms containing a 1.5 x 10 x 15 mm bar of titanium. (A and D) Photographs of phantoms. (B and C) Images acquired at 7T and a readout-gradient of 40 mT/m with the bar oriented perpendicular and parallel to the frequency encoding direction, respectively. (E) Image acquired at a 132 μT measurement field with a readout-gradient of 110 $\mu T/m$. [40]

As we can see in Figure 5.7, at ultra low field issues are different due to the intrinsic differences in field amplitude. Therefore susceptibility artifacts and RF screening are going to be measured in the small MRI setup at 10 mT to compare the results. We know that the maximum spatial distortion Δx due to a susceptibility change $\delta\chi$ can be expressed as

$$\Delta x = \Delta\chi B_0 / G_R$$

where G_R is the frequency encoding gradient and B_0 the permanent magnet field. A phantom composed of a square grid is acquired at 8 mT. This acquisition is repeated with small pieces of titanium placed inside the grid. We choose to test this material as it is often use for implants because of its biocompatibility and its mechanical properties.

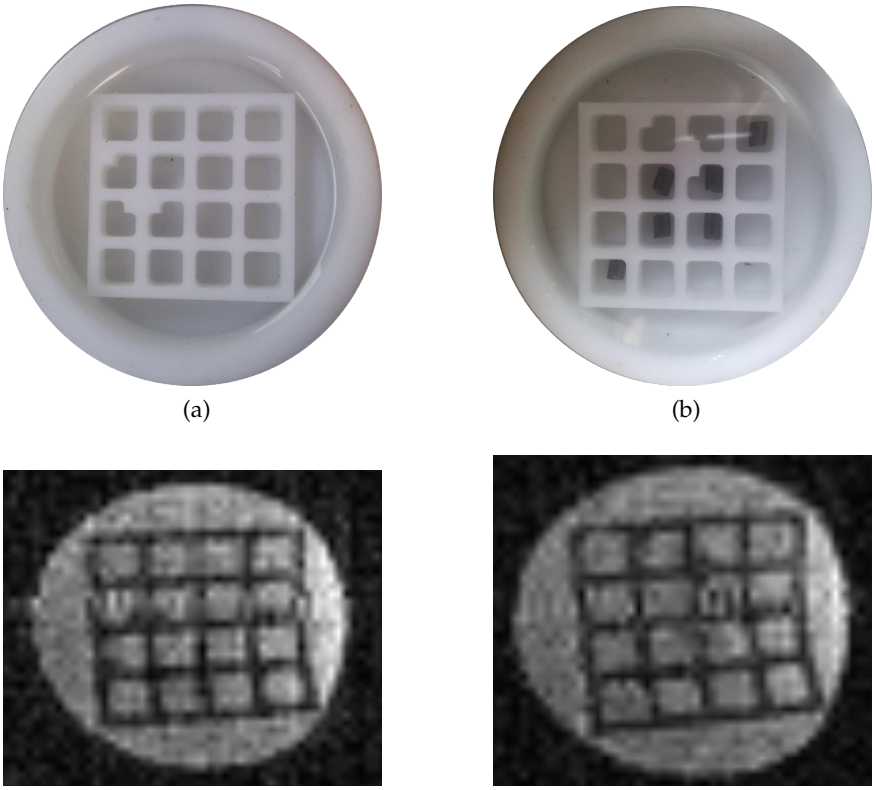

(a) (b)

(c) (d)

Figure 5.8: a) and b) are photographs of both phantoms filled with doped water (T_1 and T_2 around 50 ms). c) and d) are the resulting 2D images.

A gradient of 0.4 mT/m has been applied in both direction. Figure 5.8 shows no new distortion with or without titanium. It is in agreement with the theory which predict a distortion 10 times smaller than in Figure 5.7.

Another acquisition is then performed through a beverage can to estimate the radiofrequency screening at this frequency (see Figure 5.9).

Figure 5.9: Teflon phantom in an aluminum can.

At 170 kHz (4 mT), it is impossible to recover any NMR signal from our phantom. The screening of the can is too important to allow any MRI acquisition. Moreover, a change in the resonance frequency is observed in the tuned coil when the can is added which complicate the experiment. It should be noticed that the same experiment at 66 μT has been performed by Mössle et al. [40] with successful results (see Figure 5.10).

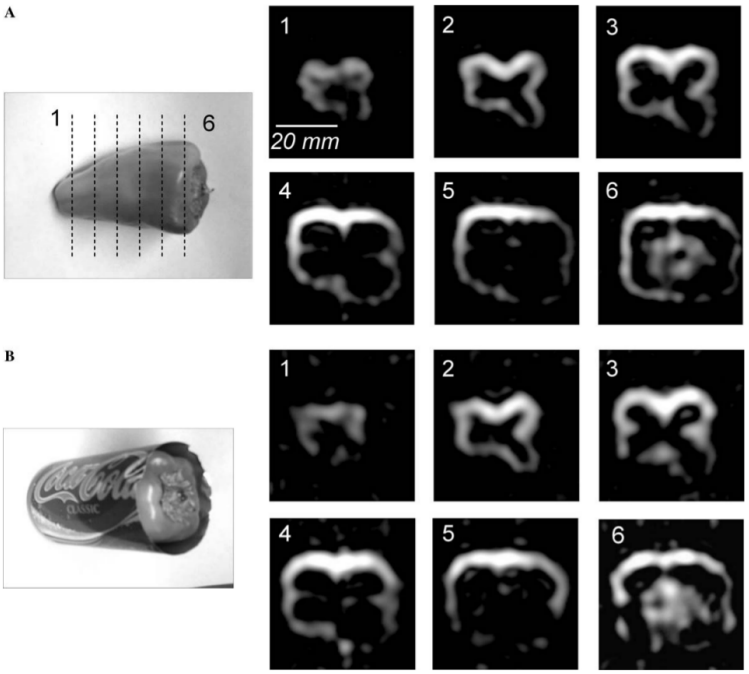

Figure 5.10: (A) Three-dimensional image of bell pepper showing six cross sections with a thickness of 8 mm; the lines in the photograph mark the position of each slice. (B) Six cross sections of the same pepper enclosed in an aluminum can. In each case, B_0 = 66 μT and G_{freq} = 57 $\mu T/m$.[40]

In conclusion, metallic implants have a negligible influence on distortion in very low field MRI. Some screening issues can exist even below 200 kHz and introduce some artifacts but in a minor way in comparison to high field MRI. Finally, all displacements and heating safety issues are greatly reduced by using smaller magnetic field.

5.1.5 *In-vivo imaging*

In-vivo tissues are complex structures that require a good resolution and three dimensional imaging or slice imaging. Indeed any part of the human body projected on a plan would not bring any relevant information. Three dimensional imaging at very low field MRI is time consuming and in-vivo measurements need to be fast to be comfortable for patients and to avoid any displacements. The acquisition of one slice of an index finger was performed in the small MRI setup. A specific cylindrical tuned coil was designed to fit around a finger (l = 3 cm and Ø = 2 cm). A 2 mm slice is acquired with a field-of-view of 2048 points x 32 points at 7mT with pixels of 1 mm x 1 mm. Each point is averaged 50 times for a total acquisition time of 15 min. The relaxation times are around 40 and 150 ms for T_2 and T_1(see Section 5.2). A slice selection spin echo sequence is applied with a selective cardinal sinus pulse of 8 ms, an echo time of 50 ms and a repetition time of 500 ms.

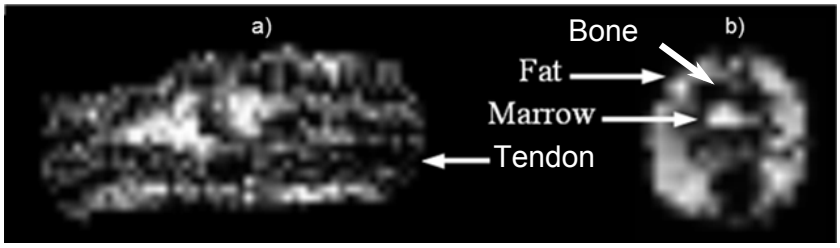

Figure 5.11: a) Sagital and b) axial slice of a finger at 7 mT

The signal-to-noise ratio of this image is around 40 and it is possible to distinguish bone, marrow and fat. The measured noise was not increasing with or without the finger inside the coil which is coherent with our predictions. This very low field setup is compatible with in-vivo imaging on a small body part with reasonable acquisition time.

5.2 RELAXOMETRY

As shown in Chapter 1, very low field MRI presents original characteristics concerning spin relaxation in comparison to classic MRI. The influence of molecular dynamic processes on T_1 and T_2 at such frequencies could have interesting consequences on medical field and security field. Multi spin echo and inversion recovery sequences have been introduced in both setups in order to achieve precise measurements of longitudinal and transverse relaxation. Examples of phantom mapping are presented. Then relaxometry measurements are performed on four different products with known relaxometry behavior to test our system. Finally, in-vivo measurements are performed on a finger. All those experiments have been performed in the small MRI setup.

5.2.1 *Definition*

The relaxometry can be defined as the study of magnetic resonance relaxation. According to its chemical composition, a sample will present a specific longitudinal and transverse relaxation time called respectively T_1 and T_2 (see Chapter 1). A precise analysis of those parameters present several advantages. First, those relaxation times can be used as parameters for liquid characterization. A defined product will present a certain value of T_1 and T_2 that can be measured quickly. Based on those observations, low field devices could be used as effective transportable detection devices [20].

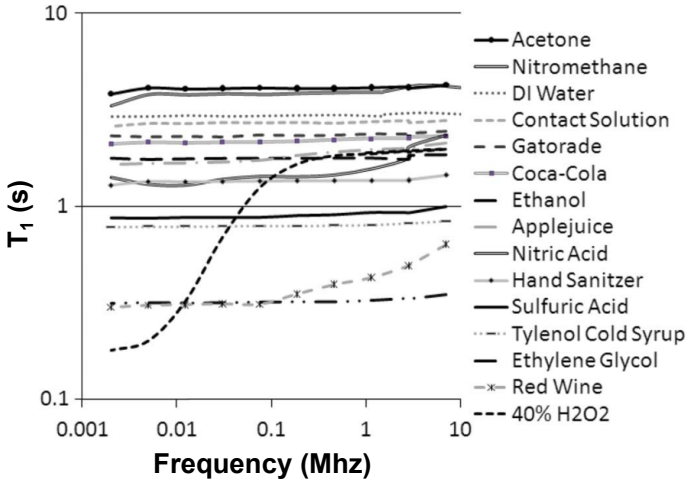

Figure 5.12: T_1(s) vs frequency (Mhz) from $\sim$ 1 kHz to 10 MHz for various assumed threats and items from streams of commerce[20].

Moreover, MRI images can be weighted in T_1, in T_2 or in proton density. This weighting can be chosen by programming a sequence with well defined parameters like repetition time (TR) or echo time

(TE) in agreement with the targeted sample relaxation times. Then a relevant sequence programming call for a precise knowledge of T_1 and T_2. That's especially true at very low field where contrast to noise ratio is significant.

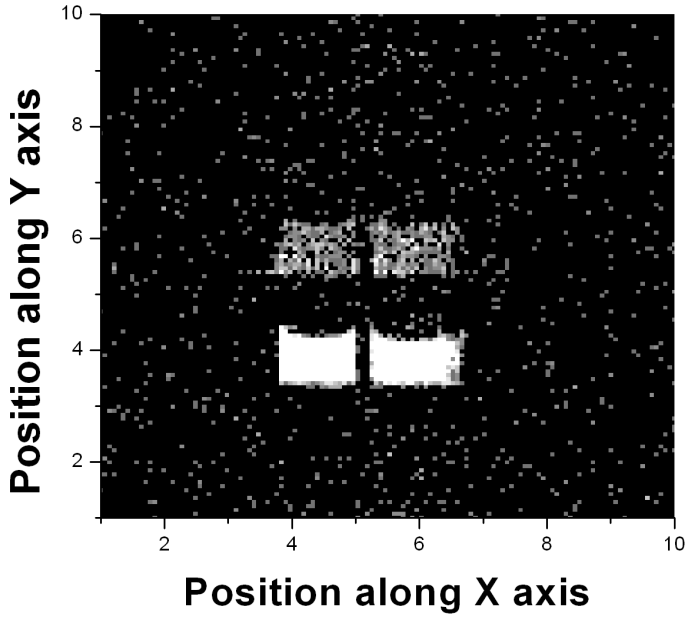

Figure 5.13: Two top samples filled with distilled water (T_1 and T_2 around 3 s) and two bottom samples filled with water doped with Copper Sulfate (T_1 and T_2 around 50 ms). A two dimensional T_1-weighted image is obtained with TE = 50 ms and TR = 500 ms. Bottom samples present a strong signal (in white) and top samples a low signal (in grey).

Different tissues and liquids will be studied between 1 mT and 10 mT to establish a basic table of T_1 and T_2.

5.2.2 *Multi spin echo sequence*

In a perfectly homogeneous magnetic field, the transverse relaxation time can be straightly measured on the free induction decay as it is described by

$$M_{xy}(t) = M_{xy,0}(e^{-t/T_2})$$

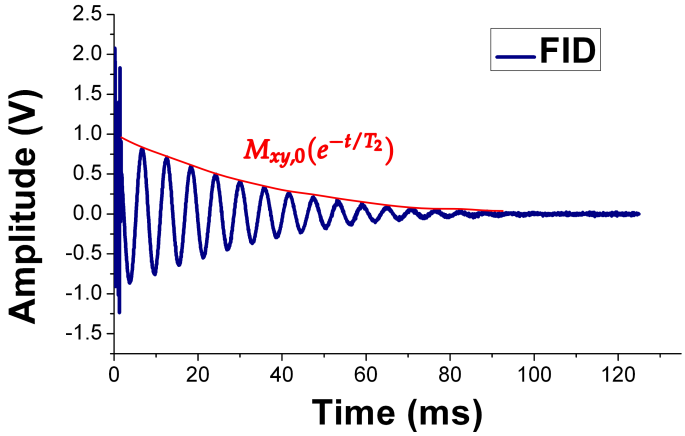

Figure 5.14: T_2 measurement on a FID signal in homogeneous environment.

However, this solution supposes perfect measurement conditions and excludes imaging possibility. Another interesting option is to use a multi spin echo sequence. It is identical to a single spin echo sequence but instead of one refocusing pulse, we apply N refocusing pulses.

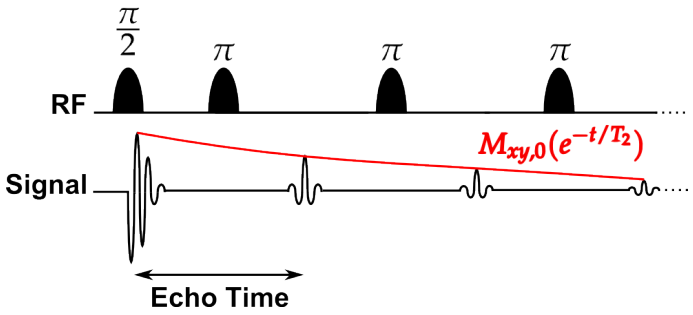

Figure 5.15: Multi spin echo sequence and corresponding $M_{x,y}$ decay

During echoes, the phase shift between spins due to permanent external inhomogeneity is canceled. The obtained signal has an amplitude which corresponds to the true T_2 relaxation. That way it becomes possible to reconstruct the intrinsic decoherence of the sample and thus access to its T_2 . This sequence is practical as it works in inhomogeneous environment and it is compatible with gradient encoding. It becomes then possible to realize one image with each echo. The evolution of its amplitude through each echo is relative to T_2. An exponential decay fit applied on each voxel will thus lead to a pure T_2 map. It is a useful method to discriminate tissues for in-vivo experiments.

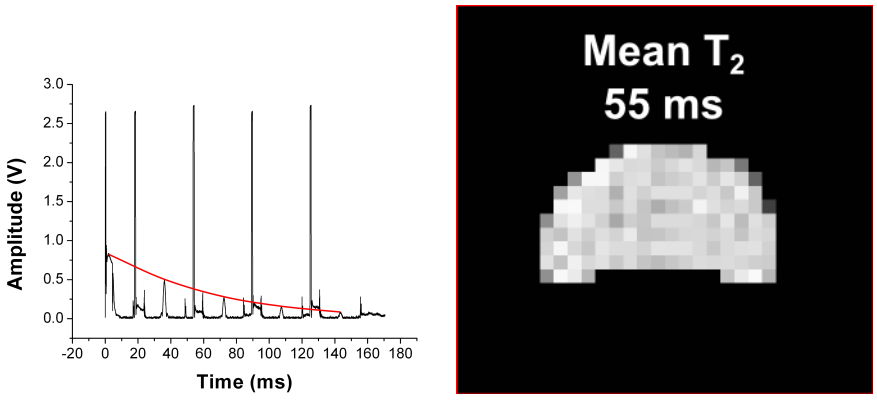

(a) (b)

Figure 5.16: a) Classic multi spin echo sequence on a sample doped with copper sulfate and b) its T_2 map after an exponential decay fit

5.2.3 *Inversion Recovery sequence*

Another important parameter in relaxometry is the longitudinal relaxation time T_1. Its measurement is more difficult as the sensor is oriented to measure transverse signal only. However a specific sequence called Inversion Recovery allows a precise measure of this longitudinal component relaxation described by

$$M_z(t) = M_{z,0}(1 - 2e^{-t/T_1})$$

A classic spin echo sequence is again used however an inversion pulse π precedes it. After this first "inversion" pulse, the magnetic moment will relax longitudinally during a time T_i called the "inversion time". Thus the amplitude of the signal after the classic spin echo part will be related to this "inversion time" and the T_1 of the sample.

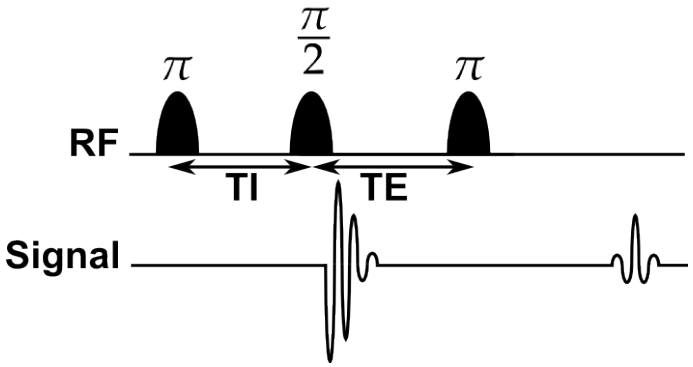

Figure 5.17: Inversion recovery sequence

Like for a multi echo sequence, it is compatible with the gradient encoding and the inhomogeneous environment. The evolution of the amplitude is described in Figure 5.18

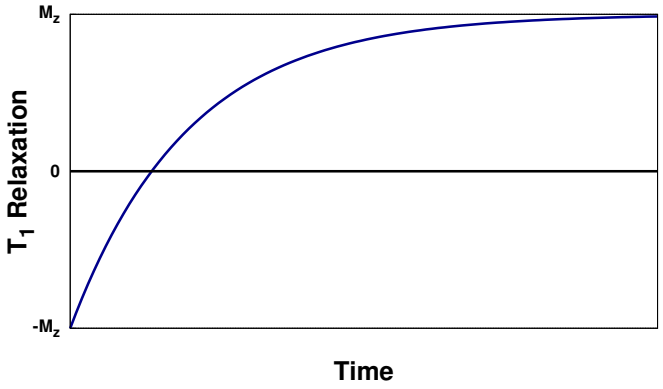

Figure 5.18: Relaxation of the longitudinal component of the magnetic moment after the inversion pulse

Practically, a pure T_1 map requires several three dimensional images which have been acquired at different T_i . Then all voxels see their amplitude fitted with the relaxation equation. It has to be noticed than an amplitude measured is always positive. It is the phase of the signal which indicates us if the magnetic moment is still reversed or not.

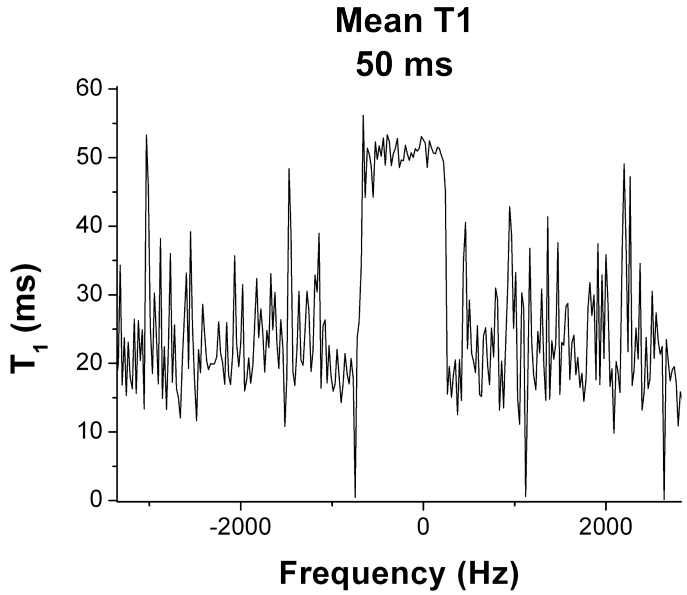

Figure 5.19: One dimensional T_1 map of a homogeneous sample filled with water doped with Copper Sulfate. In the sample range (-750 Hz to 250 Hz), the calculated T_1 is around 50 ms. Outside, the T_1 is completely random and corresponds to the noise.

Like previously, this mapping is useful for all experiments where it becomes difficult to physically separate elements.

5.2.4 *Liquid relaxometry*

A study of several liquids relaxation time has been performed at 2.1 mT, 4 mT, 5.8 mT and 7.8 mT. All liquids have been measured at 293 K in a bottle of 30 cl. Agarose (0.25% and 0.50%), distilled water and H_2O_2(70%) have been chosen to perform those tests. They are relevant to test the robustness of the system as their relaxation times have already been studied at those frequencies [20][33]. Moreover, agarose samples are supposed to have a relaxation behavior close to in-vivo tissues and could then help to predict the suitability of very low field MRI. T_1 and T_2 were measured three times.

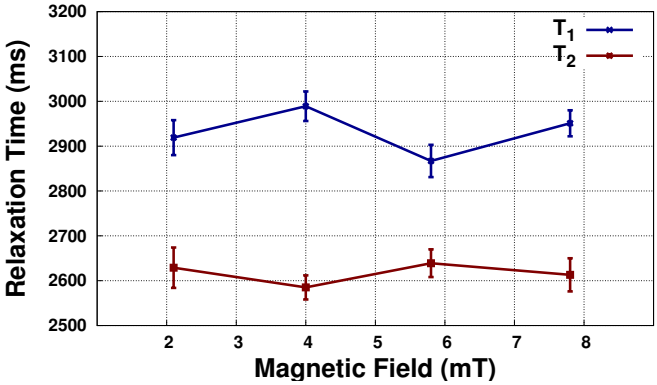

Figure 5.20: Relaxation time of distilled water between 2.1 mT and 7.8 mT

As expected, the relaxation time of the transverse and longitudinal relaxation of distilled water (see Figure 5.20) does not depend on the field. However, according to the Bloembergen-Purcell-Pound theory, T_1 and T_2 should be equal. This difference can be mainly explained by the ripple current noise coming from the static field supply which creates punctual magnetic perturbations. The T_2 is then artificially reduced and a better filtering circuit should be used to obtain accurate measurements. Short T_2 should be less impacted by this issue.

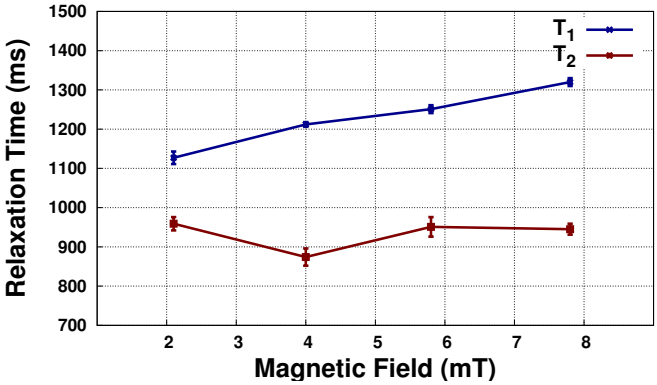

Figure 5.21: Relaxation time of hydrogen peroxide (70%) between 2.1 mT and 7.8 mT

With hydrogen peroxide (see Figure 5.21), T_2 is constant but we observe a decrease in T_1. This is consistent with previous results obtained by M. Espy et al. [20]. Finally for both agarose samples, results are plot on the experimental curve obtained by S. Lee et al. [33].

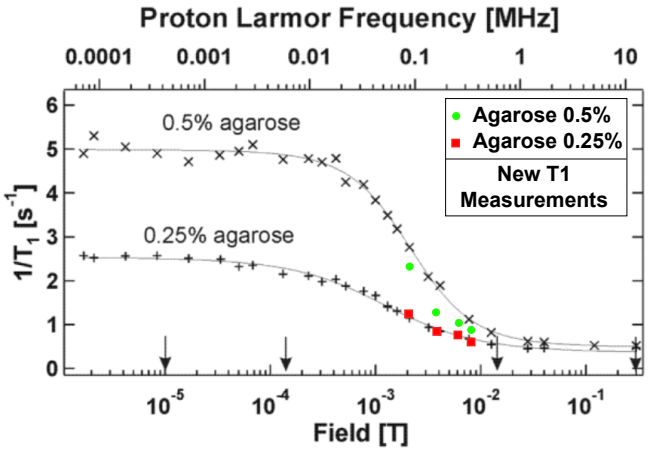

Figure 5.22: Relaxation rate dispersion of 0.25% and 0.5% agarose gel in water measured between 72 Hz and 12.8 MHz[33] and new measurements performed in the small MRI setup.

Figure 5.22 shows an identical behavior between S. Lee experiments and the small MRI setup results. The small difference with the Agarose at 0.5% could be mainly due to a difference in temperature which is supposed to be around 20 °C but has not been precisely controlled. From all those results, we can conclude that our relaxometry measurements are consistent with literature. Moreover, according to agarose samples very low field MRI is a perfect compromise to obtain a substantial difference in contrast without using any prepolarization field.

5.2.5 *In-vivo relaxometry*

For in-vivo relaxometry, a global T_1 and T_2 are first measured. No gradients are applied and then there is no spatial discrimination. The resulting relaxation time is a "mean" relaxation time of all tissues present in the body part we are looking at.

	Entire hand	Entire finger
T_1 (ms)	83 ± 5	122 ± 16
T_2 (ms)	47 ± 3	37 ± 1

Table 5.1: Mean relaxometry of an entire hand and an entire finger at 6.4 mT

Unlike homogeneous liquids, a three dimensional mapping is needed for a precise study of different tissues. A T_2 map in two dimensions

is performed on a finger on a 2 mm slice with a resolution of 1 mm x 1 mm. The total acquisition time of this relaxometry map is about 15 min.

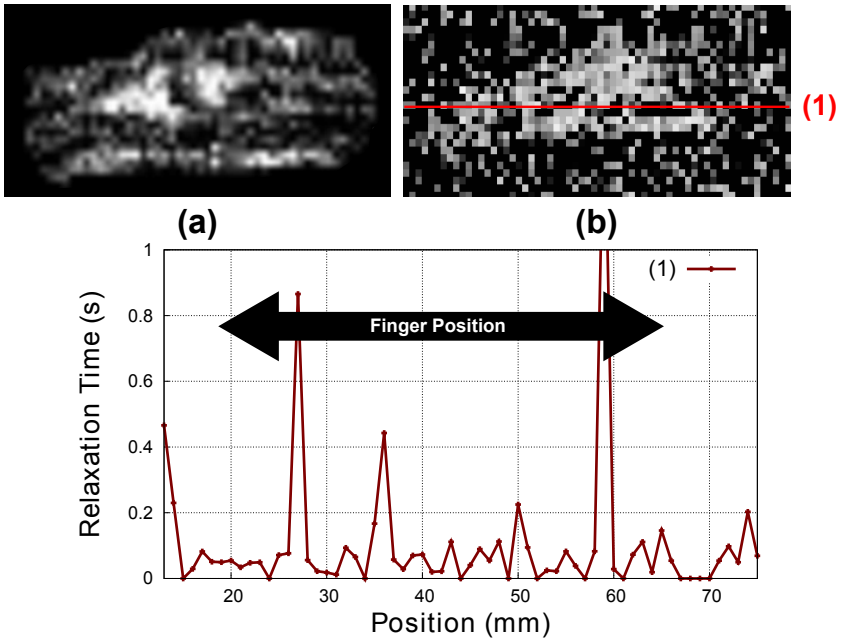

Figure 5.23: a) In-vivo 2 mm slice of a finger at 7 mT (1 mm x 1 mm) b) and its T_2 map in two dimensions and c) in one dimension (finger between 17 mm and 66 mm)

Due to a low signal-to-noise ratio, it is difficult to obtain a precise T_2 value with a resolution of 1 mm x 1 mm. However those preliminary results are in agreement with our previous measurements with a mean T_2 around 40 ms. A T_1 map in two dimensions is also performed on a finger on a 2 mm slice with a resolution of 1 mm x 2 mm. The total acquisition time of this relaxometry map is about 30 min with ten inversion recovery step.

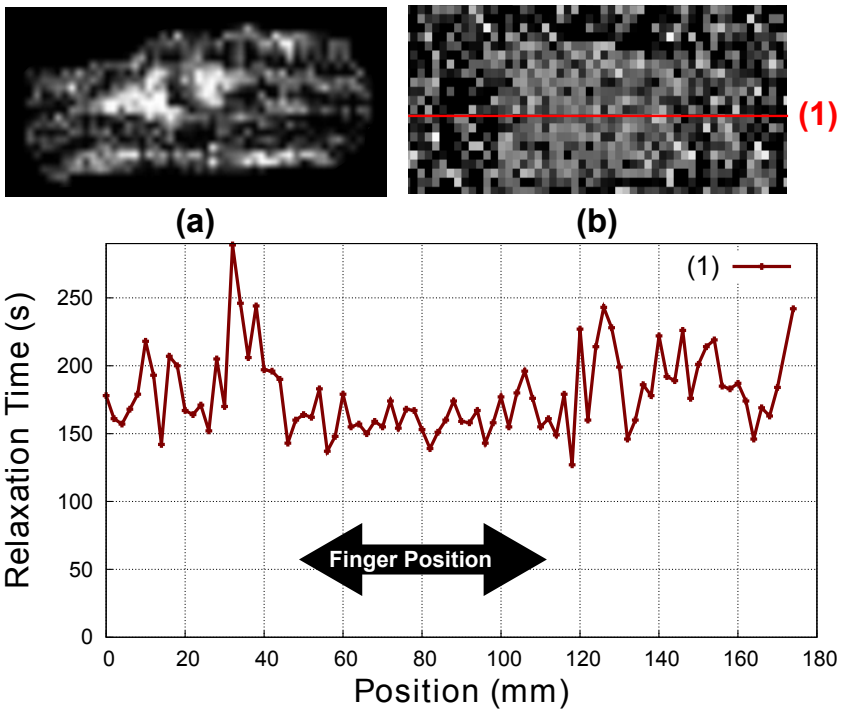

Figure 5.24: a) In-vivo 2 mm slice of a finger at 7 mT (1 mm x 1 mm) b) and its T_1 map in two dimension (1 mm x 2 mm) and c) in one dimension (finger between 50 mm and 110 mm)

For the longitudinal relaxation, we had to reduce the resolution to obtain a T_1 map in less than 30 min. The mean T_1 is measured around 150 ms. Both T_1 and T_2 in-vivo mapping works but it is difficult to distinguish tissues from each other in such a small appendix with the current signal-to-noise ratio.

CONCLUSION

Very low field MRI is compatible with classic imaging sequences. Spin echo sequences sequences have been incorporated for three dimensional imaging. A millimetric resolution with a reasonable signal-to-noise ratio is obtain after several hours of acquisition. Double phase encoding was used at first but the total acquisition time was not compatible with in-vivo imaging. Slice selection pulses have been designed to achieve a 2 mm resolution. They have been tested for in-vivo imaging on a finger with an in-plane resolution of 1 mm x 1 mm. The signal-to-noise ratio after 15 min of acquisition is sufficient to distinguish bones, fat, tendon and marrow. The impact of metallic implants has been evaluated. The susceptibility artifacts with titanium is measured as negligible. However the screening effect of an aluminum can has completely destroyed our signal in the frequency range where we operate. A mixed sensor combined with a tuned flux transformer has also been tested to see if the use of gradients could degrade its de-

tectivity. A two dimensional image was obtained but working in this configuration is not ideal as the cryogenic dewar is filtering the signal and the geometry does not offer as much filling factor as tuned coils.

Multi spin echo and inversion recovery sequences has been incorporated and tested on several products for relaxometry studies. The results with distilled water, hydrogen peroxide and agarose is close from literature values. However an undesirable effect of the ripple current noise is observed for T_2 measurements. For long transverse relaxation (distilled water for example), we have underestimated the value. A better filtering circuit should be designed to obtain correct values. As predicted by previous papers, the agarose samples at 0.25% and 0.5% possess two distinct T_1 in this range of frequencies. As their behavior is close from in-vivo tissues, new biological contrasts could be measured at very low field. Finally, relaxometry maps have been acquired in-vivo on a finger. The result does not allow any local measurement but give the average T_1 and T_2 values.

6

SPEEDING UP ACQUISITION TIME

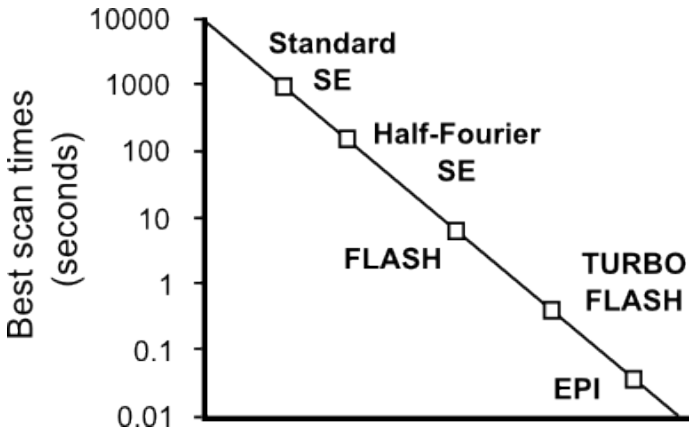

Scan time of different sequences : Standard Spin Echo, Half-Fourier Spin Echo,

Fast Low Angle SHot, Turbo Fast Low Angle SHot and Echo Planar Imaging.

Very low field MRI is inherently limited in signal-to-noise ratio and thus requires important averaging time to obtain good quality images. In addition the sample's polarization and the sensor's detectivity, MRI sequences have a major impact on the acquisition efficiency. Spin echo and Gradient echo, that we use in this manuscript,

are not used anymore for high field diagnosis as much more powerful methods exist. Through the study of Fast Low Angle SHot and Echo Planar Imaging, we will evaluate the impact of such approaches at very low field in term of signal-to-noise ratio and acquisition time.

6.1 FLASH FOR VERY LOW FIELD MRI

There are different kinds of sequences to accelerate MRI acquisition. In this section, Fast Low Angle SHoT sequence is going to be presented. The principle has to be defined from very low field point of view. Indeed, unlike high field MRI, we cannot trade signal-to-noise ratio (which is already weak) to speed up the total acquisition time. The signal-to-noise ratio per acquisition time is going to be defined to measure the efficiency of FLASH. Two things should be pointed out. First, FLASH should be demonstrated to be compatible at very low field and more efficient than classic sequences like spin echo or gradient echo. Then, the advantages should be compared to high field to evaluate intrinsic sequences limits of very low field MRI. To do so, a simulation is performed first, to predict the signal-to-noise ratio per acquisition time in both configurations. Finally, a one dimensional image will be acquired using classic gradient echo imaging and FLASH imaging with different angles.

6.1.1 *Definition*

Fast Low Angle SHot sequence is one measuring technique for rapid MRI invented in 1985 [24]. The principle is to combine a low-flip angle excitation with the acquisition of a gradient echo which allows a rapid repetition of the basic sequence interval. That way, the entire image acquisition is much faster.

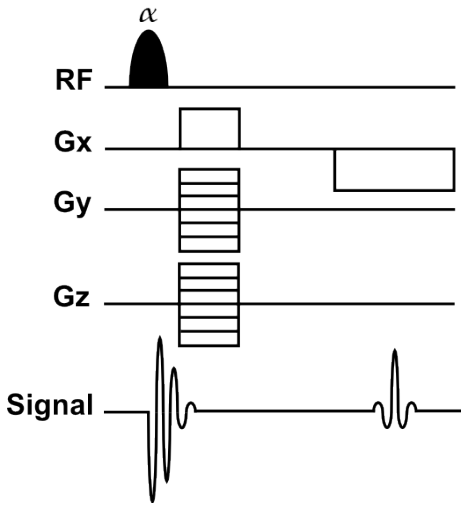

Figure 6.1: FLASH sequence for three dimensional imaging

The magnetic moment is tipped down by an angle α. It reduces its longitudinal magnetization by only $1 - cos(\alpha)$. Moreover, the use of a gradient echo excluded any refocusing pulses that would affect the residual longitudinal magnetization. A steady state is reached when the polarization restored during TR matches the saturation created by α. Using this method, high field MRI measuring times have been shortened up to two orders of magnitude [24]. Repetition times were reduced from 1 second to 10 milliseconds. It should be noticed that the speed of a FLASH sequence is limited by the space encoding time. All time requirements for slice selection, phase encoding and frequency encoding increase the minimum TR value we can use. Usually, the NMR linewidth δf of the sample defines the minimum required readout gradient strength. Then the acquisition time T_a for one K-space point is expressed as

$$T_a = \frac{1}{\delta f}$$

This value is typically around 5 millisecond at high field. Due to a much better absolute homogeneity, very low field MRI requires weaker gradients and then the typical acquisition time is around 50 millisecond. The slice selection and phase encoding time are also dependent of the gradient strength and then usually they are 10 times longer at very low field. Then the use of regular gradients to perform FLASH sequences would lead to a direct acceleration of our acquisition time up to a factor 10.

6.1.2 *Very low field specificity*

At very low field, the acquisition time is an important parameter that should be minimized. However, it can not be shorten by trading signal-to-noise ratio which is a rare resource at such frequency. It is then important to quantify the trade between the acquisition time and the signal to noise ratio that occurs for FLASH sequences. A particular attention should be paid to what we call "the signal-to-noise ratio per unit acquisition time". A classic gradient echo sequence is compared to a FLASH sequence on the same time period in terms of signal-to-noise ratio. When the steady state of a FLASH sequence is reached, the signal after the excitation is given by the Ernst equation [19] :

$$S_{FLASH} = A\ sin(\alpha)\frac{1 - exp(-TR/T_1)}{1 - cos(\alpha)\ exp(-TR/T_1)}$$

where A is the signal amplitude during the gradient echo for a 90° tip down of a full magnetization. The maximum signal is observed at the Ernst angle α_E such as

$$cos(\alpha_E) = exp(-TR/T_1)$$

During a classical gradient echo sequence, the entire longitudinal magnetization is used ($S_{CLASSIC} = A$). If we compare both signal intensities, we obtain

$$\frac{S_{FLASH}}{S_{CLASSIC}} = sin(\alpha_E)\frac{1 - exp(-TR/T_1)}{1 - cos(\alpha_E)\ exp(-TR/T_1)}$$

However, a shorter repetition time authorize more averaging. If we suppose that 5 T_1 is the necessary repetition time to recover the entire longitudinal magnetization, the signal-to-noise ratio between both sequences becomes

$$\frac{SNR_{FLASH}}{SNR_{CLASSIC}} = sin(\alpha_E)\frac{1 - exp(-TR/T_1)}{1 - cos(\alpha_E)\ exp(-TR/T_1)}\sqrt{\frac{5T_1}{TR}}$$

For several values of T_1, Figure 6.2 shows the evolution of this ratio according to the repetition time.

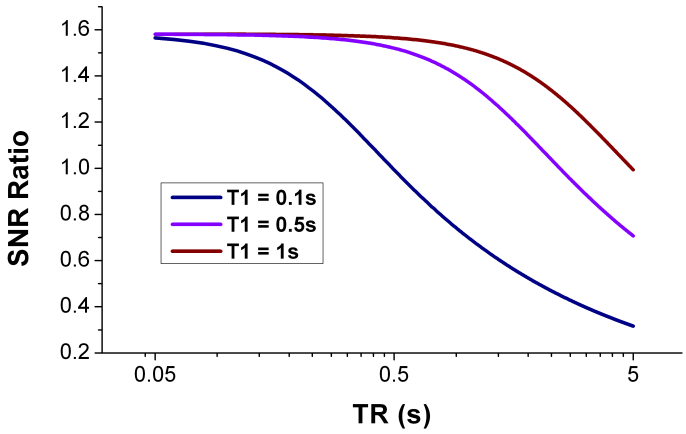

Figure 6.2: Signal to noise ratio between a FLASH sequence and a classical sequence for different repetition time.

The signal-to-noise ratio gain is limited and reached a maximum. Then decreasing the repetition time becomes ineffective. This reduction limit is linked to the T_1 relaxation time of the observed tissue. It should be noticed that the contrast obtained strongly depends on the Ernst angle we choose as we can see on Figure 6.3.

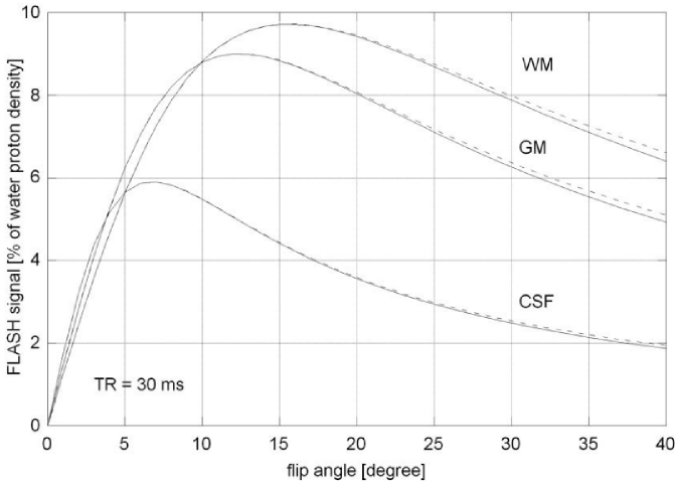

Figure 6.3: Simulated flip angle dependence for TR = 30 ms in White Matter, Grey Matter and Cerebrospinal Fluid using experimentally determined values of T_1 at 3T. Bold curves depict the exact Ernst equation, dashed curves the approximation of Ernst equation.[25]

Moreover, FLASH sequence doesn't use any 180° pulse which implies shorter echo time than for classic spin echo sequence. As a result, the T_2 effects are minimized. Also this lack of refocusing pulses implies a contamination of T_2 by external inhomogeneity. Therefore, it is really difficult to perform T_2 - weighted imaging with FLASH. The use of this sequence is excluded for many pathologies diagnosis like multiple sclerosis or cystic lesions. However this domination of T_2* on the weighting has also its advantage for some clinical diagnostic protocols [54].

6.1.3 *One dimensional FLASH*

A square phantom of 5 cm x 5 cm x 5 cm is imaged in one dimension with a 2 mm resolution along Z axis (see Figure 6.4). It is filled with tap water. The total acquisition time is fixed at 15 min for all images.

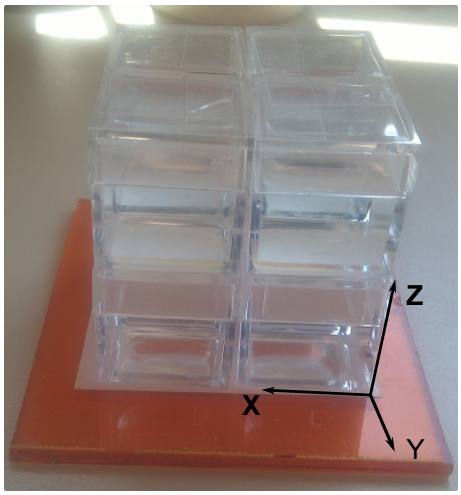

Figure 6.4: Square phantom of 5 cm x 5 cm x 5 cm filled with tap water

First, a gradient echo imaging is performed with a relaxation time between each pulse of 5 seconds. Indeed, the T_1 of this tap water is close from 1 second so 5 seconds corresponds to an entire relaxation of T_1 and T_2 for the sample. For such repetition time, the optimal Ernst angle is 90°. Then another image is obtained but with a repetition time of 15 seconds between each 90° pulse to confirm the inefficiency of this method. Finally, two images are acquired with a repetition time of 1 second and 0.5 second. They respectively correspond to an optimal Ernst angle of 68° and 52° . The signal-to-noise ratio of each image is then calculated and normalized by the signal-to-noise ratio corresponding to the usual sequence (TR = 5 seconds). All results are combined in Figure 6.5 and compared to the theoretical curve.

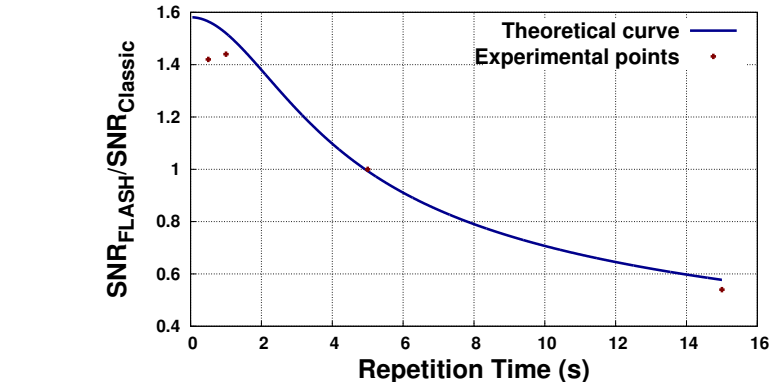

(a)

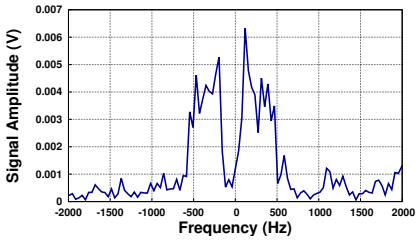

(b)

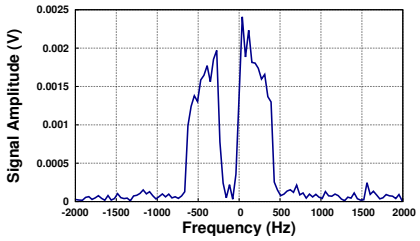

(c)

Figure 6.5: a) Experimental signal-to-noise ratio of Fast Low Angle SHot sequences with different repetition time and b) the resulting image for TR = 5 seconds and c) TR = 0.5 second.

The experimental points are close from the theoretical curve. The signal-to-noise ratio per acquisition time has been increased by a factor 1.4. For this sample, we reach the maximum efficiency before being limited by the intrinsic limit of the sequence (the time needed to acquire the signal). However, according to the simulation, it would be more difficult to reach the optimal repetition time with in-vivo tissues which have shorter T_1. The use of stronger gradients to reduce the intrinsic limit of our repetition time would lead to a worse signal-to-noise ratio (see Figure 6.6)

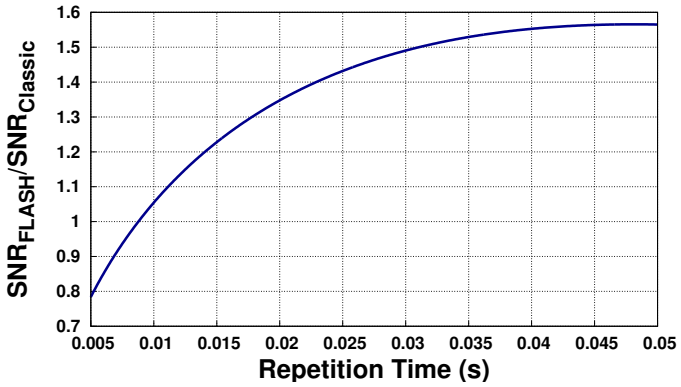

Figure 6.6: Signal-to-noise ratio of a Fast Low Angle SHot sequence below the intrinsic repetition time limit. The use of stronger gradients degrade the efficiency of the sequence. The product chosen for the simulation has a T_1 of 100 ms and a T_2 of 100 ms.

Finally, the gain in signal-to-noise ratio per acquisition time is substantial with Fast Low Angle SHot method. This sequence has been first designed to speed up the acquisition time, trading signal-to-noise ratio against rapidity. This trade is not well adapted with very low field requirements however it remains fully compatible with very low field MRI as long as the repetition time remains higher than the readout time.

6.2 SPIRAL ACQUISITION

6.2.1 *Principle*

Echo Planar Imaging (EPI) has been proposed by Peter Mansfield in 1977 [38]. It belongs to the family sequence that uses the repetition time waiting to acquire multiple lines of the K-space. A rapidly oscillating gradient is applied along the frequency encoding direction. For each reversal of the readout gradient from positive to negative, another gradient is applied along the phase encoding direction. Multiple gradient echo are then obtained and they are independently phase encoded.

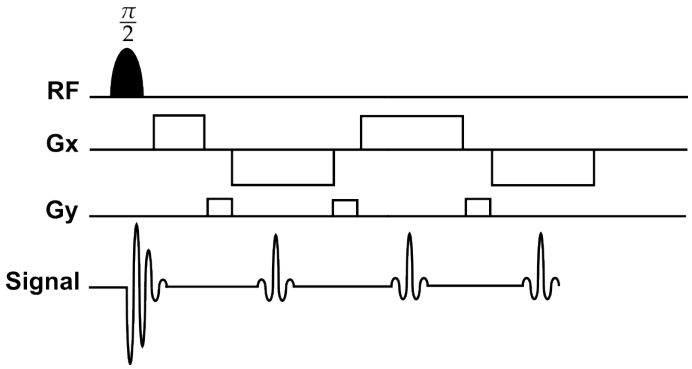

Figure 6.7: Echo Planar Imaging Sequence

At high field, an echo planar imaging can acquire the entire K-space in one shot. This technique collects data in a markedly different way than standard pulse sequence. The K-space is scanned linearly or not, depending on the gradients. Some exemples are presented in Figure 6.8.

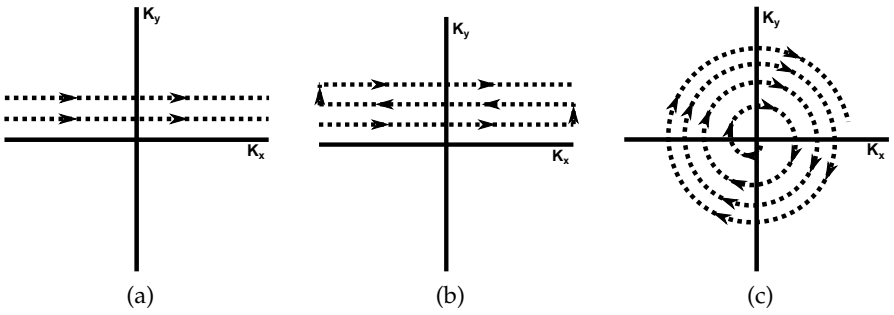

Figure 6.8: K-space scan for a) a classic gradient echo or spin echo sequence, b) an echo planar imaging in zig zag and c) an echo planar imaging in spiral.

At high field, EPI uses strong gradients (15-25 mT/m) with very small rise and fall time (0.1-0.3 ms). This important slew rate imposes good eddy current compensation to minimize image artifacts

and some acoustic noise protections. As for Fast Low Angle SHot sequence, the idea behind Echo Planar Imaging is to optimize the acquisition process to achieve faster imaging.

6.2.2 *Very low field specificity*

Very low field MRI does not offer as much signal resources as high field. Then trading signal-to-noise ratio for temporal resolution is not a relevant option and Echo Planar Imaging is considered here in term of pure signal-to-noise ratio gain rather than acquisition time gain. Two specificities will influence Echo Planar Imaging :

- T_2^* are much longer at very low field due to a smaller absolute inhomogeneity of the permanent field. The decay of the signal is then slower allowing the acquisition of more K-space lines or the use of a smaller acquisition bandwidth.

- The gradients amplitude we are using are weaker, around 1 mT/m in usual conditions. We could use the Echo Planar Imaging sequence with low amplitude gradients to take advantage of its efficient K-space sampling without changing the acquisition bandwidth. . As shown in Figure 6.9, those gradients imply longer readout sequence. The signal becomes then strongly sensitive to T_2 and T_2^* decay. At high field, this filtering appears mainly for high spatial frequencies and results in a blurring along the phase encoding direction. At very low field, this filtering could concern also central frequencies, depending on the tissues we observe.

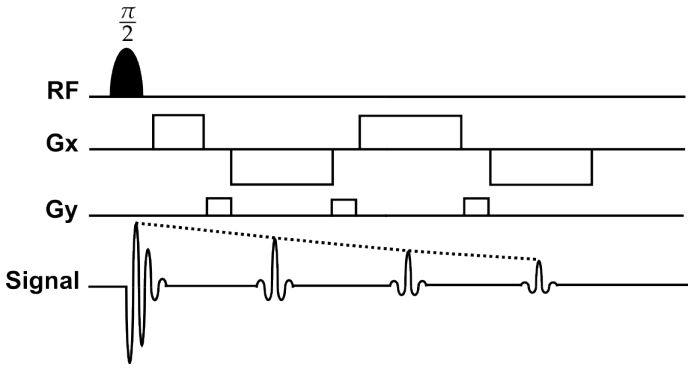

Figure 6.9: Echo Planar Imaging Sequence at very low field

A signal to noise ratio comparison between an Echo Planar Imaging using regular gradients and a gradient echo sequence is performed. To estimate the gain in signal-to-noise ratio, we compare one regular gradient echo sequence with a repetition time long enough to recover

the entire longitudinal magnetization ($TR \approx 5T_1$) to an echo planar imaging sequence with N gradient echos such as

$$N = floor[\frac{5T_1}{T_a}]$$

where T_a is the readout time. We will suppose here that external inhomogeneity are always dominating the transverse relaxation time ($T_2 \geq 50$ ms). For the classic gradient echo the signal S_{SE} measured is

$$S_{SE} = M_0 e^{-T_a/T_2^*}$$

where M_0 is the maximum longitudinal magnetization of the sample. For the Echo Planar Imaging, we consider that each gradient echo is a contribution to the total measured signal. Then we obtain

$$S_{EPI} = M_0 e^{-T_a/T_2^*} * \sum_{n=0}^{N} e^{-nT_a/T_2^*}$$

The noise is also increasing but in $\sqrt{N}$. The readout time T_a is related to the gradient strength we are using which impacts also the acquisition bandwidth BW. Here we use the smallest gradient strength to obtain a good signal-to-noise ratio such as $T_a = T_2^*$. For Echo Planar Imaging, we choose to compare its efficiency in signal-to-noise ratio per unit acquisition time according to the T_1. The T_2 has no influence as we are working in gradient echo imaging with a dominating T_2^*. The gain in signal to noise ratio per unit of acquisition time is expressed as

$$\frac{SNR_{EPI}}{SNR_{Classic}} = \sqrt{\frac{1}{N}} \sum_{n=0}^{N} e^{-n}$$

The result is plot in Figure 6.11 for different T_1 values.

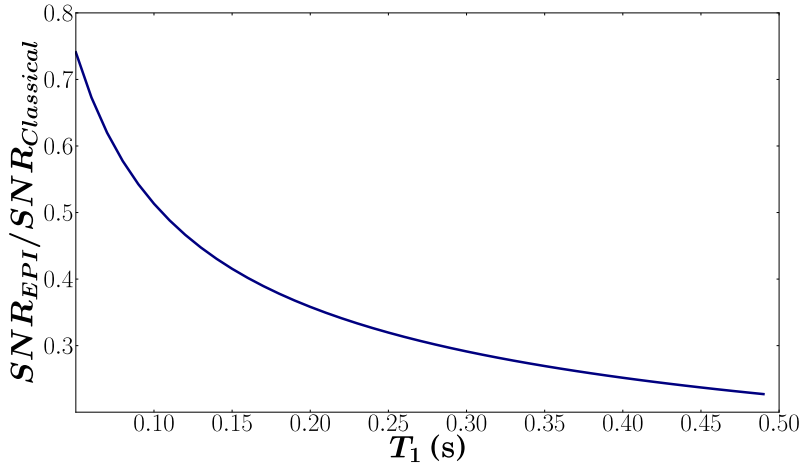

Figure 6.10: Gain in signal-to-noise ratio per acquisition time for different T_1

For all T_1, the signal-to-noise ratio per acquisition time measured with normal gradients is very low in comparison to classical gradient echo. It is mainly due to the fact that we add more noise than signal with such a long readout gradient. The use of stronger gradients associated with small readout time ($T_a \leq T_2^*$) should then be tested. The gain in signal to noise ratio per unit of acquisition time is expressed as

$$\frac{SNR_{EPI}}{SNR_{Classic}} = \frac{e^{-T_a/T_2^*}}{e^{-1}} \sqrt{\frac{Ta}{N * T_2^*}} \sum_{n=0}^{N} e^{-nT_a/T_2^*}$$

For a $T_1 = 150$ ms (e.g. longitudinal relaxation time in a finger at 7 mT), we simulate the gain in Figure 6.11.

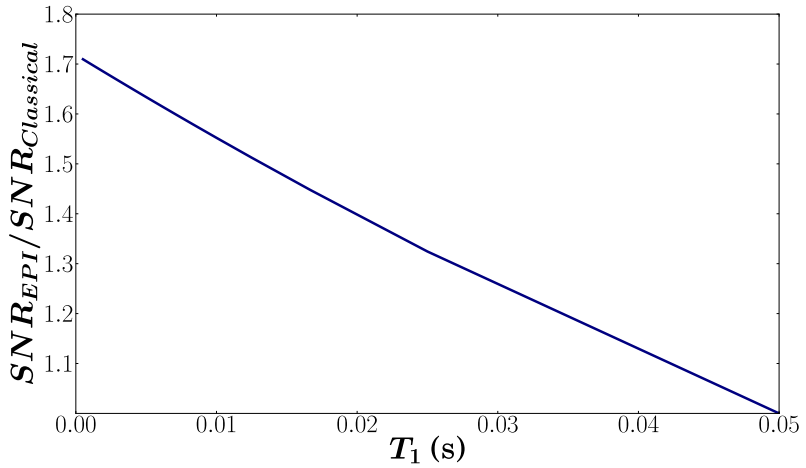

Figure 6.11: Gain in signal-to-noise ratio per acquisition time for different T_a combined with stronger gradients.

We see that despite the larger bandwidth, the gain is substantial for a gradient ten times stronger than the usual one (gain in signal-to-noise ratio ≈ 1.6). An image of a 10 cm sample would be acquired 2.5 times faster with the use of a 20 kHz gradient instead of a usual 2 kHz gradient. The problem with such strong gradients is that the detector should have a low quality factor to have a larger detection bandwidth. Nevertheless mixed sensors offer interesting detectivity level with large detection bandwidth and could then be fully compatible with the use of strong gradients. It should be noticed that this gain in signal-to-noise ratio will be smaller for tissues with very short T_2 (≤ 50 ms). Finally, an interesting point with Echo Planar Imaging at very low field is the T_2^* which is much longer than at high field. The gain in signal-to-noise ratio on tissues with long T_2 ($T_2 \geq 50$ ms) is potentially higher because we can exploit the signal during a longer time.

6.2.3 *EPI for 2 dimensional imaging*

Echo Planar Imaging sequence has been introduced in the homemade MRI program and a two dimensional imaging is being performed in the full-head MRI device. A square sample of 22 mm x 18 cm filled with doped water is measured with a 2 mm x 2 mm resolution at 3.3 mT (140 kHz). A gradient echo sequence is first used with a repetition time of 0.5 s and an echo time of 25 ms. Then an Echo Planar Imaging with two gradient echoes is applied with a repetition time of 0.5 s and an echo time of 12.5 ms. Both imaged have been acquired in 1 hour.

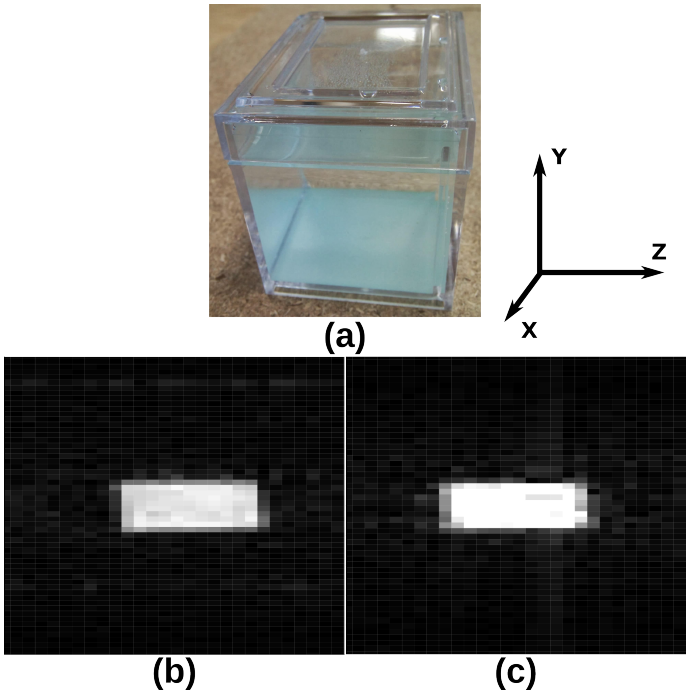

Figure 6.12: (a) Square sample filled with doped water imaged in two dimensions along X and Y with (b) a classic gradient echo sequence and (c) a echo planar imaging sequence.

The signal-to-noise ratio measured with the gradient echo sequence is around 26 and with the echo planar imaging sequence we are close to 41. The simulation was predicting a ratio of 1.32 between both methods and we measure a ratio of 1.58. The gain is low but still interesting. The ratio is higher than predicted as the signal is concentrated to the center of the K-space for a more efficient sampling method. For in-vivo imaging, the gain in signal-to-noise ratio could be higher as we will be less sensitive to flow and patient motions.

CONCLUSION

There is two conclusions to be drawn from fast sequence imaging at very low field. Both FLASH and EPI sequences bring an interesting

but limited gain in signal-to-noise ratio with a more efficient acquisition scheme. Indeed those sequences have been designed to trade efficiently spatial resolution for time resolution which is relevant at high field where the signal-to-noise ratio is higher than at very low field. In the actual development stage of very low field MRI, it might be too soon to trade the signal-to-noise ratio against speed and then their use is not totally appropriate. However, those sequences are compatible with very low field MRI to a certain extent. The use of 300 kHz gradients (typical gradient amplitude used for Ultra Fast Echo Planar Imaging at high field) for an NMR signal resonance at 140 kHz does not have any sense but smaller gradients (15 kHz) could be used to accelerate our total acquisition time by a factor 10 to 15. Indeed, a good detectivity (1.7 $fT/\sqrt{Hz}$) is offered by actual mixed sensors combined with tuned flux transformers with a quality factor corresponding to a detection bandwidth of 15 kHz. Moreover, the intrinsic high T_2^* of the very low field setup could be an important advantage for EPI with a signal less sensitive to permanent field inhomogeneities.

DISCUSSION

Magnetic Resonance Imaging quality depends on many parameters. Those parameters are very different for high field MRI and low field MRI. From every previous developments, we are going to compare the signal-to-noise ratio of a 1.5 T device and a 10 mT device for brain imaging:

- The signal at 1.5 T is 150 times greater due to a better polarization of the sample.
- The limiting noise at 1.5 T is the noise generated by the body which is around 0.1 $fT/\sqrt{Hz}$. The limiting noise at 10 mT is the noise generated by the sensor which is around 1 $fT/\sqrt{Hz}$.
- The detection bandwidth at 1.5 T is one hundred times larger than at 10 mT.

Finally, the signal-to-noise ratio between both MRI devices is

$$\frac{SNR_{1.5T}}{SNR_{10mT}} = \frac{150 * 10}{\sqrt{100}} = 150$$

A 1 mm x 1 mm x 1 mm resolution at 1.5 T would then correspond to a 4.2 mm x 4.2 mm x 4.2 mm at very low field. With an ultra low noise sensor ($\approx 0.01\ fT/\sqrt{Hz}$) , the difference in signal-to-noise ratio would be decreased to a factor 10, corresponding to a resolution of 2 mm x 2 mm x 2 mm at very low field. The use of fast sequences to optimize the signal acquisition can increase the signal-to-noise ratio by a factor 1.6. However, it is not yet relevant to use them to trade the spatial resolution against temporal resolution like it is usually the case at high field. However, the use of large gradients is compatible with very low field MRI and could lead to substantial reduction of the total acquisition time.

PERSPECTIVES

Through this study, the feasibility of very low field MRI has been proven. I will present here some future developments that could improve drastically the efficiency and the quality of very low field MRI.

Flux transformer

As it has been presented in Chapter 4.3, the best results were obtained using a tuned resistive flux transformer. In this configuration, the mixed sensor can be seen as a low noise pre-amplifier and the theoretical limit corresponds to the thermal noise of the flux transformer. This is also true for untuned resistive flux transformer but in this configuration the mixed sensor noise is not negligible and decreases our sensitivity. Based on this observation it appears that the detectivity of the sensor is not that important if it is combined with a tuned resistive flux transformer. The better the sensor is, the lower the quality factor can be (widening the working bandwidth) and for very sensitive sensor ($\lesssim 1\ fT/\sqrt{Hz}$), the flux transformer can be untuned. However, the signal to noise ratio will be exactly the same in all those configurations. Two solutions can be explored to go past this limit.

- First, the use of ferromagnetic core between the input coil and the superconducting loop could lead to a better coupling between both loops. As the input coil is the most resistive part of the flux transformer, it could be easier to obtain adequate coupling with less turns and thicker wires.
- Secondly, the use of niobium flux transformer would eliminate the limiting thermal noise. Using adapted cryogenic dewar, it could be a good solution to reach extremely good signal to noise ratio. However, the use of low temperature superconducting devices is never easy and it should be used only if the noise coming from the sensor is negligible compared to the thermal noise

of an equivalent resistive flux transformer ($\lesssim 0.2\ fT/\sqrt{Hz}$). Today, mixed sensors are not that sensitive and the use of a niobium wire should be relevant only for low frequency measurement that could be filtered with a resistive flux transformer.

- Finally, the use of a cryogenic dewar with a shape adapted to the measured sample with non-shielded super-isolation would lead to important gain in signal-to-noise ratio. For specific situations, a cryogenic dewar with sealed passage to let the pickup coil outside of the cryogenic dewar is also a solution. However the detectivity limit of such geometry will be difficult to overcome as it will be entirely defined by the thermal noise of the input coil.

Improved sensors

The improvement of the mixed sensor itself could also greatly ameliorate our results. The homemade YBaCuO sensors exhibit typically a factor 5 to 10 less low frequency noise than Sensitec sensors. However the superconducting loop was too fragile and it was not possible to perform experimental measurement on several days. A better control of the $YBa_2Cu_3O_7$ roughness of those sensors would allow us to integrate them in MRI experiments. Moreover, the use of tunnel magnetoresistance instead of giant magnetoresistance could lead to a better overall detectivity.

High Field MRI gradients

Very Low Field MRI authorizes the use of small gradients. As the absolute homogeneity of the system is much lower than at high fields, the acquisition bandwidth can be much smaller, increasing the signal-to-noise ratio as $\sqrt{BW}$. However, this short bandwidth induces long acquisition time which are limiting drastically the possibility of sequences. With such reduced gradients, some sequences were tested. The gain in signal-to-noise ratio is clear and is predicted to be even better for stronger gradients. It could then become interesting to work at very low field using larger gradients ($\approx$ 20 kHz).

Implement other complex sequence

Fast Low Angle SHot and Echo Planar Imaging have been tested already but MRI sequences are not reduce to those two solutions. First, cartesian acquisition of the K-space is not the only possibility offered by MRI. Spiral and radial K-space trajectory are other ways to acquire the signal which are more efficient (more points in the center where the contrast information stands) and more resistant to motion

and flow artifacts. Combined with Echo Planar Imaging, it could lead to a good improvement of image quality. Then sequences like Short TI Inversion Recovery (STIR) or Fluid Attenuated Inversion Recovery (FLAIR) could be used to enhanced the contrast to noise ratio of images depending on the observed tissues. FLAIR for example is widely used to suppress the cerebrospinal fluid (CSF) signal in the brain when STIR is more adapted to suppress fat signal. Both are entirely compatible with very low field requirements.

Sparse MRI and Compressed Sensing

Compressed sensing is based on the idea of undersampling the K-space[35]. With significantly fewer measurements than usual, images are reconstructed with little or no perceptible loss of information. This method is relevant because of two MRI properties :

- MRI is sampling encoded samples rather than direct pixel samples
- MRI images are naturally compressible by sparse coding in appropriate transform domain.

Compressed sensing has been extensively used to speed up the acquisition of tissues suffering from motion artifacts. For brain imaging, transform sparsity in the wavelength domain has been exhibited. Compressed sensing showed a significant resolution improvement over an equivalent linear reconstruction[36].

Parallel Imaging

The use of multiple detection coils is possible to accelerate the acquisition time of an image. An array of independent receiver channels is disposed in the phase encoding direction. Then each coil is measuring an undersampled version of the K-space in this phase encoding direction. The result is a combination of aliased imaged. Using a specific algorithm, it is then possible to reconstruct a correct image from the aliased images (SENSE) or reconstruct the missing K-space data combining all undersampled K-space (GRAPPA). Combined with fast imaging sequences, it reduces the number of echoes needed and most artifacts coming from T_2 and T_2^* decay. Its efficiency has been proven in many imaging scenarios where patient motions pose significant problems[47, 34]. It should be noticed that in an untuned flux transformer scenario, parallel imaging would be even easier at very low field than at high field due to reduced coupling issues.

CONCLUSION

A new approach of very low field MRI has been presented in this thesis. One small MRI setup has been optimized and characterized to perform in-vivo and in-vitro experiments on small volumes. One full-head setup has been built and adapted to perform in-vivo brain imaging. The detection was performed by the use of a superconducting loop combined with a Giant MagnetoResistance. This detection chain was combined with flux transformers of different types. Three dimensional imaging has been performed on several liquids and tissues as well as relaxometry studies. Finally, advanced sequences have been integrated to optimize very low field acquisition.

An existing small setup adapted for small volumes (5x5x5 cm^3) and a new full-head setup adapted for brain imaging (20x20x20 cm^3) have been used. With an open and transportable geometry, both designs offer a good homogeneity around respectively 10 ppm and 100 ppm on the defined working zone. The ripple noise of current supplies has been identified as the main source of inhomogeneity. Adapted gradient coils have been added to allow external inhomogeneity corrections (shimming) and three dimensional imaging. The amplitude of each gradient was 100 times lower than at high field but sufficiently high to achieve a resolution of 1 mm x 1 mm x 1 mm. Radiofrequency

coils have all been built with the same saddle coil model. The excitation homogeneity offered by this design was sufficient for all applications. Thanks to the use of appropriate filters, the noise generated by all supplies and metallic structures used in both setup was evaluated to be negligible in front of the sensor's noise.

Different mixed sensors have been characterized. All sensors were made of a Giant MagnetoResistance combined with a high-temperature superconducting loop ($YBa_2Cu_3O_{7-d}$). At a working temperature around 77 K, the measured detectivity was changing between 100 $ft/\sqrt{Hz}$ for sensors with a loop of 1 $cm^2$and 10 $ft/\sqrt{Hz}$ for homemade sensors with larger loop of 2.5 cm^2. All mixed sensor were built in a Wheatstone bridge configuration with four Giant MagnetoResistances, doubling the signal to noise ratio in comparison to a normal architecture involving one Giant MagnetoResistance. This design also suppresses any voltage drift coming from temperature changing. Mixed sensors have been introduced into an MRI experimental environment to put to the test its robustness. Its sensitivity was actually better inside the MRI device. No noise were added by current supplies and pulses were not blanking the sensor. Moreover the permanent magnetic field was linearising and centering the Giant MagnetoResistance response if disposed perpendicular to the hard layer. All mixed sensors were characterized in thermal noise regime between 42 kHz and 420 kHz (resonance frequency of protons between 1 mT and 10 mT). However, the use of those sensors to measure directly NMR signals raises important issues of coupling and filling factor. A NMR experiment was performed to illustrate those difficulties. Like for SQUIDs and Atomic Magnetometers, an intermediary device was needed to perform efficient MRI measurements.

Flux transformers have been used to increase the coupling between the mixed sensor and the measured sample. We have discussed the integration of superconducting, resistive and tuned flux transformers. Mounted inside the cryogenic environment, all three configurations were optimized and compared in term of detectivity for a given coupling coefficient between the input coil and the mixed sensor. We have evaluated the best geometry to obtain a maximum detectivity with such flux transformers. An original method to measure the coupling between the superconducting loop and the input coil has been presented. A concentric distributed input coil has given the best results. It has been shown that the mixed sensors size should be also dependent of the input coils size to obtain a perfect optimization. At high frequency ($\leq$ 40 kHz), mixed sensors combined with non resistive or resistive flux transformers had the same detectivity gain. It is mainly explained by a low cutoff frequency in the resistive flux transformer and a noise dominated by the Giant MagnetoResistance

thermal noise in both cases. A 1 cm^2 mixed sensor with a detectivity around 120 $fT/\sqrt{Hz}$ combined with a resistive or non resistive flux transformer offered a final detectivity respectively around 28 $fT/\sqrt{Hz}$ and 11 $fT/\sqrt{Hz}$. As the main source of noise is coming from the giant magnetoresistance, the use of a tuned flux transformer has been discussed. With a quality factor around 20, we achieve a detectivity around 1.75 $fT/\sqrt{Hz}$. Then flux transformers have been incorporated in an MRI experiment with success and no additional noise due to new coupling effect has been measured. Magnetic Resonance Imaging experiments have been performed with this system with good results despite the limitation due to the cryogenic dewar and the filling factor.

Spin echo and gradient echo sequences have been introduced to perform three dimensional imaging. The third dimension was acquired using a double phase encoding gradient or a slice selection gradient, depending on the sample. Both methods offered similar images with 1 mm x 1 mm x 1 mm resolution. Distortion and shielding induced by metallic implants have been tested using small pieces of titanium and an aluminum can. As predicted, the titanium had a negligible effect on the image but the can was entirely shielding the signal and the RF pulse. Multi spin echo and inversion recovery sequences have been introduced to perform relaxometry study of different liquids and tissues. The T_1 measurements of agarose showed important changes for different concentrations reinforcing the idea that 10 mT is a relevant field range. A three dimensional mapping of T_1 and T_2 has been performed for an in-vivo finger with poor results due to a low signal to noise ratio. Only the mean relaxation time of the entire finger has been determined with precision.

Fast Low Angle SHot and Echo Planar Imaging have been introduced to increase the signal-to-noise ratio per acquisition time. Both methods have been performed on a regular cartesian grid to avoid any reconstruction complication in a first step. During a equivalent period of time, one and two dimensional imaging have been performed on phantoms to compare the resulting signal to noise ratio after the reconstruction. The efficient acquisition scheme of FLASH and EPI have led to an increase of the signal-to-noise ratio by a factor 1.4 and 1.5. However, the use of stronger gradients to trade some spatial resolution against temporal resolution is not yet relevant according to the lack of signal-to-noise ratio.

To conclude, I would say that very low field MRI is a very promising technique. The lack of signal-to-noise ratio is a substantial issue but there are still many improvements (sensors detectivity, multichannel acquisition, undersampling,...) that could lead to a very ef-

ficient system. The next important step should be to perform in-vivo measurements on the brain to determine diagnosis possibilities. The cost and the flexibility of very low field MRI are significant assets and this device could become an important complementary imaging method.

BIBLIOGRAPHY

[1] Flux. (Cited on page 46.)

[2] *Phobias: a handbook of theory, research, and treatment*. Wiley, Chichester ; New York, 1997. (Cited on page 5.)

[3] *Methods in biomedical magnetic resonance imaging and spectroscopy*. Encyclopedia of nuclear magnetic resonance. Wiley, Chichester ; New York, 2000. (Cited on page 35.)

[4] *The SQUID handbook*. Wiley-VCH, Weinheim, 2004. (Cited on page 69.)

[5] Weston A. Anderson. Electrical current shims for correcting magnetic fields. *Review of Scientific Instruments*, 32(3):241, 1961. (Cited on page 46.)

[6] Jan H. Ardenkjær-Larsen, Björn Fridlund, Andreas Gram, Georg Hansson, Lennart Hansson, Mathilde H. Lerche, Rolf Servin, Mikkel Thaning, and Klaes Golman. Increase in signal-to-noise ratio of> 10,000 times in liquid-state NMR. *Proceedings of the National Academy of Sciences*, 100(18):10158–10163, 2003. (Cited on page 18.)

[7] MN Baibich, JM Broto, A Fert, and FN Van Dau. Giant magnetoresistance of (001) Fe/(001) Cr magnetic superlattices. *Physical Review Letters*, 61(001):2472–2475, 1988. (Cited on page 75.)

[8] Nicolaas Bloembergen, Edward Mills Purcell, and Robert V. Pound. Relaxation effects in nuclear magnetic resonance absorption. *Physical Review*, 73(7):679, 1948. (Cited on page 29.)

[9] Dmitry Budker and Michael Romalis. Optical magnetometry. *Nature Physics*, 3(4):227–234, 2007. (Cited on page 72.)

[10] Sarah Busch, Michael Hatridge, Michael Mößle, Whittier Myers, Travis Wong, Michael Mück, Kevin Chew, Kyle Kuchinsky, Jeffry Simko, and John Clarke. Measurements of t(1) -relaxation in ex vivo prostate tissue at 132 μT. *Magnetic resonance in medicine: official journal of the Society of Magnetic Resonance in Medicine / Society of Magnetic Resonance in Medicine*, 67(4):1138–1145, April 2012. PMID: 22294500. (Cited on pages 6, 30, and 31.)

[11] Wallace H. Campbell. *Introduction to geomagnetic fields*. Cambridge University Press, Cambridge ; New York, 2nd. ed edition, 2003. (Cited on page 5.)

[12] R. Cantor, L. P. Lee, M. Teepe, V. Vinetskiy, and J. Longo. Low-noise, single-layer YBa< sub> 2</sub> cu< sub> 3</sub> o< sub> 7-x</sub> DC SQUID magnetometers at 77 k. *Applied Superconductivity, IEEE Transactions on*, 5(2):2927–2930, 1995. (Cited on page 69.)

[13] John Clarke, Michael Hatridge, and Michael Mößle. SQUID-Detected magnetic resonance imaging in microtesla fields. *Annual Review of Biomedical Engineering*, 9(1):389–413, August 2007. (Cited on pages 6, 67, 70, and 71.)

[14] R Coehoorn. Giant magnetoresistance and magnetic interactions in exchange-biased spin-valves. *Handbook of magnetic materials*, (September 1999), 2003. (Cited on page 77.)

[15] J. H. Coggon. ELECTROMAGNETIC AND ELECTRICAL MODELING BY THE FINITE ELEMENT METHOD. *GEOPHYSICS*, 36(1):132–155, February 1971. (Cited on page 37.)

[16] Charles H. Cunningham, John M. Pauly, and Krishna S. Nayak. Saturated double-angle method for rapidB1+ mapping. *Magnetic Resonance in Medicine*, 55(6):1326–1333, June 2006. (Cited on page 53.)

[17] R Damadian, M Goldsmith, and L Minkoff. NMR in cancer: XVI. FONAR image of the live human body. *Physiological chemistry and physics*, 9(1):97–100, 108, 1977. PMID: 909957. (Cited on page 9.)

[18] Hadrien Dyvorne. *Superconducting-Giant MagnetoResistive Mixed Sensors for Nuclear Magnetic Resonance*. PhD thesis. (Cited on pages 33, 36, and 58.)

[19] R. R. Ernst. Application of fourier transform spectroscopy to magnetic resonance. *Review of Scientific Instruments*, 37(1):93, 1966. (Cited on page 134.)

[20] Michelle Espy, Shermiyah Baguisa, David Dunkerley, Per Magnelind, Andrei Matlashov, Tuba Owens, Henrik Sandin, Igor Savukov, Larry Schultz, Algis Urbaitis, and Petr Volegov. Progress on detection of liquid explosives using ultra-low field MRI. *IEEE Transactions on Applied Superconductivity*, 21(3):530–533, June 2011. (Cited on pages 122, 127, and 128.)

[21] C. Fermon, M. Pannetier-Lecoeur, N. Biziere, and B. Cousin. Optimised GMR sensors for low and high frequencies applications. *Sensors and Actuators A: Physical*, 129(1-2):203–206, May 2006. (Cited on page 76.)

[22] S. Gabriel, R. W. Lau, and Camelia Gabriel. The dielectric properties of biological tissues: II. measurements in the frequency range

10 hz to 20 GHz. *Physics in medicine and biology*, 41(11):2251, 1996. (Cited on page 20.)

[23] A Guedes, JM Almeida, S Cardoso, R Ferreira, and PP Freitas. Improving magnetic field detection limits of spin valve sensors using magnetic flux guide concentrators. *Magnetics, IEEE Transactions on*, 43(6):2376–2378, 2007. (Cited on page 78.)

[24] A Haase, J Frahm, D Matthaei, W Hanicke, and K.-D Merboldt. FLASH imaging. rapid NMR imaging using low flip-angle pulses. *Journal of Magnetic Resonance (1969)*, 67(2):258–266, April 1986. (Cited on pages 133 and 134.)

[25] Gunther Helms, Henning Dathe, and Peter Dechent. Quantitative FLASH MRI at 3T using a rational approximation of the ernst equation. *Magnetic Resonance in Medicine*, 59(3):667–672, March 2008. (Cited on page 136.)

[26] F. N. Hooge. 1/f noise is no surface effect. *Physics Letters*, 29(3):139–140, 1969. (Cited on page 81.)

[27] Thomas L. James. Fundamentals of NMR. *Department of Pharmaceutical Chemistry University of California San Francisco, CA 94143-0446 USA*, 1998. (Cited on page 30.)

[28] J. Jaycox and M. Ketchen. Planar coupling scheme for ultra low noise dc SQUIDs. *Magnetics, IEEE Transactions on*, 17(1):400–403, 1981. (Cited on page 70.)

[29] Seungmun Jeon, Gunhee Jang, Hyunchul Choi, and Sukho Park. Magnetic navigation system with gradient and uniform saddle coils for the wireless manipulation of micro-robots in human blood vessels. *IEEE Transactions on Magnetics*, 46(6):1943–1946, June 2010. (Cited on page 52.)

[30] R P Klucznik, D A Carrier, R Pyka, and R W Haid. Placement of a ferromagnetic intracerebral aneurysm clip in a magnetic field with a fatal outcome. *Radiology*, 187(3):855–856, June 1993. PMID: 8497645. (Cited on page 118.)

[31] I. K. Kominis, T. W. Kornack, J. C. Allred, and M. V. Romalis. A subfemtotesla multichannel atomic magnetometer. *Nature*, 422(6932):596–599, April 2003. (Cited on page 72.)

[32] S.-K. Lee, K. L. Sauer, S. J. Seltzer, O. Alem, and M. V. Romalis. Subfemtotesla radio-frequency atomic magnetometer for detection of nuclear quadrupole resonance. *Applied Physics Letters*, 89(21):214106, 2006. (Cited on page 73.)

[33] Seung Kyun Lee, Michael M??le, Whittier Myers, Nathan Kelso, Andreas H. Trabesinger, Alexander Pines, and John Clarke.

SQUID-detected MRI at 132 ?T withT1-weighted contrast established at 10 ?T-300 mT. *Magnetic Resonance in Medicine*, 53(1):9–14, January 2005. (Cited on pages 30, 127, and 128.)

[34] Terri L Lindholm, Lisa Botes, Eva-Lena Engman, Anders Frank, Tomas Jonsson, Leif Svensson, and Per Julin. Parallel imaging: is GRAPPA a useful acquisition tool for MR imaging intended for volumetric brain analysis? *BMC Medical Imaging*, 9(1):15, 2009. (Cited on page 149.)

[35] M. Lustig, D.L. Donoho, J.M. Santos, and J.M. Pauly. Compressed sensing MRI. *IEEE Signal Processing Magazine*, 25(2):72–82, March 2008. (Cited on page 149.)

[36] Michael Lustig, David Donoho, and John M. Pauly. Sparse MRI: the application of compressed sensing for rapid MR imaging. *Magnetic Resonance in Medicine*, 58(6):1182–1195, December 2007. (Cited on page 149.)

[37] Vince I. Madai, Federico C. von Samson-Himmelstjerna, Miriam Bauer, Katharina L. Stengl, Matthias A. Mutke, Elena Tovar-Martinez, Jens Wuerfel, Matthias Endres, Thoralf Niendorf, and Jan Sobesky. Ultrahigh-field MRI in human ischemic stroke – a 7 tesla study. *PLoS ONE*, 7(5):e37631, May 2012. (Cited on page 17.)

[38] Peter Mansfield. Multi-planar image formation using NMR spin echoes. *Journal of Physics C: Solid State Physics*, 10(3):L55, 1977. (Cited on page 140.)

[39] Sunderarajan S. Mohan, Maria del Mar Hershenson, Stephen P. Boyd, and Thomas H. Lee. Simple accurate expressions for planar spiral inductances. *Solid-State Circuits, IEEE Journal of*, 34(10):1419–1424, 1999. (Cited on page 107.)

[40] Michael Mößle, Song-I Han, Whittier R. Myers, Seung-Kyun Lee, Nathan Kelso, Michael Hatridge, Alexander Pines, and John Clarke. SQUID-detected microtesla MRI in the presence of metal. *Journal of Magnetic Resonance*, 179(1):146–151, March 2006. (Cited on pages 118 and 120.)

[41] M. Moszligle, W.R. Myers, S.-K. Lee, N. Kelso, M. Hatridge, A. Pines, and J. Clarke. SQUID-Detected in vivo MRI at microtesla magnetic fields. *IEEE Transactions on Appiled Superconductivity*, 15(2):757–760, June 2005. (Cited on page 18.)

[42] John P. Mugler and Talissa A. Altes. Hyperpolarized ^{129} xe MRI of the human lung. *Journal of Magnetic Resonance Imaging*, 37(2):313–331, February 2013. (Cited on page 18.)

[43] Whittier Myers, Daniel Slichter, Michael Hatridge, Sarah Busch, Michael Mößle, Robert McDermott, Andreas Trabesinger, and John Clarke. Calculated signal-to-noise ratio of MRI detected with SQUIDs and faraday detectors in fields from 10μT to 1.5T. *Journal of Magnetic Resonance*, 186(2):182–192, June 2007. (Cited on page 20.)

[44] Albert Overhauser. Polarization of nuclei in metals. *Physical Review*, 92(2):411–415, October 1953. (Cited on page 18.)

[45] M. Pannetier. Femtotesla magnetic field measurement with magnetoresistive sensors. *Science*, 304(5677):1648–1650, June 2004. (Cited on page 6.)

[46] M Pannetier, C Fermon, and G Le Goff. Noise in small magnetic systems - Applications to very sensitive magnetoresistive sensors. *...and magnetic materials*, 00:8–10, 2005. (Cited on page 77.)

[47] Pasquale Paolantonio, Riccardo Ferrari, Fabrizio Vecchietti, Salvatore Cucchiara, and Andrea Laghi. Current status of MR imaging in the evaluation of IBD in a pediatric population of patients. *European Journal of Radiology*, 69(3):418–424, March 2009. (Cited on page 149.)

[48] George A. Rinard, Richard W. Quine, Gareth R. Eaton, Sandra S. Eaton, Eugene D. Barth, Charles A. Pelizzari, and Howard J. Halpern. Magnet and gradient coil system for low-field EPR imaging. *Concepts in Magnetic Resonance*, 15(1):51–58, 2002. (Cited on page 36.)

[49] Francoise Romeo and D. I. Hoult. Magnet field profiling: analysis and correcting coil design. *Magnetic Resonance in Medicine*, 1(1):44–65, 1984. (Cited on page 35.)

[50] I. Savukov and T. Karaulanov. Anatomical MRI with an atomic magnetometer. *Journal of Magnetic Resonance*, 231:39–45, June 2013. (Cited on pages 6 and 74.)

[51] I.M. Savukov, V.S. Zotev, P.L. Volegov, M.A. Espy, A.N. Matlashov, J.J. Gomez, and R.H. Kraus. MRI with an atomic magnetometer suitable for practical imaging applications. *Journal of Magnetic Resonance*, 199(2):188–191, August 2009. (Cited on page 74.)

[52] H. C. Seton, J. M. S. Hutchison, and D. M. Bussell. Gradiometer pick-up coil design for a low field SQUID-MRI system. *Magnetic Resonance Materials in Physics, Biology and Medicine*, 8(2):116–120, 1999. (Cited on page 70.)

[53] B. H. Suits and D. E. Wilken. Improving magnetic field gradient coils for NMR imaging. *Journal of Physics E: Scientific Instruments*, 22(8):565, 1989. (Cited on page 48.)

[54] E C Unger, M S Cohen, and T R Brown. Gradient-echo imaging of hemorrhage at 1.5 tesla. *Magnetic resonance imaging*, 7(2):163–172, April 1989. PMID: 2716484. (Cited on page 136.)

[55] P. Vedrine, G. Aubert, F. Beaudet, J. Belorgey, J. Beltramelli, C. Berriaud, P. Bredy, P. Chesny, A. Donati, G. Gilgrass, G. Grunblatt, F.P. Juster, F. Molinie, C. Meuris, F. Nunio, A. Payn, L. Quettier, J.M. Rey, T. Schild, and A. Sinanna. The whole body 11.7 t MRI magnet for Iseult/INUMAC project. *IEEE Transactions on Applied Superconductivity*, 18(2):868–873, June 2008. (Cited on page 6.)

[56] F. Verpillat, M. P. Ledbetter, S. Xu, D. J. Michalak, C. Hilty, L.-S. Bouchard, S. Antonijevic, D. Budker, and A. Pines. Remote detection of nuclear magnetic resonance with an anisotropic magnetoresistive sensor. *Proceedings of the National Academy of Sciences*, 105(7):2271–2273, 2008. (Cited on page 18.)

[57] M Zierhofer. Geometric Approach for Coupling Enhance of Magnetically Coupled Coils. 43(7):708–714, 1996. (Cited on page 106.)

[58] V.S. Zotev, A.N. Matlashov, I.M. Savukov, T. Owens, P.L. Volegov, J.J. Gomez, and M.A. Espy. SQUID-Based microtesla MRI for in vivo relaxometry of the human brain. *IEEE Transactions on Applied Superconductivity*, 19(3):823–826, June 2009. (Cited on page 30.)